The Ultrafast Laser Inscription of Photonic Devices for Integrated Optical Applications

Stephen J. Beecher

Submitted for the degree of Doctor of Philosophy

Department of Physics

School of Engineering and Physical Sciences

Heriot-Watt University

March – 2012

Abstract

A study of some key areas in which ultrafast laser inscription may usefully be employed is presented. The thesis includes waveguide inscription in a variety of substrates including passive glass, doped glass and a nonlinear crystal. The work contained can be split into three studies, with some overlap between them.

Firstly fused silica glass is used, both in planar substrates and as flat fibre, for the inscription of two sensing elements. The planar substrate is used for a device similar in design to a side-polished fibre and the flat fibre is used for the fabrication of a Bragg grating waveguide array.

In the second study, waveguides are inscribed in the nonlinear crystal monoclinic bismuth borate, and used for guided mode second harmonic generation. A novel waveguide design is employed to increase overlap between the pump and second harmonic waveguide modes.

The remainder of the thesis investigates the applicability of ultrafast laser inscription to the fabrication of compact modelocked lasers. Lasing is demonstrated, both continuous wave and modelocked, using a laser inscribed erbium doped bismuthate glass waveguide as the gain element. A study is then undertaken into methods of integrating carbon nanotubes, used as saturable absorbers to modelock lasers, into laser inscribed waveguides.

Acknowledgements

There are many people whose help and guidance made the work in this thesis possible.

First I would like to thank my supervisor, Ajoy Kar, for his continuous support and advice over the duration of my PhD. The trips and exchanges he has organised have provided an education far beyond the field of photonics, I'll never forget the elephant safari in Guwahati.

I would also like to thank the other members of the Nonlinear Optics Group for their help, most specifically Robert Thomson and Nick Psaila for training me in the art of ULI and the science of waveguide characterisation. Graeme Brown's help on Bragg grating inscription and CAD of silica parts was vital for the flat fibre work I have completed.

Adi Choudhury deserves my gratitude for his help and advice which made our trip to India a fantastic experience.

I am grateful to Derryck Reid for useful discussions on the modelling of nonlinear optical systems, his help with coding these problems and the loan of a variety of equipment.

I would like to thank Keith Serrels for the use of his modelocked erbium doped fibre laser for the characterisation of SWNT samples and his advice in modelocking my erbium doped waveguide laser.

My thanks go to all of the technical staff who rushed through work at the last minute. Of particular note are Peter Heron and Mark Stewart from the Physics Mechanical Workshop and Neil Ross for cutting our substrates.

I also appreciate the contributions from my collaborators at The University of Cambridge: Andrea Ferrari, Zhipei Sun and Daniel Poppa for supplying the SWNTs and for our useful discussions on the best direction to go for SWNT-ULI integration.

I am grateful to the researchers I met at the Politecnico di Milano during my month there. Roberto Osellame's and Giulio Cerullo's work made for a productive and enjoyable trip. I appreciate Rebeca Martinez's work, giving me a grounding in biology

and more specifically capillary electrophoresis. I would like to thank Jenny Clark for recommending some superb pubs, restaurants and sights to see. I'd also like to thank Simone for tirelessly translating the cycling related pages of the Gazzetta Dello Sport in the run up to the Road Cycling World Championships in Varese. Cheers to Yu Gu, Shane Eaton, Andrea Crespi, as well as the others for great company during lunchtime and espresso breaks.

I am indebted to my office mates for their continued tolerance and contagious eccentricities.

My family, Ann, Phil and Hazel deserve special recognition for the role they have played in my life.

Finally I would like to give my heart-felt thanks to my fiancée Teresa Ferreiro, whose support and patience have made the writing of this thesis possible.

ACADEMIC REGISTRY
Research Thesis Submission

Name*:*	Stephen J. Beecher		
School/PGI:	EPS		
Version: *(i.e. First, Resubmission, Final)*	First	Degree Sought (Award **and** Subject area)	PhD, Physics

Declaration

In accordance with the appropriate regulations I hereby submit my thesis and I declare that:

1) the thesis embodies the results of my own work and has been composed by myself
2) where appropriate, I have made acknowledgement of the work of others and have made reference to work carried out in collaboration with other persons
3) the thesis is the correct version of the thesis for submission and is the same version as any electronic versions submitted*.
4) my thesis for the award referred to, deposited in the Heriot-Watt University Library, should be made available for loan or photocopying and be available via the Institutional Repository, subject to such conditions as the Librarian may require
5) I understand that as a student of the University I am required to abide by the Regulations of the University and to conform to its discipline.

* *Please note that it is the responsibility of the candidate to ensure that the correct version of the thesis is submitted.*

Signature of Candidate*:*		Date:	

Submission

Submitted By *(name in capitals):*	STEPHEN J. BEECHER
Signature of Individual Submitting:	
Date Submitted:	

For Completion in the Student Service Centre (SSC)

Received in the SSC by *(name in capitals):*			
Method of Submission (Handed in to SSC; posted through internal/external mail):			
E-thesis Submitted (mandatory for final theses)			
Signature:		Date:	

Publications by the author

Peer reviewed journal articles by the author

1. R. R. Thomson, A. S. Bockelt, E. Ramsay, S. Beecher, A. H. Greenaway, A. K. Kar and D. T. Reid, "Shaping ultrafast laser inscribed optical waveguides using a deformable mirror," Opt. Express **16**, 12786-12793 (2008).

2. S. J. Beecher, R. R. Thomson, N. D. Psaila, Z. Sun, T. Hasan, A. G. Rozhin, A. C. Ferrari and A. K. Kar, "320 fs pulse generation from an ultrafast laser inscribed waveguide laser mode-locked by a nanotube saturable absorber," Appl. Phys. Lett. **97**, 111114 (2010).

3. J. R. Macdonald, R. R. Thomson, S. J. Beecher, N. D. Psaila, H. T. Bookey and A. K. Kar, "Ultrafast laser inscription of near-infrared waveguides in polycrystalline ZnSe," Opt. Lett. **35**, 4036-4038 (2010).

4. R. R. Thomson, N. D. Psaila, S. J. Beecher and A. K. Kar, "Ultrafast laser inscription of a high-gain Er-doped bismuthate glass waveguide amplifier," Opt. Express **18**, 13212-13219 (2010).

5. S. Beecher, R. Thomson, B. Pal and A. Kar, "Single Stage Ultrafast Laser Inscription of a Side-Polished Fiber-like Waveguide Sensor," Sensors Journal, IEEE **PP**, 1-1 (2011).

6. S. J. Beecher, R. R. Thomson, D. T. Reid, N. D. Psaila, M. Ebrahim-Zadeh and A. K. Kar, "Strain field manipulation in ultrafast laser inscribed BiB_3O_6 optical waveguides for nonlinear applications," Opt. Lett. **36**, 4548-4550 (2011).

7. R. Mary, S. Beecher, G. Brown, R. Thomson, D. Jaque, S. Ohara and A. Kar, "A Compact, Highly Efficient Ytterbium Doped Bismuthate Glass Waveguide Laser," Opt. Lett. **Early Postings** (2012).

Conference papers by the author

1. S. J. Beecher, R. R. Thomson, N. D. Psaila, A. K. Kar, Z. Sun, T. Hasan, A. Rozhin and A. C. Ferrari, "420 fs Pulses from an Ultrafast Laser Inscribed Waveguide Laser Utilizing a Carbon Nanotube Saturable Absorber," in CLEO, OSA Technical Digest (CD) (Optical Society of America, 2010), CThI6.

2. S. J. Beecher, R. R. Thomson, N. D. Psaila, D. T. Reid, A. K. Kar and M. Ebrahim-Zadeh, "Strain Field Manipulation in Ultrafast Laser Inscribed Nonlinear BiB_3O_6 Optical Waveguides," in CLEO, OSA Technical Digest (CD) (Optical Society of America, 2010), JThE84.

3. R. R. Thomson, S. Beecher, N. D. Psaila and A. K. Kar, "Ultrafast Laser Inscription of a High Gain Er-Doped Bismuthate Glass Waveguide Amplifier," in Advanced Solid-State Photonics (ASSP), OSA Technical Digest Series (CD) (Optical Society of America, 2010), AWB7.

4. S. J. Beecher, R. R. Thomson and A. K. Kar, "The Evanescent Interaction of an Ultrafast Laser Inscribed Optical Waveguide," in CLEO, OSA Technical Digest (CD) (Optical Society of America, 2011), JTuH6.

5. R. Mary, S. Beecher, G. Brown, R. R. Thomson and A. K. Kar, "Yb-doped Bismuthate Glass waveguide laser fabricated by Ultrafast Laser Inscription," in Advanced Solid-State Photonics (ASSP), OSA Technical Digest (CD) (Optical Society of America, 2012), AM4A.14.

6. D. Choudhury, W. T. Ramsay, G. Brown, N. D. Psaila, S. Beecher, R. R. Thomson, R. Kiss, S. Pells, N. A. Willoughby, L. Paterson, and A. K. Kar, "A femtosecond laser inscribed biochip for stem cell therapeutic applications," 2010 23rd Annual Meeting of the IEEE Photonics Society (IEEE, New York, 2010). pp. 216-217.

7. J. R. Macdonald, R. R. Thomson, N. D. Psaila, S. J. Beecher, H. T. Bookey, and A. K. Kar, “Ultrafast Laser Inscription of Low Loss Waveguides in Polycrystalline ZnSe”, 2010 23rd Annual Meeting of the Ieee Photonics Society (IEEE, New York, 2010), pp. 56-57.

8. Y. Ren, S. Beecher, G. Brown, A. Rodenas, F. Chen, and A. Kar, “Near-IR to Mid-IR Multimode Waveguides in Rare-Earth doped YAG by Ultrafast Laser Inscription,” in CLEO 2012, accepted for oral presentation.

Contents

Table of figures

List of abbreviations

ANDi	All normal dispersion
AOM	Acousto-optic modulator
ASE	Amplified spontaneous emission
AWG	Arrayed waveguide grating
BiBO	Monoclinic bismuth borate
CL	Coupling loss
CPA	Chirped pulse amplification
CW	Continuous wave
DBR	Distributed Bragg reflector
DFB	Distributed feedback
DUT	Device under test
EDFA	Erbium doped fibre amplifier
EDWA	Erbium doped waveguide amplifier
EM	Electro-magnetic
FBG	Fibre Bragg grating
FWHM	Full width at half maximum
GNSE	Generalised nonlinear Schrödinger equation
HAZ	Heat affected zone
HF	Hydrofluoric acid
H-pol	Horizontally polarised
IL	Insertion loss
MCVD	Modified chemical vapour deposition
MFD	Mode field diameter
MPA	Multi photon absorption
NA	Numerical aperture
NIR	Near-infrared
NPE	Nonlinear polarisation evolution
O-DCB	Ortho-dichlorobenzene
OLP	Orthogonal linear polarisations
OSA	Optical spectrum analyser
PCF	Photonic crystal fibre
PDL	Polarisation dependent loss
PPKTP	Periodically poled potassium titanyl phosphate
PPLN	Periodically poled lithium niobate
PPLT	Periodically poled lithium tantalate
PSO	Position sensitive output
PVA	Polyvinylalcohol
SESAM	Semiconducting saturable absorbing mirror
SHG	Second harmonic generation
SUSSP66	Scottish universities summer school in physics 66
SWNT	Single walled carbon nanotubes
TPA	Two photon absorption
ULI	Ultrafast laser inscription
V-pol	Vertically polarised
WDM	Wavelength division multiplexer

Chapter 1. Introduction

1.1. Background

The aim of this project has been to attempt the construction of a compact, ultrafast laser inscribed, modelocked laser. To aid in this final goal there have also been investigations into the affects of writing waveguides in birefringent crystals and the use of ultrafast laser inscribed devices for sensing applications. This chapter will describe the development of dielectric optical waveguides for a range of applications, detail the development of ultrafast laser inscription (ULI) and provide an outline for the work presented in this thesis.

1.2. Dielectric optical waveguides

A dielectric is a non-conducting material that can be polarised by an incident electric field. A waveguide is a spatially inhomogeneous material that can confine light within a defined region such that the electric field distribution of the light does not vary as the light propagates along the structure. The guidance of visible and near-infrared (NIR) light by dielectric waveguides has been most heavily utilised for the long distance transmission of data through glass optical fibres. Optical fibre has in fact been so pervasive in its integration into modern society that ‘fibre optic’ is synonymous with high speed for any computational data transmission. There has been a rapid change from the predecessor, copper wire, considering that as recently as the 1960s it was unclear if the low loss guidance of light through dielectrics was even possible. As data rates increased copper wire became increasingly less efficient and it was clear that another system was required for long haul communication. Losses from optical fibres at this time were comparable, or in excess of, systems such as free space lens transmission lines or metallic waveguides [1, 2]. However, the work of Kao, among others, showed that a large portion of this loss was due to the low purity of the materials used and not fundamental to the nature of guided modes in dielectric media [3]. By the 1970s Corning® were commercially producing low loss optical fibre which, with the advent of the continuous wave (CW) helium neon (HeNe) laser, paved the way for light to take over from microwave and coaxial electrical signals for long distance, high data rate communication. Soon HeNe lasers were replaced by semiconductor lasers, which themselves relied on the guiding of light within the p-n junction [4, 5]. With the

development of additional components, this allowed for the creation of the systems currently in place throughout the world today.

The engineering of high quality optical fibres and optical waveguides has had significant impact on fields not immediately related to the encoded transport of information with the minimum possible loss of energy: fibre Bragg gratings (FBGs) have replaced electrical strain gauges for in situ strain measurements [6], and fibre gyroscopes are fitted in most commercial aeroplanes for navigation purposes [7]. The first fibre laser trailed the first laser by one year [8], and the ongoing development of fibre lasers has allowed for power scalability while maintaining high beam quality. Multiple kW outputs with near diffraction limited performance are now attainable and fibre lasers are seen as an attractive route to even greater average powers [9, 10]. The field of nonlinear fibre optics is also of significant interest due to the ability to confine light to a small spot size over a long propagation distance. This allows for high irradiances to be preserved over metres instead of the microns that would be permitted in non-guided configurations [11]. However, fibre drawing is limited to certain select materials, imposes limits on the geometries of the devices, and the interaction of the light with the external environment requires severe modification of the fibre. For these reasons alternative waveguide fabrication technologies, although unable to compete with fibre for long haul data transmission due their higher propagation losses, are still of interest for many applications. For example arrayed waveguide gratings (AWGs) are extensively used for wavelength division multiplexing and de-multiplexing in long haul optical fibre networks, Mach-Zehnder interferometers are used as switches for time division multiplexing, and optical backplanes are starting to see use for server-to-server communication.

1.3. Ultrafast Laser Inscription

Many optical waveguide fabrication techniques exist, some made commercially viable by a single application or a few applications they perform exceedingly well, but most are limited to a single material. In 1996 Davis *et al.* showed that the nonlinear absorption of femtosecond pulses in a material could result in a permanent increase in the refractive index of that material [12]. Over the next 10 years the range of materials processable into waveguides through laser irradiation increased massively, in part due to the fact that the facilities required for the laser inscription could already be found in many ultrafast optics groups throughout the world. Over this period the majority of

work utilised regeneratively amplified titanium doped sapphire (Ti:sapphire) lasers. Most of the systems operated at a wavelength close to 800 nm, had pulse durations of about 100 fs and repetition rates around 1 kHz. With these systems typical fabrication speeds were slow, measured in μm's per second for low loss waveguides. At about this time new systems became available: Professor Giulio Cerullo's group at the Politecnico di Millano acquired a modelocked cavity dumped Yb:glass oscillator from High Q®, producing slightly longer pulses but at far higher repetition rates from 100's of kHz up to multiple MHz [13]. In 2004 Professor Peter Herman's group (Laser Photonics Fabrication) in Toronto forged links with IMRA®, one of the largest manufactures of ultrafast fibre lasers, and started fabricating waveguides with similar pulse repetition frequencies to those attainable from modelocked cavity dumped systems [14].

Changes in the systems showed that high quality waveguides could be fabricated with longer pulses, closer to 500 fs than the 100 fs pulses used for previous work, there was also a massive decrease in fabrication times due to the 100 fold increase in laser repetition rates. Perhaps more crucially from a material point of view, the inter-pulse time was now comparable with the time required for heat to diffuse out of the focal volume in many materials, allowing cumulative heating to occur and with it a completely new waveguide morphology and index change mechanism. To further increase the repetition rates of laser sources some groups moved towards extended cavity oscillators, conventional ultrafast lasers designs but with far longer cavities and therefore lower repetition rates, typically in the low 10s of MHz, and higher pulse energies [15].

I joined Professor Ajoy Kar's Nonlinear Optics Group in February 2008. The group had branched out from pure nonlinear optics and was increasingly focussing upon ultrafast waveguide inscription - I was the second student to start a PhD. in this group specifically on the subject. Previous work had relied on the occasional use of a regeneratively amplified Ti:sapphire laser and translation stages which were routinely used by one of Professor Derryck Reid's students, and on a collaboration with Professor Giulio Cerrulo's group allowing Nicholas Psaila and Robert Thomson to gain expertise from his group and fabricate waveguides using their fabrication equipment. At about the time I joined the group we invested in a Fianium® master oscillator power amplifier ultrafast fibre laser system and a set of three axis Aerotech® computer controlled stages. On paper this system was comparable with that used in Toronto or the system that R. Thomson and N. Psaila had learned to use in Milan. I was also fortunate enough to

spend 4 weeks visiting Professor Giulio Cerullo's group in Milan to be trained in some facets of their work within the first year of my PhD. studies.

During my PhD. the group has gone from three people working on ULI at Heriot-Watt to it now being the main focus of Professor Kar's group, with almost every person in the group using a device fabricated by this method for some area of their work.

1.4. Thesis Outline

The work presented in this thesis comprises three independent studies. The first is into sensing elements and sensor networks benefitting from ULI's flexibility and ability to rapidly prototype. The second study is conducted within the crystal monoclinic bismuth borate and demonstrates a novel approach to the control of the polarisation dependent guiding characteristics often encountered when employing ULI of waveguides within crystals. The third part of this thesis lays the foundations for the successful demonstration of a compact, environmentally stable, high repetition rate ultrafast oscillator. This part describes a gain element fabricated in an erbium doped bismuthate glass featuring a broad gain bandwidth and high gain per unit length, shows the characterisation of a CW and then passively modelocked laser based on this gain element and includes work on the integration of cavity components into structurally stable ULI elements.

Chapter 2 gives an introduction to nonlinear optics, including nonlinear absorption, material modification and the processes at work during waveguide inscription with an ultrafast laser. Some of the variables which must be considered in this process are discussed and a review of some devices fabricated by this technology is presented.

Chapter 3 presents the fabrication and characterisation of two distinct classes of sensor whose design is based upon successful fibre sensors. The first part details a sensor which borrows from side-polished fibres allowing the sensing of changes to an external medium. The second part reports the fabrication and characterisation of a 3x3 coupler and three different period Bragg grating waveguides to allow strain to be measured as well as load direction in a device fabricated into a piece of 'flat fibre'.

Chapter 4 details an investigation into the polarisation dependent guiding nature of waveguides fabricated in crystals which rely on the strain-optic effect for confinement of the waveguide mode. The work is carried out in the nonlinear crystal monoclinic

bismuth borate and type I birefringently phase matched second harmonic generation is demonstrated.

Chapter 5 reports work on a CW laser whose gain element is fabricated by ULI in an erbium doped bismuthate glass. A Rigrod type analysis is carried out to extract information about the properties of the waveguide useful for the following construction of a modelocked laser.

Chapter 6 presents work on a passively modelocked laser featuring the gain element studied in the previous chapter. Soliton modelocking is initiated and stabilised by a single walled carbon nanotube composite saturable absorber. The laser produces near bandwidth limited 320 fs pulses.

Chapter 7 outlines the development towards the integration of the carbon nanotube composite saturable absorber into ULI fabricated devices readily integrated into a compact laser cavity.

Chapter 8 introduces a numerical model which is used to investigate short pulse amplification within a ULI waveguide. Results are presented and an interesting amplification regime is identified.

Chapter 9 presents conclusions reached during the work performed and ideas for further work.

Chapter 2. Ultrafast Laser Inscription

2.1. Nonlinear optics in ultrafast laser inscription

The fabrication of optical waveguides by ULI relies extensively on nonlinear energy deposition, close to the laser focus, within a chosen substrate. Amplified femtosecond lasers provide an ideal source for the high peak powers necessary to drive these nonlinear processes. The first part of this chapter details the way in which femtosecond pulses interact with material before reviewing the permanent structural changes that can occur in a material. The final part of the chapter will look at the different variables that can be controlled for the fabrication of waveguides by ULI and the effects that they can have on the structures created.

2.2. Nonresonant optical nonlinearities

When an oscillating electro-magnetic (EM) field propagates through a dielectric material it exerts a polarising force on the electrons. The inner electrons of the atoms will be tightly bound to the nucleus and so the polarising effect will be mainly experienced by the outer, or valence, electrons. With low intensity light sources, the electric field of the light is much weaker than that binding the electrons to the atoms. The light causes a small perturbation to the atomic electric field and results in a material polarisation which is proportional to the electric field of the light [16].

$$\vec{P}_{linear}(t) = \varepsilon_0 \chi_{linear} \vec{E}(t) \qquad (1)$$

where P_{linear} is the polarisation, E is the electric field, χ_{linear} is the constant linear susceptibility of the medium and ε_0 is the permittivity of free space [17].

However as with most physical systems which display a proportionality, it only occurs over a limited range, a simple example of this is Hook's law for a spring where the restoring force is directly proportional to the displacement for small displacements. This law is broken when the 'yield point' is reached. In optics, if the electric field of the light is comparable to that of the atomic fields of the material, the relationship between the material polarisation and the electric field of the light is no longer linear [16].

$$\vec{P}_{nonlinear}(t) = \varepsilon_0 \chi_{nonlinear} \vec{E}(t) \quad (2)$$

where $\chi_{nonlinear}$ is no longer a constant but can now become a function of the electric field.

Since for small electric fields the susceptibility is linear, it makes sense to express the polarisability as a Taylor series [17]:

$$\vec{P}_{nonlinear}(t) = \varepsilon_0 \chi_{linear} \vec{E}(t) + \varepsilon_0 \chi^{(2)} \vec{E}^2(t) + \varepsilon_0 \chi^{(3)} \vec{E}^3(t) + ... + \varepsilon_0 \chi^{(n)} \vec{E}^n(t) \quad (3)$$

where the quantities $\chi^{(n)}$ are the nth order nonlinear susceptibilities. In general, due to the vectorial nature of the fields, the nonlinear susceptibilities must be tensors, but for simplicity in this case we will assume P and E to be scalar quantities to allow us to get to grips with how this nonlinearity can physically manifest. Interestingly, a time varying polarisation can act as a source of new EM radiation, and since it is no longer a linear function of the incident electric field, the radiation it creates is not limited to the same frequency.

2.2.1. **Second harmonic generation**

The history of experimental nonlinear optics can be traced back to the q-switched ruby laser, capable of producing 3 J pulses in 10s of ns. When focussed the irradiances producible were astounding in comparison to anything previously attainable [18]. Optical second harmonic generation can be understood by considering the first two terms of the Taylor expansion

$$P_{nonlinear}(t) = \varepsilon_0 \chi_{linear} E(t) + \varepsilon_0 \chi^{(2)} E^2(t) \quad (4)$$

If EM radiation, $E(t) = Ee^{-i\omega t}$ is incident upon a material with a non-zero second order nonlinear susceptibility, where ω is the angular frequency of the wave and t is time, then we can consider the second term of the nonlinear susceptibility,

$$\frac{P^{(2)}(t)}{\varepsilon_0} = \chi^{(2)} E^2(t) = 2\chi^{(2)} EE^* + \chi^{(2)} E^2 e^{-2i\omega t} + \text{complex conjugates} \quad (5)$$

the second term of which can be seen as an oscillating electric field at twice the frequency of the input field, showing that a new frequency (a second harmonic) can be generated by the light interacting with the material. This is called second harmonic generation (SHG).

If the polarisability of the material is symmetric then the time averaged response for all even order processes, such as SHG, must be zero and therefore no energy transfer can occur via these processes. If the potential energy function of the material is not symmetric then energy transfer can occur, but it is unclear in which direction energy should flow. From Maxwell's equations for a lossless nonlinear medium displaying a $\chi^{(2)}$ nonlinearity a theoretical treatment of SHG can be arrived at, as reported by Armstrong *et al*. in 1962 [19]. From this we arrive at the coupled amplitude equations for the three fields, two fundamental fields and one second harmonic field, where the top equation represents one fundamental field, the second equation represents the second fundamental field and the bottom equation the second harmonic field.

$$\frac{dA_1}{dz} = \frac{8\pi i \omega_1^{\,2} d}{k_1 c^2} A_3 A_2^{\,*} e^{-i\Delta kz} \tag{6}$$

$$\frac{dA_2}{dz} = \frac{8\pi i \omega_1^{\,2} d}{k_1 c^2} A_3 A_1^{\,*} e^{-i\Delta kz} \tag{7}$$

$$\frac{dA_3}{dz} = \frac{8\pi i \omega_2^{\,2} d}{k_2 c^2} A_1 A_2 \; e^{i\Delta kz} \tag{8}$$

where A is the amplitude of the wave, k is the wavevector, d is the effective nonlinearity and $\Delta k = k_1 + k_2 - k_3$. For SHG $\omega_2 = 2\,\omega_1$.

Here we can see a Δk variable in the equation, the wavevector mismatch [20]. In the absence of chromatic dispersion, this wavevector mismatch would be zero for SHG. But in real materials this is not the case.

2.2.2. **Phase matching**

In order to achieve efficient nonlinear interactions in a real medium in the presence of chromatic dispersion, steps must be taken to in order to ensure that a proper phase

relationship between the interacting waves is maintained along the propagation direction (zero phase mismatch). If phase matching is achieved, amplitude contributions from different locations along the propagation axis in the nonlinear crystal can coherently combine in phase with one another.

If we start with zero intensity in the second harmonic and a fixed power in the fundamental split equally between the two fundamental fields, then this allows us to impose the boundary conditions necessary to solve this problem. That is if $A_1 = 1$ in equation (6), $A_2 = 1$ in equation (7) and $A_3 = 0$ in equation (8), then we can investigate the effect of wavevector mismatch.

A Matlab® model was created, based on these equations and boundary conditions, to show the effect of the wavevector mismatch, see Figure 2.1.

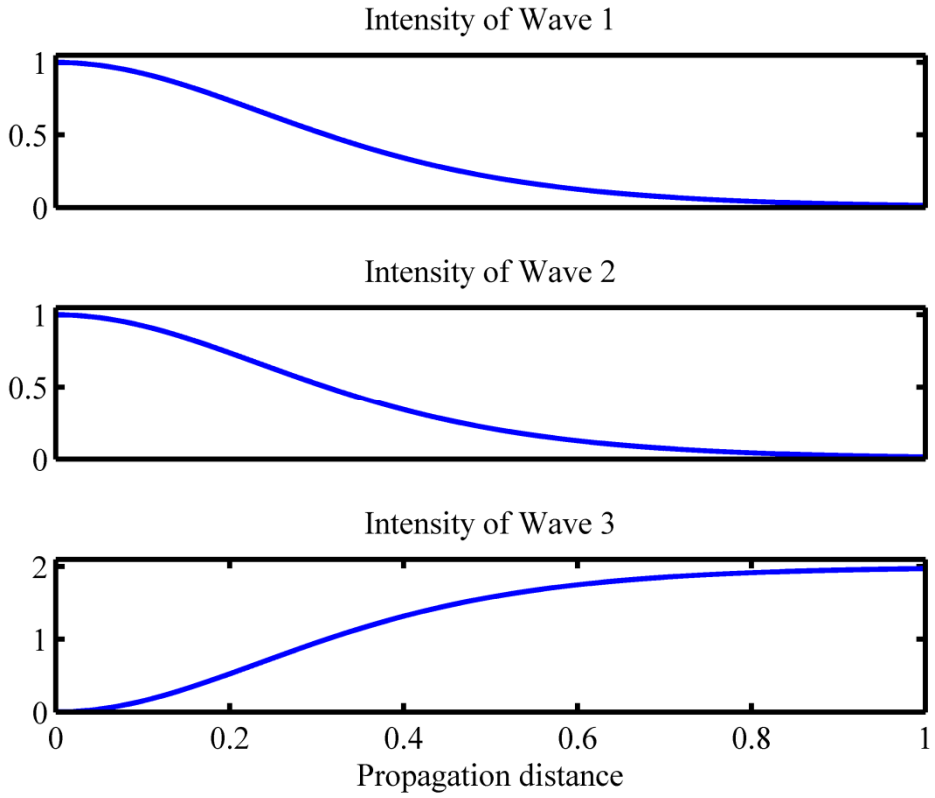

Figure 2.1. A wavevector mismatch of 0. Intensity of waves for different propagation distances along the crystal. Wave 1 and Wave 2 are the fundamental, Wave 3 is the second harmonic. Full depletion of the pump occurs.

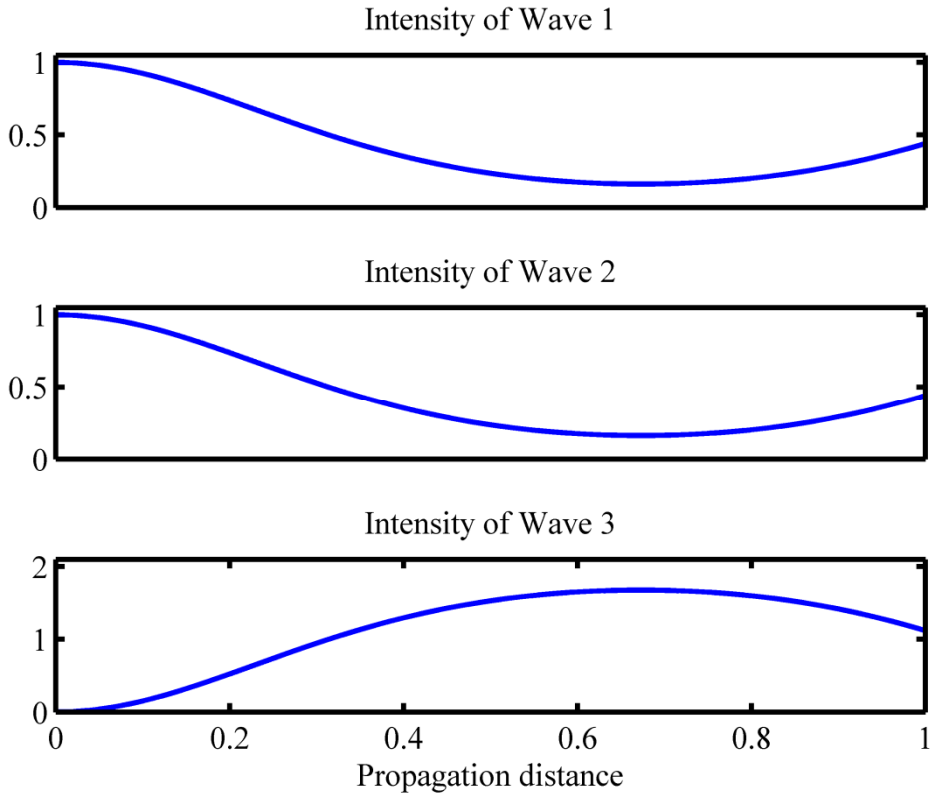

Figure 2.2. A wavevector mismatch of 1. Intensity of waves for different propagation distances along the crystal. After some propagation, back-conversion of the second harmonic wave starts to occur.

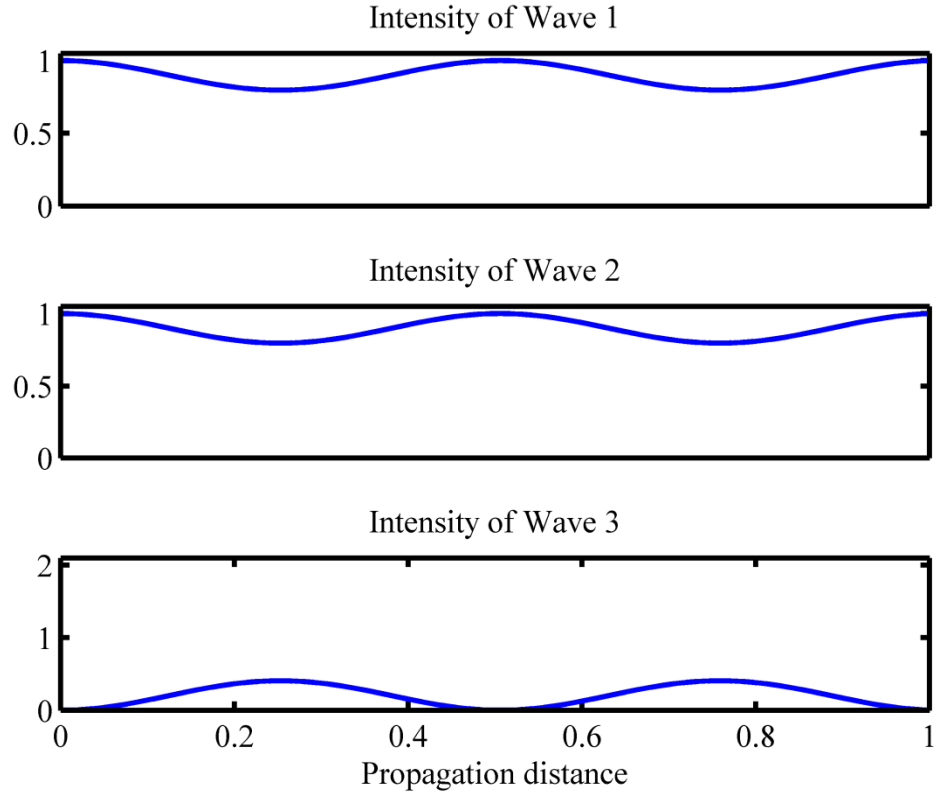

Figure 2.3. A wavevector mismatch of 10. Intensity of waves for different propagation distances along the crystal. Back-conversion occurs after a shorter distance.

As can be seen from Figure 2.1-Figure 2.3, if there is a wavevector mismatch then back-conversion of the second harmonic field can start to occur. As this wavevector mismatch increases, the amount of second harmonic generated at any point in this crystal is reduced significantly. This was the case with the first experimental SHG observation, conducted in crystal quartz, where no effort was made to phase match. It is also worth noting that the larger the bandwidth of the input field, the shorter the crystal must be in order that no back-conversion occurs for any wavelength component [19]. Two common methods exist for compensating for the chromatic dispersion: birefringent phase matching and quasi-phase matching. For birefringent phase matching a birefringent crystal is used and the polarisations of the fundamental and second harmonic waves are selected so as to result in a wavevector mismatch of zero for the desired process. A few geometries exist but two of the most common are type I and type II. Type I relies on both fundamental waves having one linear polarisation, and the second harmonic having an orthogonal linear polarisation and type II replies on the two fundamental waves having orthogonal linear polarisations and the second harmonic wave sharing polarisation with one of the fundamental waves [20]. Through this selection of the polarisations, phase matching can be accomplished even in media which display chromatic dispersion. If the crystal is not birefringent, or not birefringent along the axis you require for the nonlinear process, then birefringent phase matching is not possible. In this case quasi-phase matching may be utilised. Here no attempt is made to phase match the process but instead the direction of the domain of the crystal is inverted where a maximum for the second harmonic is reached, by repeating this domain inversion many times efficient SHG can occur. One method of achieving this is periodically polling and this has been demonstrated to great effect in periodically poled lithium niobate (PPLN) as well as several other materials (PPLT, PPKTP etc).

For type I birefringent phase matching, fine tuning of the phase matching condition can be achieved by rotation of the crystal, referred to as angle tuning. This rotation of the crystal affects the refractive index for one or both of the polarisations, dependent on the crystalline structure. Another method of tuning relies on the difference in the thermo-optic coefficients for the different crystal axes, allowing tuning by changing the temperature of the crystal, this is called temperature tuning.

2.3. Resonant optical nonlinearities

2.3.1. **Linear absorption**

When a material is exposed to light, the nature of the interaction is dependent upon a range of properties of the incident EM waves. If the highest band occupied by the electrons in a material (the valance band) is separated from the lowest unoccupied energy level (the conduction band) by a bandgap smaller than the energy of a photon, then a single photon incident on the material can promote an electron from the valance band to the conduction band. Over time this electron can thermalise with the lattice of the solid through collisions, transferring energy to the lattice. This is linear absorption and the relationship between the intensity of the light and the distance into the material is shown with the Beer-Lambert Law:

$$I(z) = I_0 e^{-\alpha z} \tag{9}$$

where I is intensity, α is the linear attenuation coefficient and z is the distance into the material [21].

2.3.2. **Nonlinear absorption**

With short pulses, the strong optical EM fields can be comparable with the atomic Coulomb potentials binding the outer electrons – so the interaction is inherently nonlinear. If the photon energy is not sufficient to promote an electron from the valance band to the conduction band, linear absorption is no longer possible. However nonlinear absorption mechanisms allow for absorption to still occur.

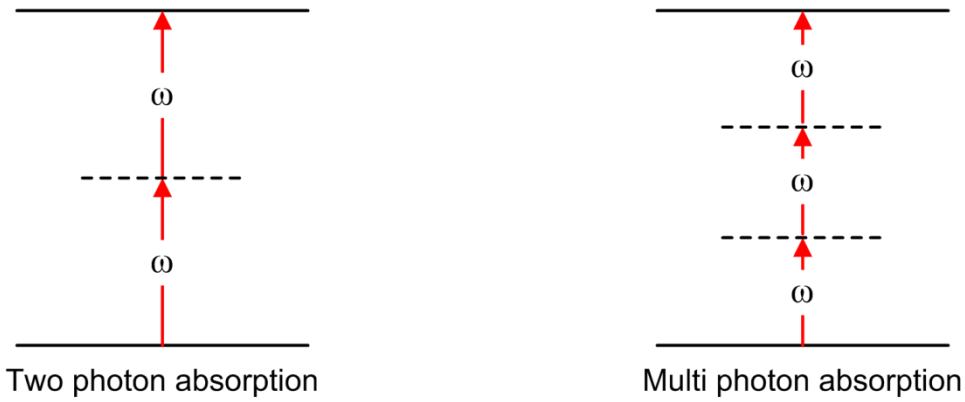

Figure 2.4. Left: energy level diagram describing two photon absorption. Right: energy level diagram describing multi photon absorption.

Two photon absorption (TPA) is an interaction between high intensity light and a material where an atom can simultaneously absorb two laser photons, promoting it from its ground state to an excited state. The absorption cross section, σ, for this process is directly proportional to the laser intensity:

$$\sigma = \sigma^{(2)} I \tag{10}$$

where $\sigma^{(2)}$ is the TPA coefficient [17]. This contrasts with linear absorption where the absorption cross section is independent of intensity. The absorption rate for TPA also scales with the square of the laser intensity [22]. This phenomena has been of most use for two photon fluorescence microscopy where, for example, a pair of ~900 nm photons from a modelocked Ti:sapphire laser can be used to excite a rhodamine 6G molecule, which will then emit in the visible part of the spectrum (~550 nm). Figure 2.5 shows one of the advantages of this technique for imaging, the inherent three dimensionality, so excitation is limited to the region of highest intensity, near the focus.

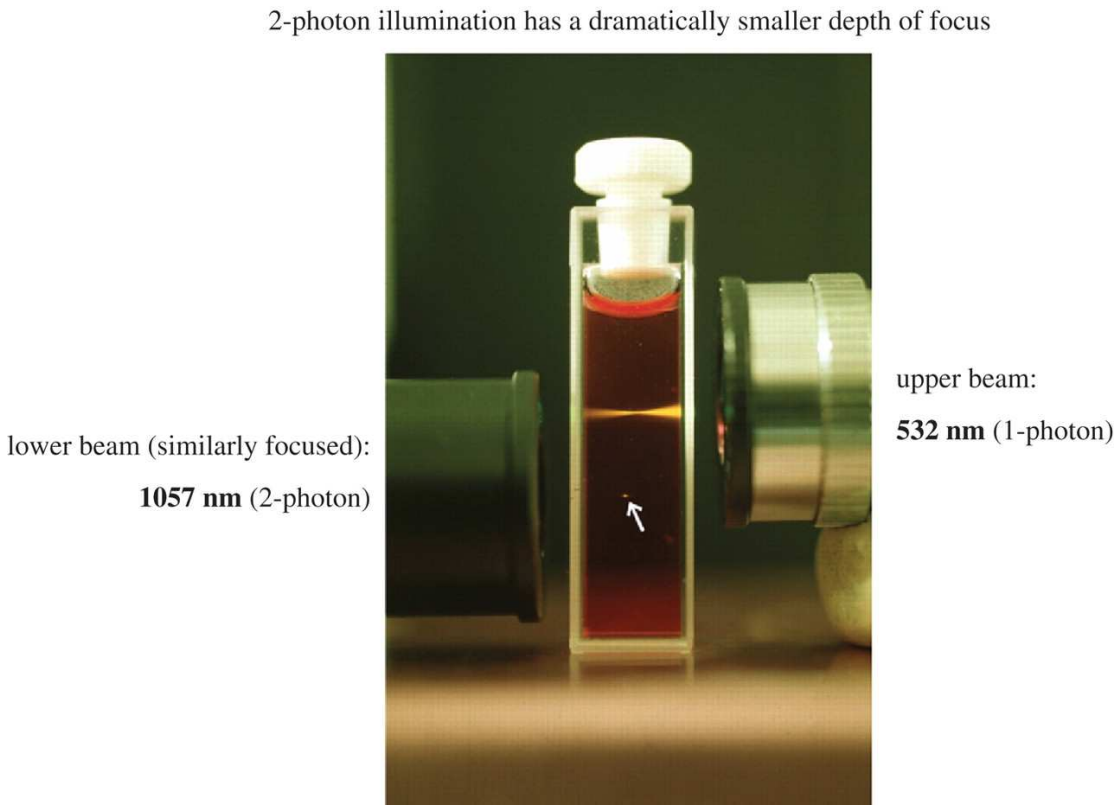

Figure 2.5. Two photon excitation microscopy, note that the absorption of the sub-bandgap light is limited to a small volume where the intensity is highest. Image taken from [23].

Similar processes can occur with the simultaneous absorption of more than two photons until the bandgap is reached, multi photon absorption (MPA), see Figure 2.4. However the probability of absorption will scale with the photon flux raised to the power of the number of photons required to exceed the bandgap energy, $\propto I^n$, where n is the minimum number of photons required to exceed the bandgap energy.

Another class of absorption mechanism exists, which is based solely on the electric field strength of incident light and not on photon energy. If the strength of the electric field of a laser focussed into a material is comparable to the Coulomb potential experienced by an electron, then the Coulomb potential will be distorted. If this distortion can suppress one side of the potential sufficiently, then the electron can tunnel through the potential barrier, free from the bound state.

The probability of tunnelling ionisation or MPA occurring will depend upon the photon energy. MPA will dominate for photon energies close to the bandgap (e.g. TPA) and tunnelling ionisation will dominate for photon energies much lower than the bandgap.

Using quantum mechanics these two regimes can in fact be shown to be two limits of the same process, as demonstrated by Keldysh in 1965 [24]. The Keldysh parameter describes the relative contribution to photon absorption that the two regimes make. If the Keldysh parameter is less than 1.5, tunnelling ionisation dominates; if it is greater than 1.5 then MPA dominates.

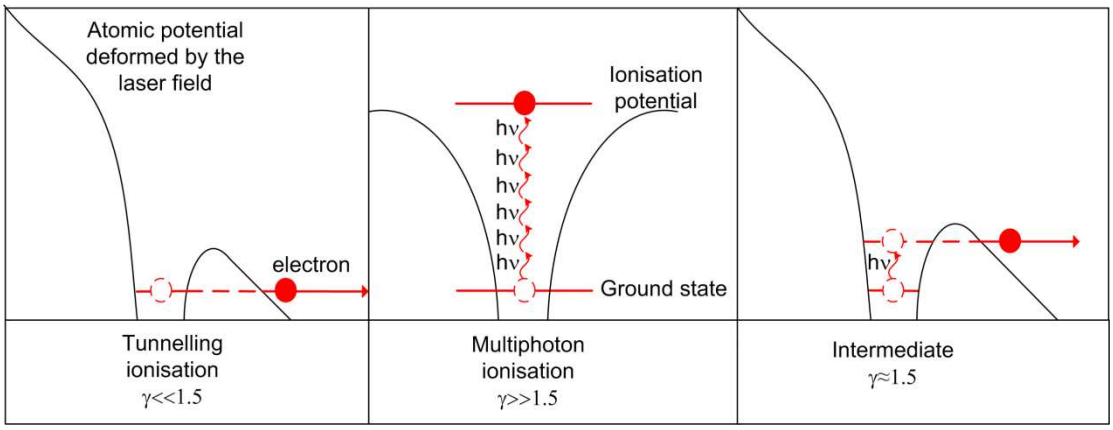

Figure 2.6. Nonlinear absorption. Left: tunnelling ionisation, the electric field of the laser suppresses the Coulomb potential of the atom allowing the electron to tunnel away. Middle: multi photon ionisation, simultaneous absorption of multiple photons occurs, the sum energy of these photons is greater than the bandgap. Right: intermediate regime, a combination of field suppression and multi photon absorption allows ionisation to occur.

Now the electron has been liberated from its parent atom, it is no longer bound and therefore free to absorb the remainder of the laser pulse linearly. Once it has gained sufficient energy through linear absorption it can impact ionise another electron, promoting it to the conduction band, this process is known as avalanche ionisation. As long as the laser field is present, these free electrons can promote more electrons to the conduction band, consequently the density of electrons in the conduction band grows exponentially. For long pulses the seed electrons for avalanche ionisation are mainly from impurities in the dielectric and from thermally excited carriers. For short pulses the majority of the seed electrons come from those ionised by the leading edge of the pulse by MPA or tunnelling ionisation.

2.3.3. **The role of electron diffusion**

The above sections have detailed how energy can be transferred to electrons from the laser. For ultrafast laser pulses (~100 fs) these processes occur substantially faster than

the energy transfer between the free electrons and the material lattice. This results in electrons with a high temperature in a cold lattice. Typically in dielectrics the diffusion of electrons is small compared to the focal spot size and so is negligible for our method of ULI.

2.4. Material changes

In this section we will concentrate on the effects within an irradiated material after the laser pulse has finished, before the next pulse is applied and while the electrons are still in an excited state. There are a range of changes that can happen on the surface of or inside the material.

2.4.1. **Ablation**

A material that has been irradiated by an ultrafast laser is left with electrons in an excited state. These electrons heat the lattice, which sublimates into a plasma. If no, or little, material surrounds this plasma then the repulsion due to the charge on the plasma causes it to expand - erupting and ejecting material. Any remaining heat diffuses into the sample. If the pulse energy is selected to be just above ablation threshold then very little heat is left to diffuse, resulting in a minimal heat affected zone (HAZ) [25].

2.4.2. **Material changes in the bulk**

Due to the nonlinear nature of the absorption, energy can be deposited inside the bulk material. In contrast to ablation, which occurs on the surface, energy can no longer be carried away through material ejection. Three qualitatively different structural changes have been reported.

For high energy exposures, explosive material expansion (similar to ablation) can occur, driving material out of the focal volume into the surrounding material. This leads to the formation of a low density ‘void’ surrounded by a high density shell of material [26].

At intermediate energy levels, a birefringent refractive index change can occur. This is the result of form birefringence from nanometre scale strips of alternating high and low refractive index [27]. These strips form after the application of many laser pulses and are orientated perpendicular to the polarization direction of the laser light. A change of polarisation of the laser results in the nanogratings being aligned in a different direction.

For fused silica the introduction of a wet chemical etchant, typically dilute hydrofluoric acid (HF), etches the modified regions many times faster than the unmodified regions. Two processes are thought to contribute to the increased etch rate: the etchant being able to ‘flow’ down the nanogratings; and strain in the material increasing etch rate. This laser assisted wet chemical etching has been used extensively for fabricating microfluidic devices [28-31].

Under the application of low energy pulses, the material in the focal volume can be structurally changed, resulting in a change to the refractive index within the focal volume. Under the correct fabrication conditions this can result in an increase in the refractive index and by translating the material through the focus in three dimensions, this index change can be extended into a waveguide [12, 32]. Waveguides fabricated using this smooth refractive index change are commonly referred to as type I ULI waveguides [33]. Typical index changes are of the order of 10^{-3} although changes as high as 10^{-2} have been reported.

2.5. Requirements for ultrafast laser inscription

The fundamental requirements for a waveguide inscription setup can be considered as a laser source capable of producing pulse energies sufficient to create smooth refractive index changes, a focussing objective and a translation stage to move the substrate through the focus. To make full use of the inherent three dimensional nature of this technique the translation stage should have movement in three axes. Figure 2.7 shows a simplified setup capable of waveguide inscription.

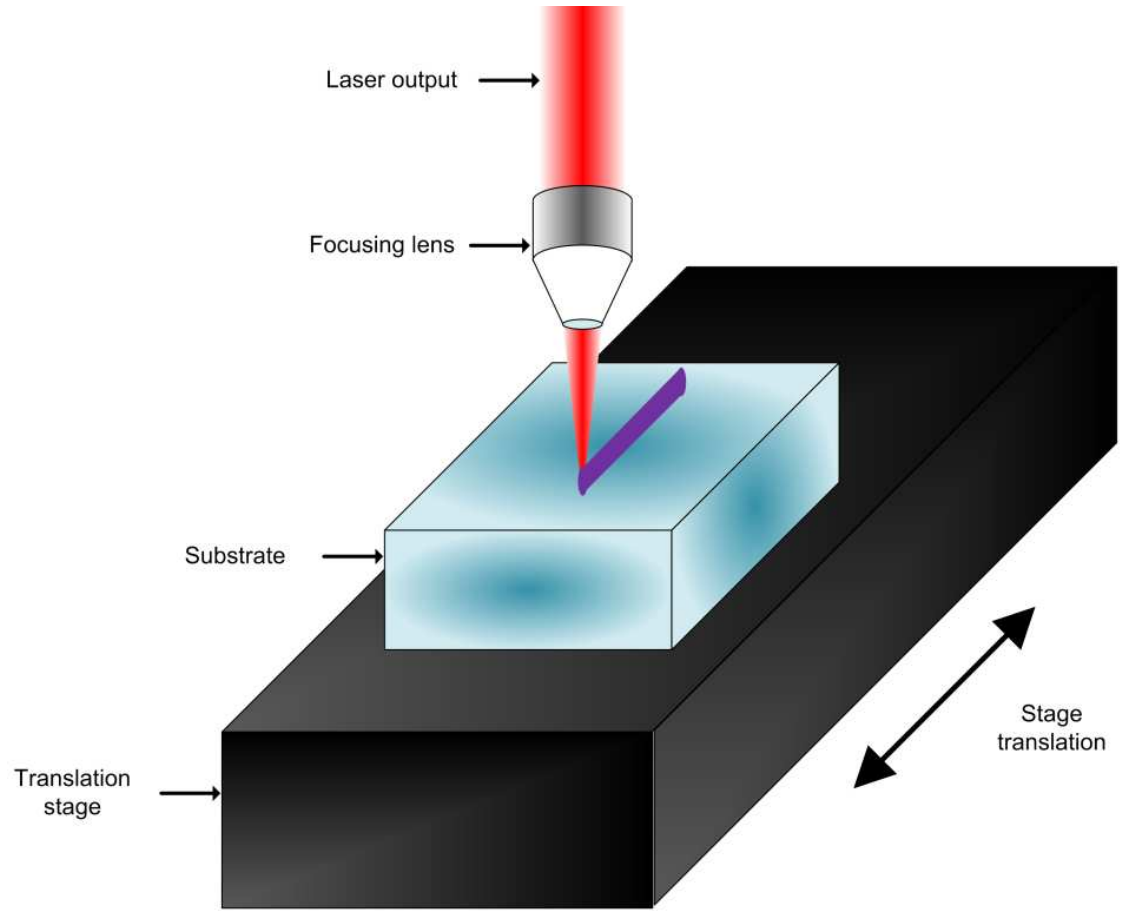

Figure 2.7. Schematic for ultrafast laser inscription.

Many parameters have been shown to directly affect the changes in the modified material. These can be parameters related to the inscription laser, the substrate undergoing inscription or the inscription setup.

2.5.1. **Laser parameters**

Pulse energy Different pulse energies result in a different quantity of energy being deposited within the material. This in turn can lead to a more complete structural change, or a completely different structural change occurring.

Polarisation The polarisation of the incident laser beam affects the efficiency of the absorption and therefore the quantity of energy deposited within the substrate. If the material has long range order (i.e. a crystal) then the polarisational state relative to the crystallographic axes can also affect

the efficiency of the absorption [34]. The polarisation of the laser relative to the stage translation can also affect the propagation losses of the waveguide, possibly due to phenomena similar to nanogratings.

Wavelength The wavelength of the inscription laser affects the relative contributions of MPA and tunnelling ionisation. The wavelength of the inscription laser can have a marked effect on the properties of the waveguides created, for example, lower loss waveguides appear to be fabricated using shorter wavelengths within fused silica (i.e. 522 nm appears to result in lower propagation losses than 1044 nm) [14].

Pulse duration The pulse duration of the inscription laser affects the efficiency of the absorption within a substrate and the proportion of this which is due to avalanche ionisation. Other nonlinear effects, in addition to absorption, occur in some materials. These will typically have different thresholds and sometimes different pulse duration dependencies. For example, with waveguide inscription within the highly nonlinear material zinc selenide (ZnSe), it is necessary to use approximately 1 ps pulses, as pulse break-up occurs with shorter pulses limiting the amount of energy deposited at the focus [35]. There has also been work showing that more complicated temporal pulse shapes, such as double pulses, can increase absorption [36].

Repetition rate If the repetition rate of the inscription laser is relatively low, then each pulse interacts with cold material. For high repetition rates a strong cumulative heating of the substrate can occur with the heat not conducting out of the focal volume between consecutive pulses [37].

2.5.2. **Material parameters**

Bandgap The bandgap of the substrate undergoing inscription dictates the energy required to liberate an electron. The bandgap in combination with the inscription laser wavelength determines the ratio of MPA to tunnelling ionisation.

Thermal properties The rate at which heat can diffuse throughout the substrate determines the degree to which heat accumulation within the substrate occurs for a given repetition rate.

Nonlinearity Effects other than absorption can contribute strongly to the propagation of the laser's electric field for the high irradiances that occur close to the focus. New wavelengths can be generated e.g. by SHG or self phase modulation, these new wavelengths may be linearly absorbed or change the ratio of MPA to tunnelling ionisation. Nonlinearity may also lead to self focussing or defocussing which can cause filamentation of the pulse, or may longitudinally shift the focus, and greatly change the irradiance at the focus [38].

Susceptibility to structural and chemical changes A multitude of structural and chemical changes have been observed in laser irradiated materials. These are generally dependent on the constituents of the material and the strength or stability of the bonds between them. Colour centres are known to form in some materials [39], but are not observed in others. Other strong photo chemical refractive index changes can occur, e.g. in GeO_2 doped silica and H_2 loaded Silica [40].

Impurities Impurities provide real intermediate energy levels within the bandgap and can provide seed electrons for avalanche ionisation. Impurities typically have a more significant effect for longer pulses with lower peak powers [41].

Symmetry Some crystals have inherent asymmetries in their structure, either favouring absorption of one polarisation, or lowering the energy needed for waveguide fabrication for one axis of sample translation. This can also lead to a non-reciprocality with respect to stage translation direction [34].

Inhomogeneity If there is a variation in material properties across different regions of the substrate, then these regions will respond differently to ULI. For example, they may have different modification thresholds and also there is the possibility of different material changes.

2.5.3. **Other inscription parameters**

Focussing objective — High numerical aperture (NA) and low NA objectives have focal regions of a different size and shape. This changes the peak irradiance for a given peak power, and also changes the nonlinear propagation of the pulse.

Inscription geometry — Translation of the substrate parallel to the inscription laser propagation direction will result in a symmetrical waveguide cross section. However the waveguide length will be limited by the working distance of the objective. Sample translation perpendicular to the inscription laser propagation typically results in an asymmetric cross section. This will be discussed in greater detail later in this chapter.

Spatio-temporal pulse effects — Pulse front tilt and spatial chirp have been shown to change the absorption within a substrate, as the bandwidth of the pulse at different positions within the material will vary. They can also lead to non-reciprocality with respect to stage translation direction for transverse translation directions parallel and anti-parallel to the pulse front tilt [42].

Translation speed — For fast translation speeds there is less overlap of subsequent pulses. If the translation speed is slow then an increased pulse overlap occurs [43]. If we operate in a low repetition rate regime, then by maintaining the product of the translation speed and the repetition rate, the inscribed waveguides will be identical. If we operate in a high repetition rate regime then the effect on the waveguides of varying the translation speed is more complicated [44].

Over scanning — By repeatedly scanning over the same region (over scanning), or scanning over a slightly offset region (multiscan) it is possible to slowly build up a refractive index profile. This may allow a greater index change than would be possible for a single scan (over scanning) [45], or tailor the waveguide cross section (multiscan) [46].

Clearly many parameters have a direct effect on the nature of the inscribed material modification. The links between some of these parameters have simple relationships in certain regimes, e.g. translation speed and repetition rate in a low repetition rate regime. But more generally they are coupled via complicated relationships. Given a parameter space of more than 16 dimensions, it is necessary to attempt to hold most of these constant while investigating the effects of independent changes to only a few. Typically many regions of the parameter space may be capable of creating acceptable waveguides for many applications. For example, both regeneratively amplified Ti:sapphire lasers with a repetition rate of 1 kHz and extended cavity Ti:sapphire oscillators with a repetition rate of 40 MHz are capable of producing acceptable waveguides, but other inscription parameters must be adjusted accordingly. For the work in this thesis many of these parameters will be held constant, either due to a requirement of the substrate for a particular application (leading to certain material properties), or the difficulty of varying them with the equipment available (a laser system is generally designed to operate at a fixed wavelength, repetition rate, pulse duration etc.). However, any investigation within a material will vary at least the pulse energy, polarisation and substrate translation speed. The subtleties of some of the parameters will be explained in more detail later in this chapter.

2.6. Ultrafast laser inscription configurations

Two fabrication setups were used for the work presented in this thesis, which will be referred to throughout the body of the text by the name of the company who manufactures the laser system. Both inscription setups are similar, but due to their importance in this work some details should be given on each fabrication setup.

2.6.1. **IMRA®**

The laser is an IMRA® FCPA μJewel D400. The laser features a fibre oscillator and preamp followed by a pulse picker. The pulse picker can vary the repetition rate between 0.1 and 5 MHz before inputting the light into the power amplifier stage. An average power of more than 500 mW is available throughout the repetition rate range. The laser features an adjustable compressor, allowing the linear chirp on the pulse to be partially or fully removed. This allows pulses as short as 350 to 450 fs over the repetition rate range or for longer, chirped pulses, up to 2 ps. The laser output is centred on 1045 nm and has a bandwidth of 10 nm (FWHM).

2.6.2. **Fianium®**

The laser is a custom built variable repetition rate master oscillator power amplifier ytterbium fibre laser system. The laser architecture is similar to the IMRA® but the compressor is factory set. The repetition rate range is from 200 to 700 kHz and the average power is about 700 mW. Without the adjustable compressor, pulse durations vary with the repetition rate, between 300 and 450 fs. The laser operates at 1064 nm with a 10 nm bandwidth (FWHM).

2.6.3. **Inscription configuration**

Both laser systems produce linearly polarised light which is attenuated by a half waveplate and polarising beam splitter combination. This light can then be rotated by a second half waveplate or made circularly polarised by a quarter waveplate if required. The rotation mounts for both half waveplates and the quarter waveplate are controlled via a computer. This same computer also controls a mechanical shutter and a set of high precision x-y-z air bearing translation stages made by Aerotech® (ABL1000), see Figure 2.10.

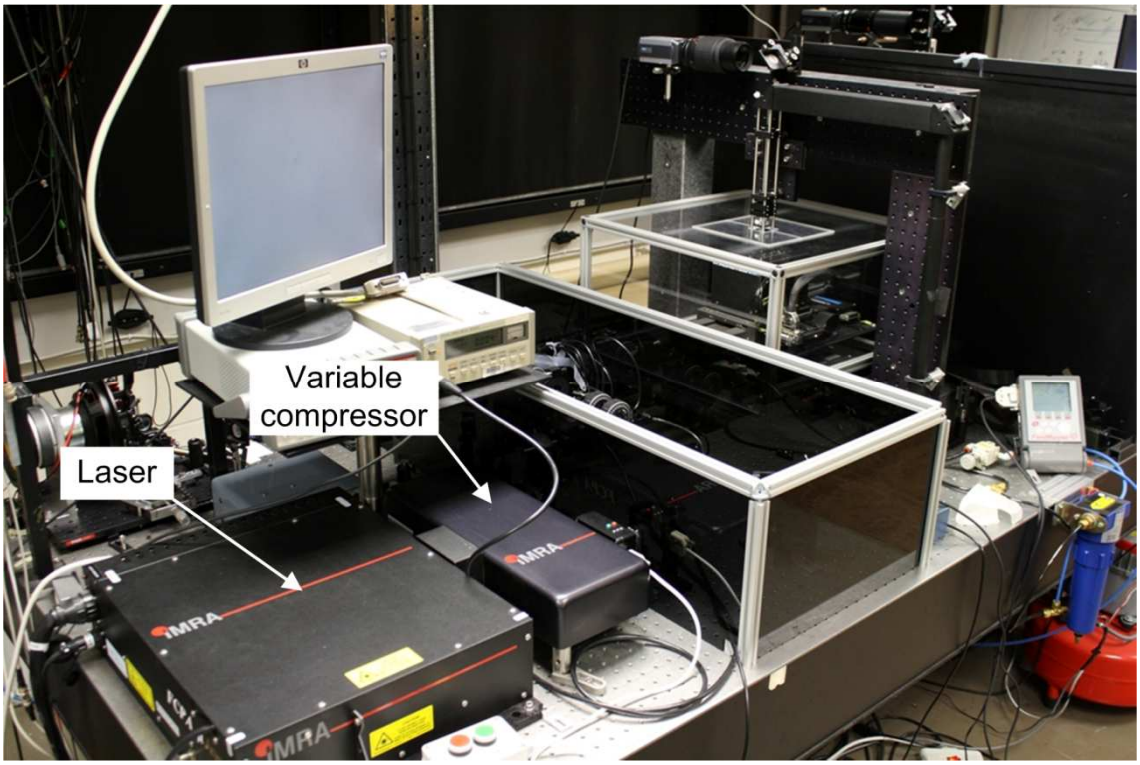

Figure 2.8. The IMRA inscription setup: laser and compressor.

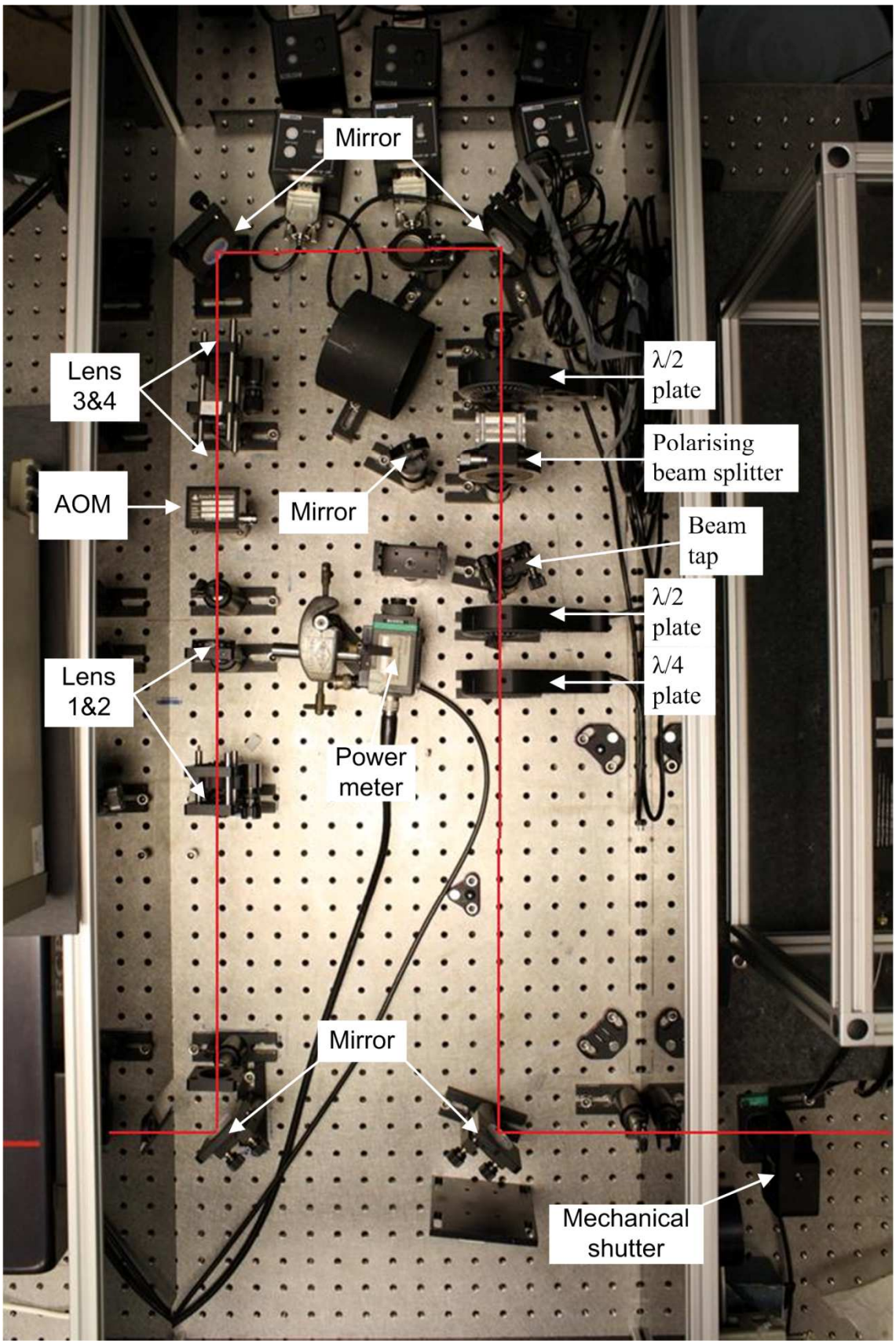

Figure 2.9. The IMRA inscription setup: beam path including acousto-optic modulator (AOM), symmetric telescope (Lens 1, 2, 3 and 4), power control (λ/2 plate, polarising beam splitter, beam tap and power meter), polarisation control (λ/2 plate and λ/4 plate) and mechanical shutter.

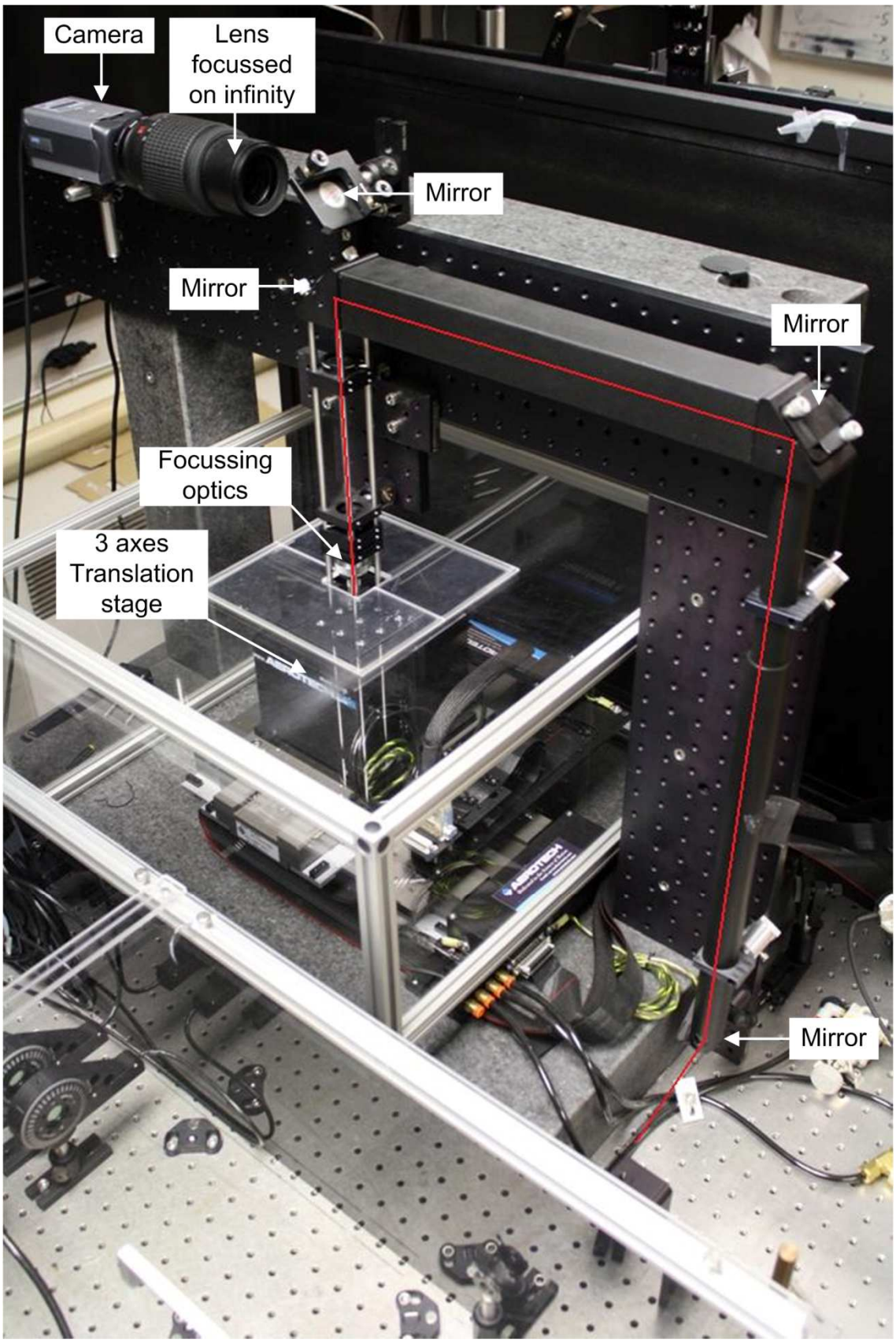

Figure 2.10. The IMRA inscription setup: beam path and focussing optics, including imaging system.

2.7. Further discussion of the fabrication parameters

This section will look at some of the inscription parameters in greater detail, focussing on the waveguide inscription geometry and techniques for control of the waveguide cross section.

2.7.1. **Inscription geometry: Longitudinal vs. Transverse**

As previously mentioned, the inscription geometry can play a key role in the resulting waveguides. For a simple explanation we will make a few assumptions, this involves a significant simplification but is only intended to illustrate the role of the inscription geometry in the waveguide writing process.

For this section we will employ the ray matrix method for Gaussian beam propagation, using Matlab®, to focus a laser that outputs 1 μm light with a typical inscription lens into a substrate with a refractive index of 1.5. The lens will be modelled using the thin lens formula, with spherical and all other aberrations ignored as well as nonlinear effects, thermal diffusion and heat accumulation. The input beam has a waist of 2.4 mm (radius to $1/e^2$) and the focal length of the lens is 4.5 mm. The 1 mm thick substrate is positioned 100 μm before the focus.

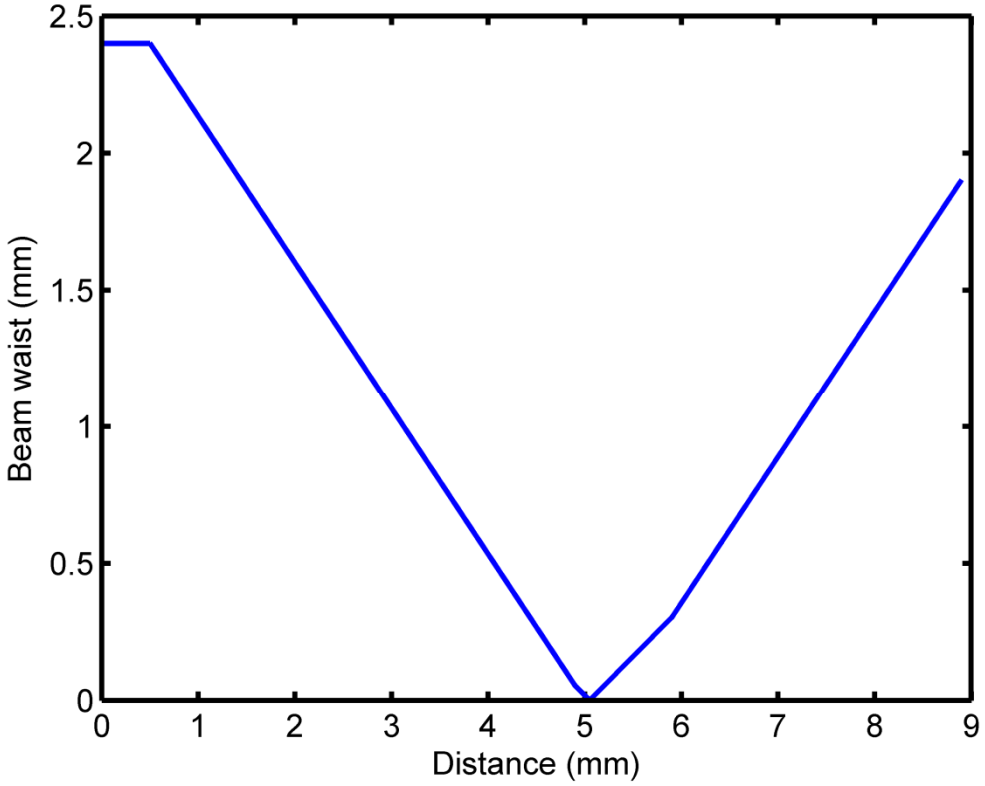

Figure 2.11 Propagation of the inscription laser beam, focussed 100 μm below the surface of a substrate with a refractive index of 1.5.

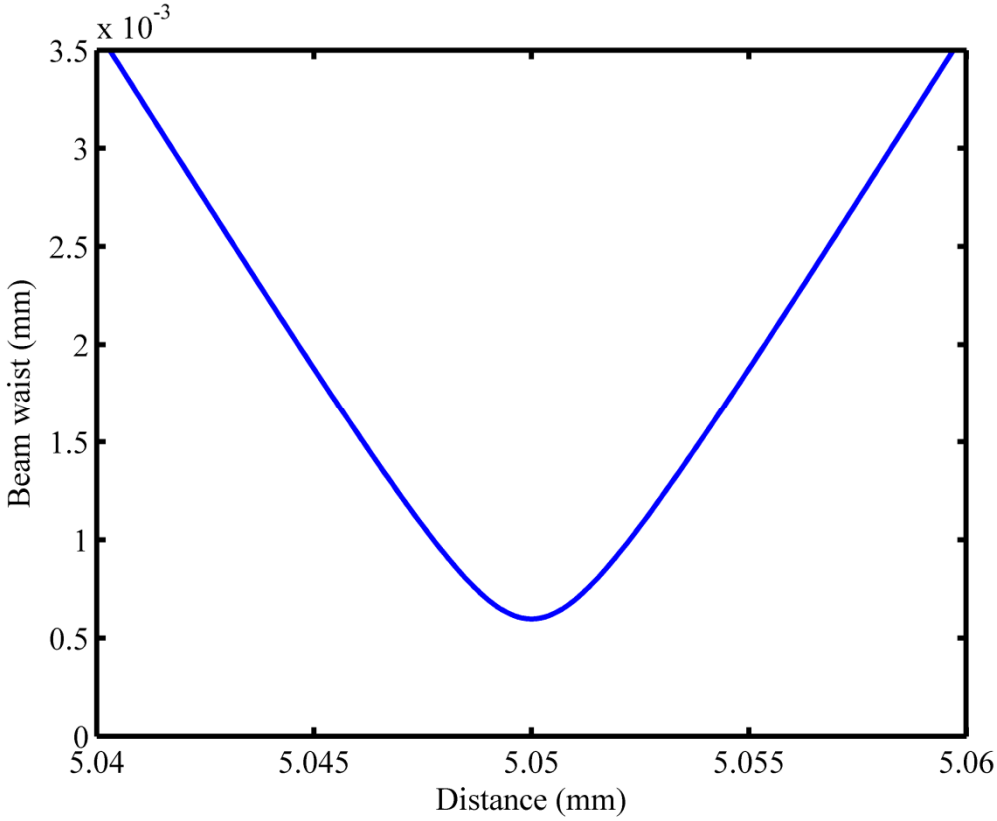

Figure 2.12 Propagation of the inscription laser beam inside the substrate close to the focus.

If the pulse energy is selected such that the modification threshold is $1/e^2$ of the peak irradiance, and sufficient pulses are incident on the material to completely saturate any index change, then any region at which the irradiance is greater than I_0/e^2, where I_0 is the peak irradiance, will be modified. This gives a spot size at the focus of 1.2 μm and a distance on axis of 8 μm over which the beam remains at an irradiance greater than I_0/e^2. Figure 2.13 presents this volume of modified material, or voxel, as viewed from along the laser propagation axis (z), and from the two axes orthogonal to this (x,y).

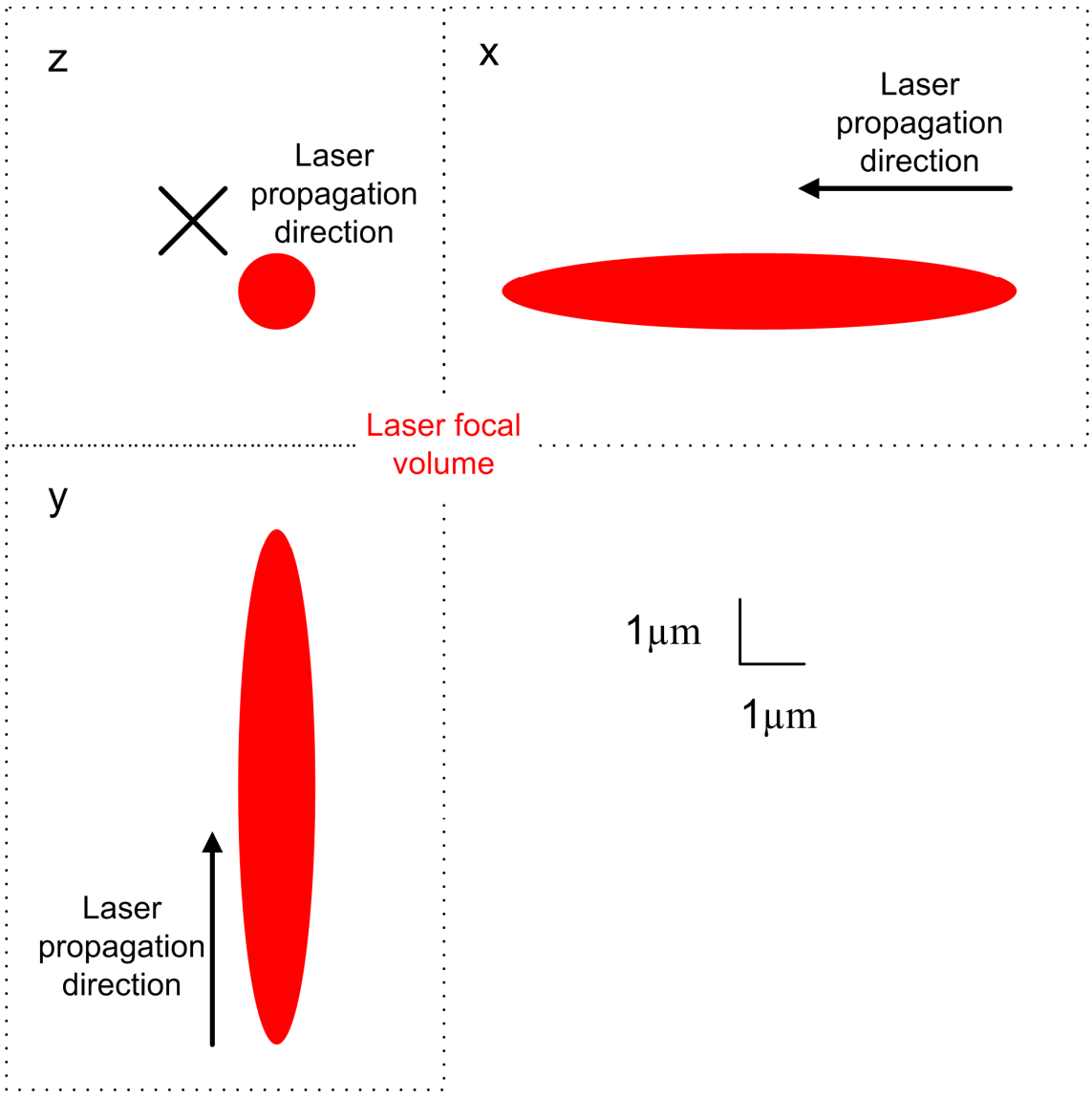

Figure 2.13. The $1/e^2$ focal volume created by a beam of 2.4 mm radius focussed by a lens of f = 4.5 mm as viewed from 3 different positions: z is viewed along the laser propagation direction, x and y are orthogonal to this.

Although ULI is a highly nonlinear process, so the linear focal volume is not directly relevant, it is clear that stage translations along the z axis (longitudinal inscription) will

result in a symmetrical cross section, while stage translations along either of the other axes (transverse inscription) will result in an asymmetry in the modified region. Furthermore, decreasing the NA of the focussing lens will result in an increase in the asymmetry.

2.7.2. **Longitudinal inscription geometry**

The inherent symmetry in the cross section of waveguides inscribed along the laser propagation axis makes this inscription geometry seem preferable. However it has two main failings:

1. Useful devices often require bends in the waveguide and therefore the structure will gain an asymmetry. This can be alleviated by minimising the angle between the waveguide axis and the laser propagation axis.
2. The waveguide length is inherently limited to the distance you can translate the sample, in this geometry that is limited by the working distance of the lens.

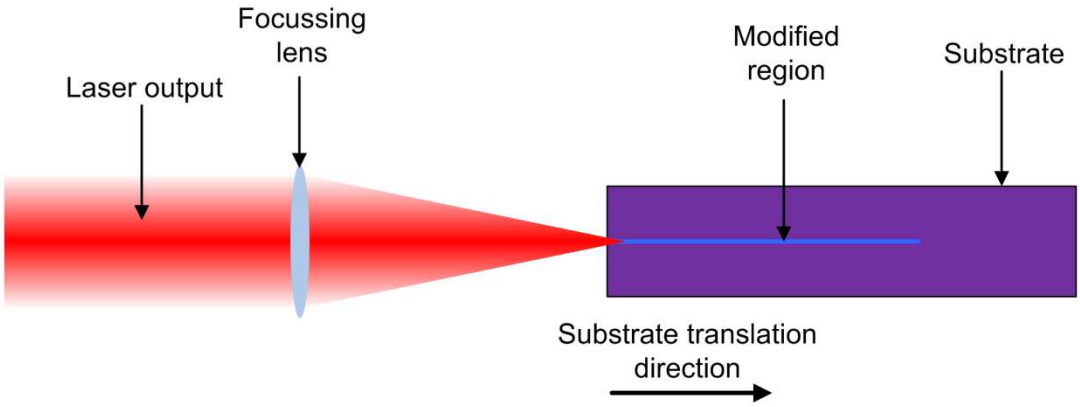

Figure 2.14. Longitudinal inscription geometry. Device length limited by the working distance of the focussing lens.

Multi-element lens designs can allow for longer working distances than are attainable with single element lenses - for a 0.5 NA lens you are still in practice limited to about 12 mm [47]. The other concern with this inscription geometry is that the degree of spherical aberration changes as the substrate is translated, this in turn alters the irradiance and therefore potentially the guiding properties of the waveguide along its length. For these reasons the majority of work has been concentrated on transverse

geometry waveguide inscription, despite the additional technical challenge required to eliminate waveguide asymmetry.

Also of note is the inscription of waveguides where focussing is carried out with an axicon. An axicon is a conical lens which allows for the creation of a transverse intensity profile which follows a zero order Bessel function as it propagates close to the focus (a donut shaped beam). Bessel beams are known for their quasi-non-diffracting nature, keeping a sharp focal spot (a few microns wide) over long distances (a few cm). This allows for the inscription of 1cm long waveguides without stage translation, either with a single pulse of sufficient energy or with multiple pulses [48]. Despite the fast processing times attainable for single shot waveguide writing, this technique poses serious limitations on the geometry of the device, even simple curves are difficult to achieve.

2.7.3. **Transverse geometry**

Using a transverse geometry for inscription removes any limitations on the waveguide length, other than the travel of the translation stages. It also does not suffer from issues relating to changes in focussing from differing degrees of spherical aberration, as the focussing is always to the same depth within the material. Waveguide bends within the x-y plane (orthogonal to the laser propagation direction) also maintain a constant cross section, this is, however, generally asymmetric.

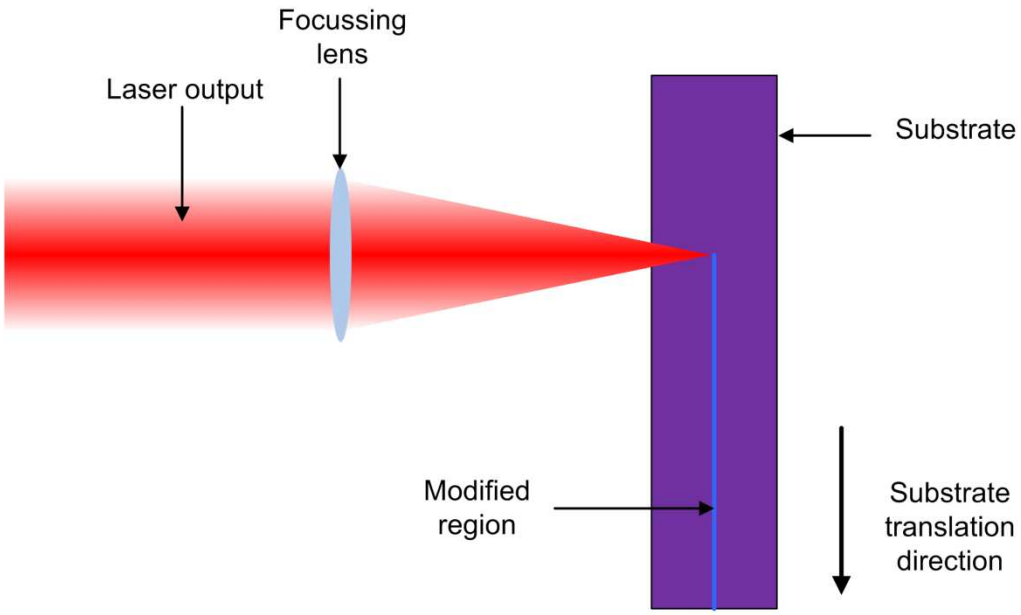

Figure 2.15. Transverse inscription geometry. Device length not limited by working distance of focussing lens.

2.7.4. **Waveguide cross section symmetry correction**

Several techniques exist for the correction of the cross sectional asymmetry present in waveguides inscribed using the transverse geometry of ULI.

High NA Objective

If the NA of the lens used is sufficiently high (~1.4 for a material with n = 1.4) then the focal volume is inherently almost spherical and as such the waveguide cross section is symmetrical. This holds for any inscription direction, allowing bends to be written and waveguide inscription to be carried out in arbitrary directions. The main issue with this technique is that the modified region may become very small, and due to the small index change commonly observed for ULI, small waveguide cross sections lead to high propagation losses, as the majority of the energy of the guided mode is guided in the cladding region. Given a material capable of sufficient index change this method would appear ideal for fabricating waveguide circuits.

Cylindrical telescope

R. Osellame *et al*. demonstrated that by placing a pair of cylindrical lenses in the path of the inscription laser, prior to the focussing objective, an astigmatism in the beam could be generated [49]. This results in different focussing conditions for the two axes, parallel to and orthogonal to the sample translation direction. By changing the distance between the cylindrical lens pair, the degree of astigmatism can be varied to create an almost circular waveguide cross section. This technique corrects waveguide asymmetry for waveguides inscribed along one axis only, to write a waveguide along the other transverse axis the cylindrical telescope must be rotated. Practically this is of little importance for any bends which keep the waveguide axis near-parallel to the axis along which the asymmetry has been corrected for.

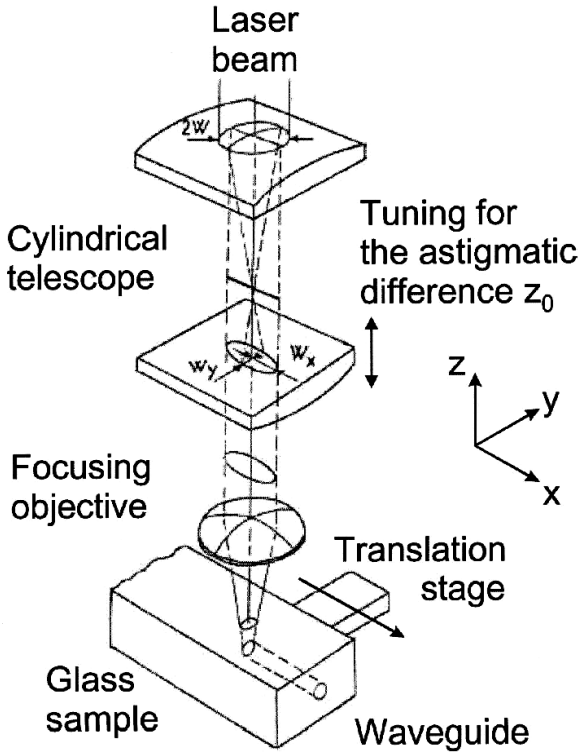

Figure 2.16. Schematic of setup for astigmatic waveguide shaping taken from Osellame et al. [49].

Slit technique

Shortly after the invention of the cylindrical telescope technique, M. Ams *et al.* proposed a technique to achieve a similarly shaped focal volume by placing a slit in front of the focussing lens [50]. Provided the slit is sufficiently close to the lens, then

the inscription laser under-fills the lens along one axis while properly filling it along the other. This results in a different NA for the two axes. This in turn means you can correct a waveguide asymmetry for inscription along an axis parallel to the slit with similar restrictions to the cylindrical telescope technique for writing bends in the waveguide. In comparison to the cylindrical telescope technique, this technique requires you to block some of the laser beam by obstructing it with the slit, reducing the laser power. However, it requires only one element, as opposed to two cylindrical lenses, and the slit's position is only alignment critical in one axis; potentially making this a simpler technique.

Deformable mirror

Early in my PhD, I worked with R. Thomson *et al*. to show that by placing a deformable mirror before the focussing objective, a spatially dependent phase can be placed on the light focussed through the objective, and therefore alter the shape of the focal region [51]. Despite this technique's technological complexity, the optical alignment is no more difficult than with a slit, and given sufficient investigation, could allow on the fly waveguide cross sectional correction. This technique should also allow for some control of the degree of spherical aberration caused to the beam, as it is focussed through different amounts of substrate.

Multiscan

Another technique for waveguide cross section control relies on the ability to stitch together regions of index change to create a near homogeneous modified area larger than any single region. Nasu *et al.* first demonstrated this technique in 2005 [46], the same year that Ams *et al.* first demonstrated the slit method of focal volume control. This technique differs from the other techniques described in this section, in that it uses the asymmetry to gain access to an additional control parameter. With the other techniques, fabrication of a waveguide requires a single scan of the substrate through the laser focus, for the multiscan technique this process creates the first 'scan' of modified material, the substrate is then moved a small amount in the direction orthogonal to both the laser propagation direction and the waveguide axis. The substrate is then translated through the focus again creating a second scan, slightly offset from the first. This process is repeated many times, often for 20 scans, until the cross section is symmetrical. Interestingly, this leads to an almost square cross section, as opposed to

the near circular cross section obtained by the other asymmetry compensation techniques. The waveguide height, which is parallel to the inscription laser propagation direction, is determined by the confocal parameter of the focussing objective, whereas the waveguide width is determined by the number of scans and the scan separation. In this way the multiscan technique decouples the waveguide height from the waveguide width. This technique can easily be implemented for curved waveguides or straight waveguides in any direction within the transverse plane. Since the multiple scans often have a large degree of overlap, it is not necessary to achieve the full index change required within one scan. This lowers the required pulse energy and can allow modification of materials where the damage threshold is close to the index modification threshold. The main disadvantage of this technique is the increased processing time - the waveguide must be built up from multiple scans, making this technique many times slower, assuming the translation speed used for a scan is the same as that used for single scan inscription.

Also of note is the multiscan technique's applicability to the selective chemical etching of fused silica. For fabrication of microfluidic channels, the multiscan technique can be used to 'paint' the material to be removed before the introduction of HF to etch the irradiated material [28].

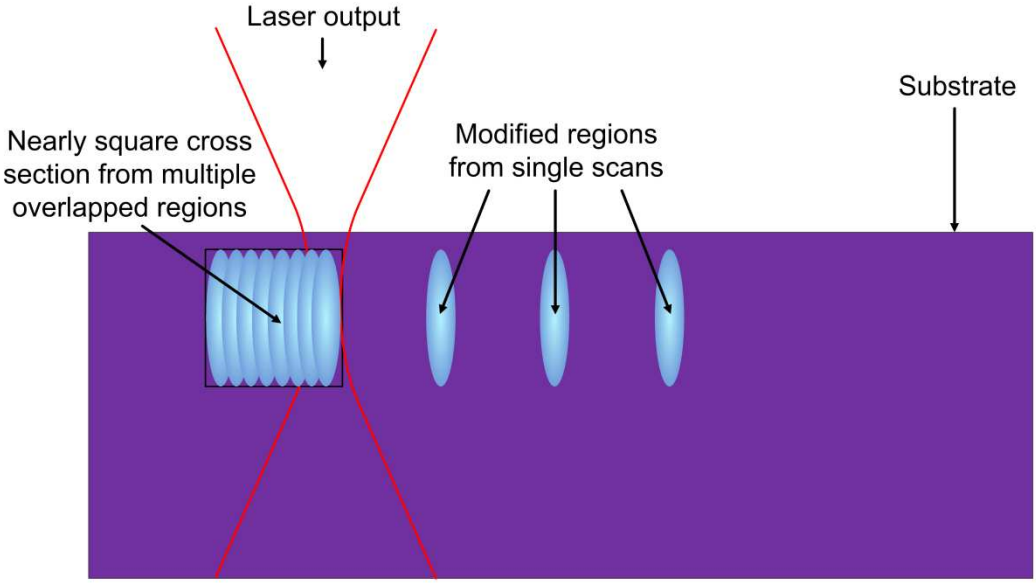

Figure 2.17. The multiscan waveguide fabrication technique, the cross section of the waveguide on the left is built up from multiple asymmetric modified regions.

Heat accumulation

All of the waveguide shaping techniques detailed up to this point have assumed we are operating in a low repetition rate regime, where each pulse is incident upon cold material and negligible thermal diffusion occurs. If the repetition rate is raised so that the inter-pulse time becomes comparable with the time required for heat to diffuse out of the focal volume, then the modified region ceases to bare resemblance to the shape of the focal volume of the inscription laser [37]. In a high repetition rate limit the laser can be viewed as providing a point source of heat inside the substrate, cumulative heating occurs over many pulses and the size of the melted region grows with each pulse. In this limit the modified region is dependent on the translation speed, as the size of the modified region is proportional to the number of pulses used to heat an element of material. Using heat accumulation to control the waveguide cross section has the benefit of producing inherently symmetrical cross sections, and the region's size can be easily tailored. This regime does however have limitations - the modification mechanism is completely different to that of low repetition rate ULI, so waveguides may be produced with one regime but not with the other for a particular material. Some materials have a sufficiently high thermal conductivity that the pulse energies and repetition rates are high, leading to the requirement for high average power laser sources.

2.8. Type I waveguide inscription

In Section 2.4.2, waveguides inscribed relying on the smooth index change mechanism from comparatively low pulse energies were referred to as type I ULI waveguides. There is, however, another class of ULI waveguides.

2.9. Type II waveguide inscription

In 2004 type II waveguide inscription was proposed and demonstrated by Nolte *et al.* [52]. For this technique the role of the laser absorption is to create regions of catastrophic optical damage in the material. If the region of the substrate that absorbs the light expands, such as when amorphising an initially crystalline material, then the material near this region will become strained. The refractive index of a strained material is different from that of unstrained material due to the strain-optic effect [53], and hence it is possible to guide light down strained material close to the damaged regions.

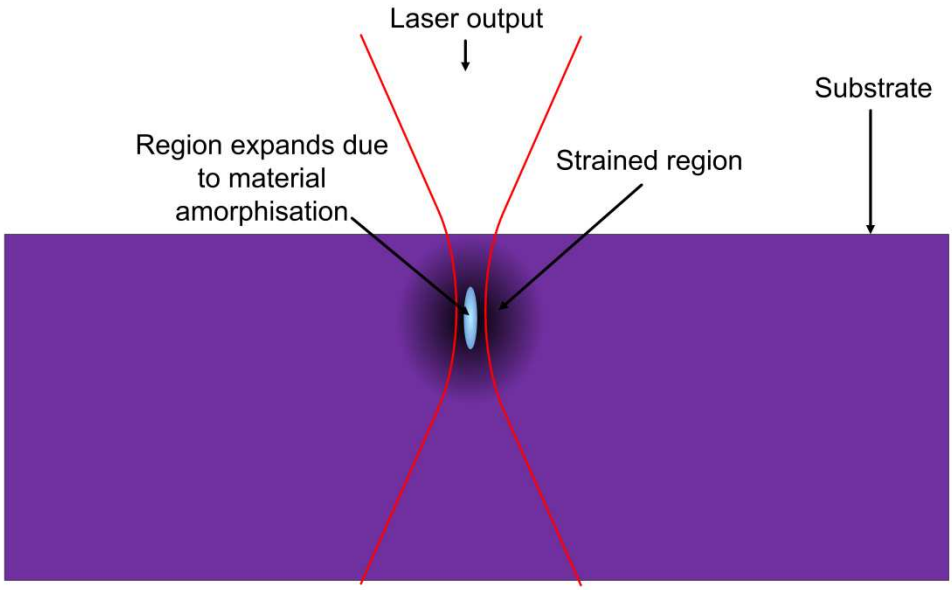

Figure 2.18 Type II waveguide inscription. Energy is deposited in the focal volume causing material expansion. Surrounding material is strained and so changes its refractive index via the strain-optic effect.

This technique is often used in crystals where type I direct index modification can be difficult and has the benefit that the material where the guiding takes place has not been exposed to the inscription laser and as such should possess properties nearly identical to unmodified material. Several possible disadvantages include the sometimes unpredictable nature of the guiding regions, they can be highly polarisation dependent and can be shaped by the interaction of the strain fields generated by more than one damage line. It is however an important class of ULI waveguide writing for work in crystals and hard glasses. This process has been most heavily utilised in doped crystals for laser applications [54-56], and nonlinear crystals for second harmonic generation [33, 57, 58], although work in lithium niobate - due to it's electro-optic properties - has also been undertaken using type II ULI [59].

2.10. ULI: previous successes and future developments

Ultrafast laser inscription has been used successfully for the fabrication of waveguides in a wide range of glasses including silica [14], phosphate [49], bismuthate [60], chacogenide [38], microscope slides [32], and borosilicate [37]. It has also been applied to ceramics [61], polycrystals [35], and crystals, including Nd:YAG [62], Yb double tungstates [54], lithium niobate [33, 57, 63], and KTP [58]. However, it has several drawbacks in comparison to more established techniques. Propagation losses for ULI

waveguides are normally of the order of 0.1-1 dB/cm, and can be significantly higher in some materials. ULI is a serial process (as opposed to lithography which can produce many devices in parallel) and this limitation, in addition to the relatively high propagation losses and the number of variables that must be closely controlled, results in difficulties in its application to mass production. This also restricts ULI from competing with some, already commercialised, fabrication techniques for simple straight waveguide structures. It is therefore important to identify fields where ULI can accomplish what other technologies cannot, for example, through rapid prototyping a device before a commercial development, or low volume runs of devices (see Figure 2.19) [64]. It can also be integrated with other technologies [65], or other facets of the same technology [66], and allow waveguides to be fabricated in new materials for which other waveguide fabrication techniques have not yet been developed [35]. Another key area is in the exploitation of the truly three dimensional nature of ULI (see Figure 2.20-Figure 2.22) [32, 67]. Some interest still remains in investigating new materials, as there may still be a perfect material for ULI, which would allow the consistent and rapid fabrication of high quality waveguides, at a price which makes this technology economically viable.

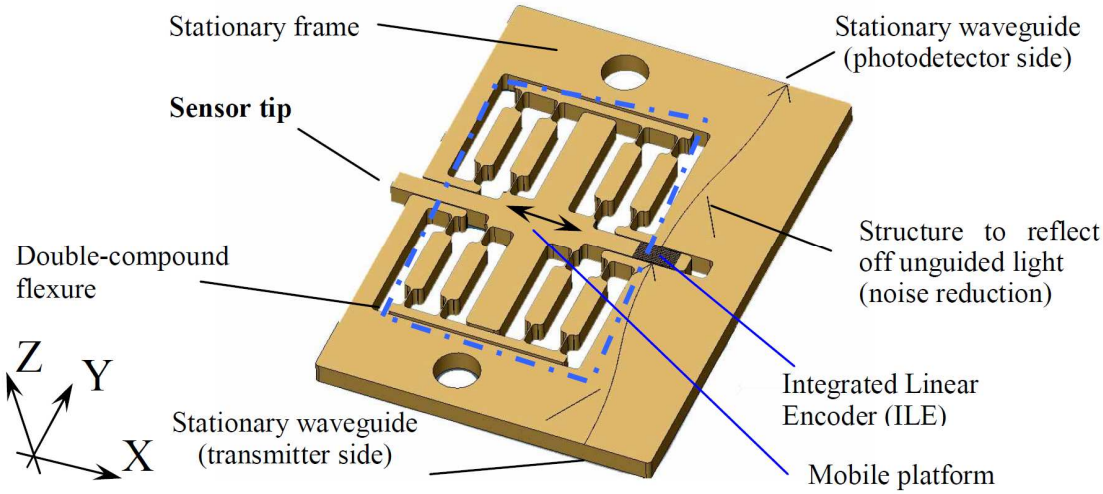

Figure 2.19. Diagram of a monolithic, optically encoded displacement sensor fabricated by Bellouard et al. The device features fused silica flexures created by the selective removal of substrate material and a pair of waveguides which meet a waveguide array inscribed in the moving section of the sensor. Figure and labels taken from [64].

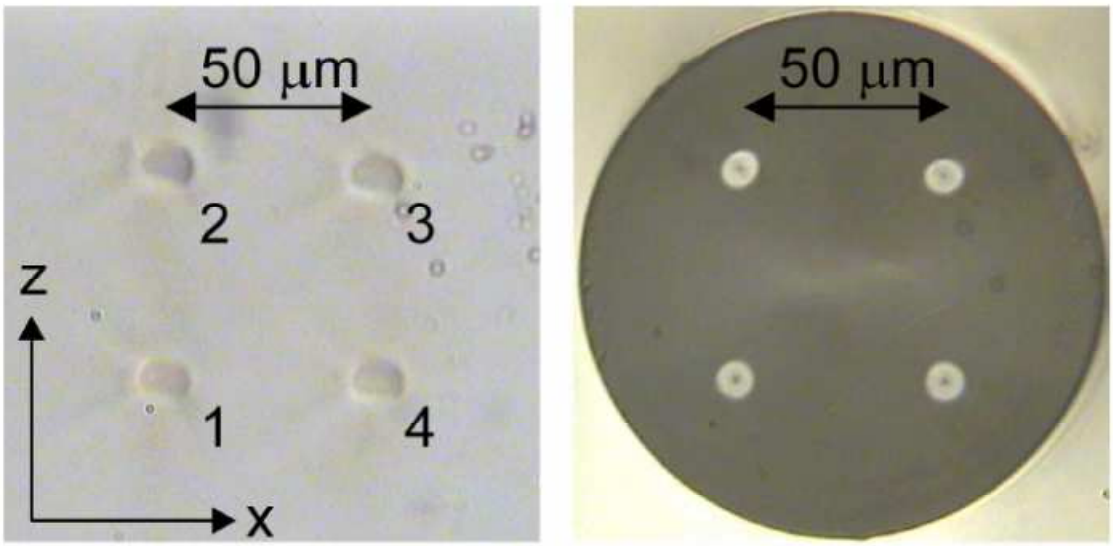

Figure 2.20. Left: near field optical micrograph of the multicore fibre coupling end of an ultrafast laser inscribed fan out inscribed by Thomson et al. This side of the waveguide has a core geometry matched to a multicore fibre, the other side of the waveguide has a core geometry matched to a standard telecoms fibre v-groove array. Right: near field optical micrograph of the multicore fibre to which the waveguide couples. This figure has been taken from [32].

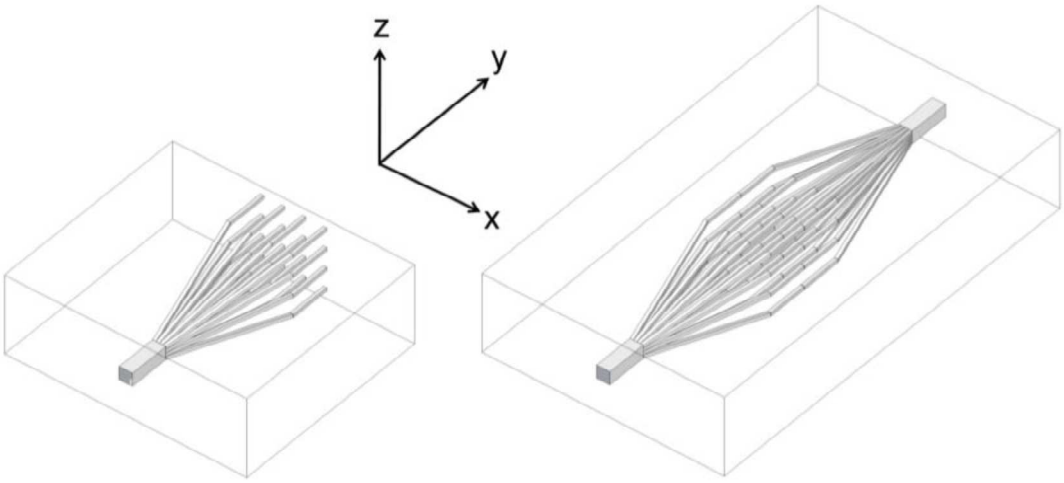

Figure 2.21. Left: sketch of a multimode to single mode integrated photonic lantern transition inscribed by Thomson et al. Right: sketch of a multimode to single mode to multimode transition created by inscribing two photonic lanterns. This figure has been taken from [67].

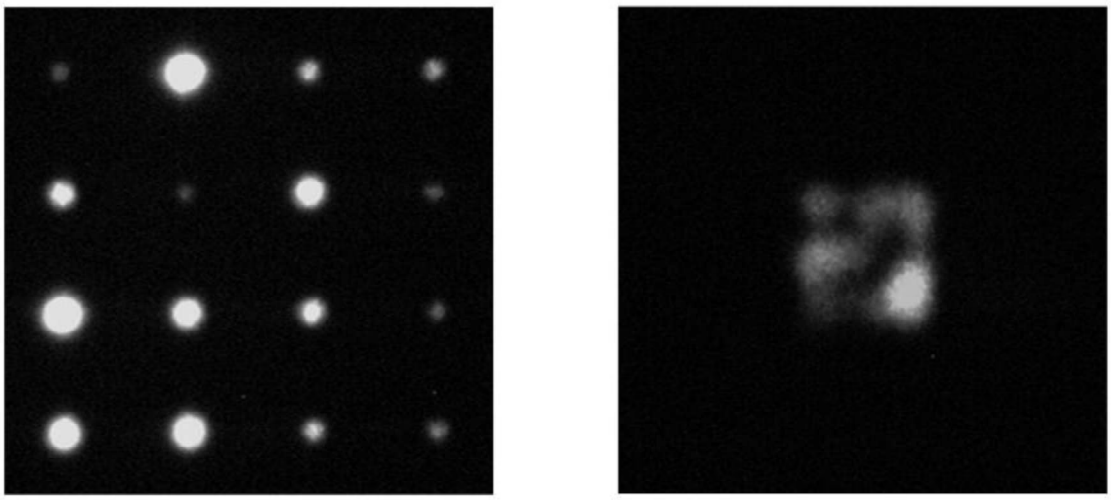

Figure 2.22. Left: the modes from the single mode array end of the photonic lantern. Right: an image of the mode from the multimode end of the waveguide. This figure has been taken from [67]

In this chapter we have considered light matter interactions, including the absorption of sub-bandgap radiation. We have qualitatively discussed the material changes that may manifest if sufficient energy is deposited within a small volume of the substrate and reviewed the role different inscription parameters can play in the resultant structures. Different waveguide writing geometries have been considered and methods of alleviating some weaknesses of these geometries have been stated. The waveguide fabrication setups used for the experimental part of this thesis have been presented and finally some devices highlighting the uniqueness of this technology have been discussed.

In chapter 3, I will demonstrate how ULI can be used to create sensing elements by, firstly showing how in a single stage ULI can fabricate a side-polished fibre-like device that has the potential to be integrated into an evanescent field sensor. I will then show how ULI can be used to write waveguide Bragg gratings in planar fibre for bend sensing.

Chapter 3. Sensors

Fibre sensing has become a major industry, despite the fact that optical fibres are designed to inherently limit the effect of the external environment upon the light propagating through them [68]. Consequentially, post fabrication adaption of the fibre structure is often undertaken to allow interaction of the light with the external environment. Light can then interact directly with the environment, or changes to the fibre can occur, which in turn change some property of the guided light. The two devices detailed in this chapter are based on two different classes of fibre sensor, but both benefit from the inherent simplicity of the ULI process - they can be fabricated in a single step - and could be built into networks with other components that have been developed with ULI. This would allow for the production of compact, single chip devices with the functionality of systems built out of many tens of fibre components, fusion spiced together.

3.1. Fibre Sensors

The first sensing element presented in this chapter is based on the design of a side-polished fibre. These sensors allow the guided mode to directly interact with the environment around the fibre. The second waveguide sensor described is an array of waveguide Bragg gratings. Bragg gratings rely on a resonant reflection from the interference of multiple periods of high and low refractive index. This has the effect of the peak wavelength of the reflection from the grating being shifted by changes to the temperature of and strain on the fibre.

3.1.1. Side-polished fibres

By taking a piece of standard optical fibre and removing a section of cladding by chemical mechanical polishing, the evanescent field of the guided mode can be exposed to the environment over a defined length, see Figure 3.1. This piece of fibre can then be used as a sensor. If the sensing region is surrounded by an absorbing gas or liquid, then a loss of optical power in the guided mode occurs due to the absorption. Alternatively a change in the refractive index of the medium surrounding the polished section of fibre causes a change in the effective index of the guided mode. By placing this sensor in one arm of an interferometer, the change in the effective refractive index of the mode can be measured. Due to the complexity of their manufacture, side-polished fibres have been

largely superseded by taper methods for exposing the evanescent field of the guided mode to the environment.

Figure 3.1. Schematic of a side-polished optical fibre, a section of the cladding (blue) has been removed by chemical mechanical etching to leave the core (red) in close proximity to the external environment.

3.1.2. **Fibre Bragg gratings**

Fibre Bragg gratings (FBGs) are among the most heavily utilized fibre sensors and have largely displaced their electrical counterpart, the strain gauge, for many applications [68]. Their mode of operation is similar to that of a dielectric mirror - through creation of a longitudinally periodic refractive index modulation, a highly reflective 'mirror' can be created, even with only a small modulation in the refractive index [69], see Figure 3.2. The reflectivity of a Bragg structure is a function of the wavelength of light, with the wavelength resonant to the structure being highly reflected and other wavelengths transmitted.

$$2d \sin \theta = n\lambda \qquad (11)$$

where d is the grating separation, θ is the angle to the grating plane (i.e. 90^o for normal incidence), n is the refractive index and λ is the free space wavelength of the radiation. For normal incidence the Bragg condition is satisfied when $2d=n\lambda$ [70].

For a multimode fibre, different transverse modes have different propagation constants and therefore different effective refractive indices. Therefore the Bragg condition will be satisfied by a different wavelength for each transverse mode of the fibre. For this reason FBGs are generally only of use in single mode fibres.

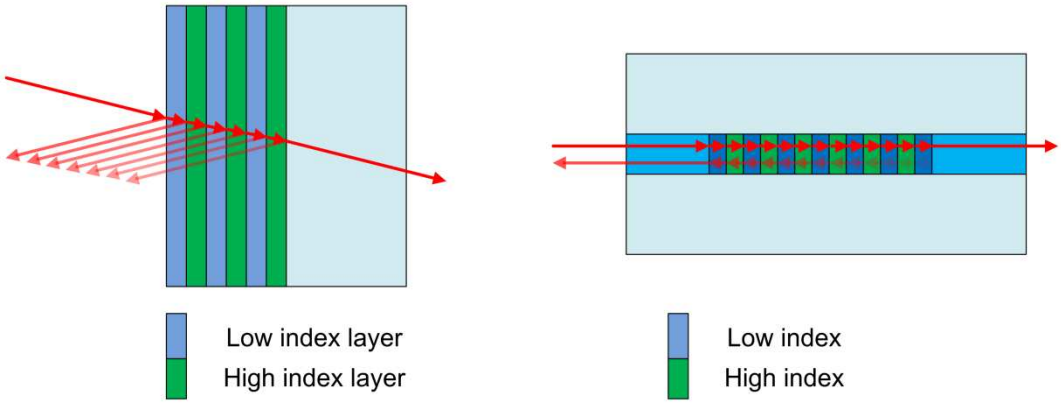

Figure 3.2. Left: a dielectric mirror: by alternating layers of high and low index a structure highly reflective to a wavelength corresponding to the Bragg condition can be created. Right: a section of fibre Bragg grating: a longitudinal modulation of the core index allows coupling between the forward propagating fundamental core mode and the counter propagating fundamental core mode for a wavelength corresponding to the Bragg condition. Similar conditions also exist for higher order modes.

The functionality of FBGs as sensors is derived from their sensitivity to strain (fractional change in length) parallel to the fibre axis, and temperature changes. This can be understood by considering the change in the wavelength satisfied by the Bragg condition if the fibre is uniformly strained. Extension of the fibre results in each high index region and low index region extending, thus shifting the Bragg condition to a longer wavelength. To a first approximation, the shift in the wavelength of the reflection peak of an FBG is expected to have a linear dependence on the strain on the device. The temperature relationship is more complicated, as temperature increases most materials expand, increasing the length of the high and low index regions. The refractive index also changes by an amount dictated by the thermo-optic coefficient of the material. For standard FBG's fabricated in SMF-28 for a reflectivity around 1550 nm, a wavelength shift of the reflection peak of 9-12 pm/ ºC is expected when operating close to room temperature [71].

One limitation of FBGs is the inherent inability to discriminate between temperature and strain changes. This can be solved using several methods, most relying on mounting multiple FBGs in complex arrangements, see Figure 3.3 for one example.

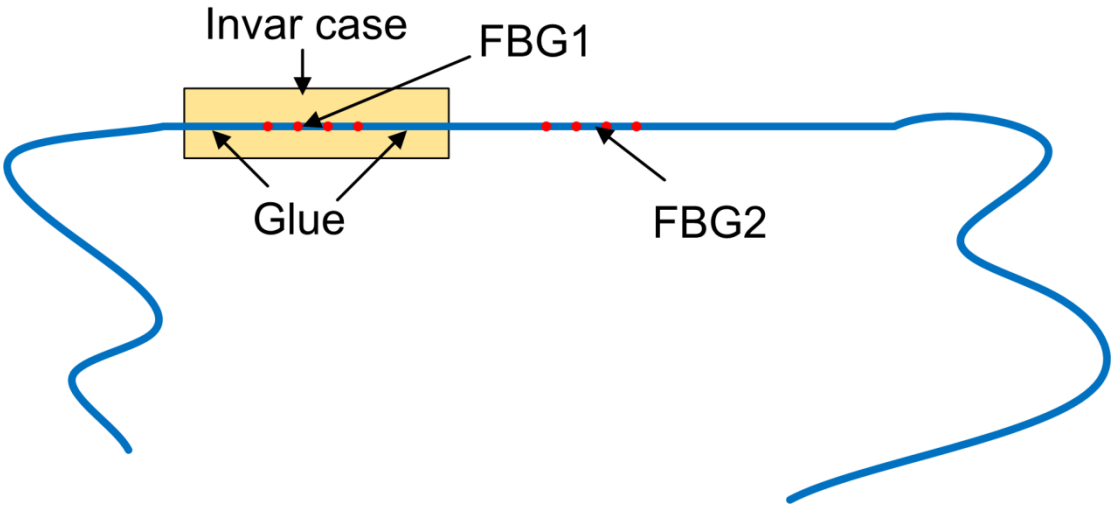

Figure 3.3. An implementation of a temperature invariant FBG. Two FBGs with different reflection peaks are spliced together, one is bonded at both ends to a piece of invar and the other is left free. Both FBGs are susceptible to temperature changes but only FBG2 has strain exerted on it. By measuring the reflection peaks of both FBGs the strain on FBG2 can be extracted.

Another limitation of FBGs is their one dimensionality, they only detect strain parallel to the core. This can also be solved with multiple FBGs in series, but other techniques also exist, for example inscribing a different period Bragg grating into each core of a multicore fibre, so the strain on each core can be measured - allowing bend direction to be calculated [72].

3.2. Side-polished fibre-like waveguide sensor

ULI has previously been used to make an evanescent field sensor [73]; in this case a selective chemical etching stage was utilised to create a channel, allowing the measurand to be brought into sufficiently close proximity to the waveguide core for detection. Since surface ablation thresholds are generally lower than the bulk material modification threshold for waveguide fabrication, the direct inscription of waveguides sufficiently close to the substrate surface for sensing applications requires special considerations in terms of the processing parameters.

3.2.1. Fabrication

Fused silica was selected as the substrate material for its compatibility with a large range of thin film deposition and other functionalisation techniques. To allow waveguide fabrication close to the surface, the multiscan technique was used to lower

fabrication pulse energy for a given index change. A comparatively high NA focussing objective was also used to decrease the confocal parameter. Straight waveguides were fabricated for a range of pulse energies and translation speeds 75 µm below the substrate surface using the IMRA® system described in Chapter 2. The repetition rate was set to 500 kHz and the pulse duration was measured to be 450 fs. The laser polarisation was adjusted to be circular and focussing was performed by a 0.67 NA single element aspheric lens. Waveguides were built up from 15 elements with a 0.2 µm separation between each element. An element consisted of both an out and a back scan at the translation speed. Under these conditions a local minimum in the insertion loss to an SMF-28 transmission line at 1550 nm was found for an incident pulse energy of 0.38 µJ and a translation speed of 4.0 $mm \cdot s^{-1}$. A measurement of the mode field diameter (MFD) of this waveguide yielded 7.8 µm in the horizontal axis and 8.0 µm in the vertical axis, slightly less than the MFD of SMF-28 = 10.4 µm. This implies that a smaller macroscopic bend radius can be achieved with this waveguide than with SMF-28 for a given bend loss. Based on this a bend radius of 30.0 mm was selected, since the expected loss for this radius of bend is negligible (<0.0005dB/turn) [74].

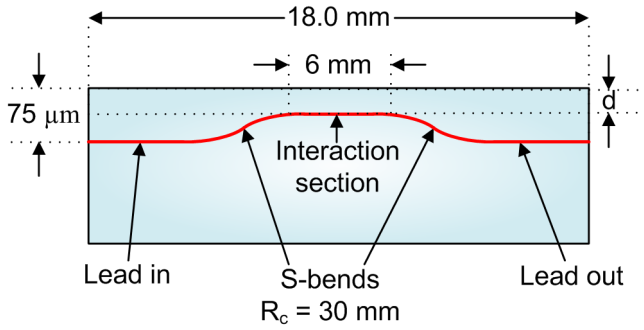

Figure 3.4. Schematic of the side-polished fibre-like ULI waveguide. R_c is the radius of curvature and d is the distance from the substrate surface to the centre of the waveguide in the interaction section.

The device design was based on a side-polished fibre and was made up of 5 distinct sections along its length: a straight lead in section parallel to the substrate surface; an s-bend to approach the substrate surface; a straight interaction section parallel to the substrate surface; a second s-bend away from the surface and a straight lead out, see Figure 3.4. Thirty waveguides were fabricated, each separated by 100 µm from the previous one. Each waveguide started and terminated 75 µm below the substrate

surface, but the distance between the centre of the waveguide in the interaction section and the substrate surface was varied. The depth of the interaction section was 30 µm for the first waveguide (waveguide 1) and was decreased by 1.45 µm per waveguide for each subsequent waveguide. Inspection of the substrate, post fabrication, under an optical microscope showed that waveguides 1-18 had no signs of surface ablation, waveguides 19-25 exhibited ablation in the central interaction region and waveguides 26-30 exhibited ablation in the s-bend sections and showed no signs of material modification in the interaction region. Waveguide 18, the waveguide with the smallest waveguide-to-surface parameter ('d' in Figure 3.4) and no signs of surface ablation was selected for characterization. This waveguide has a 'd' parameter of 6.0 ± 1.0 µm. Before characterisation the sample was ground and polished to expose the waveguide facets.

3.2.2. **Characterisation**

The output facet of the waveguide was imaged with a calibrated NIR camera while coupling the light from a fibre coupled 1550 nm distributed feed back (DFB) laser diode into the other end of the waveguide. This confirmed the MFD of the guided mode to be the same as in the earlier study of straight waveguides, see Figure 3.5.

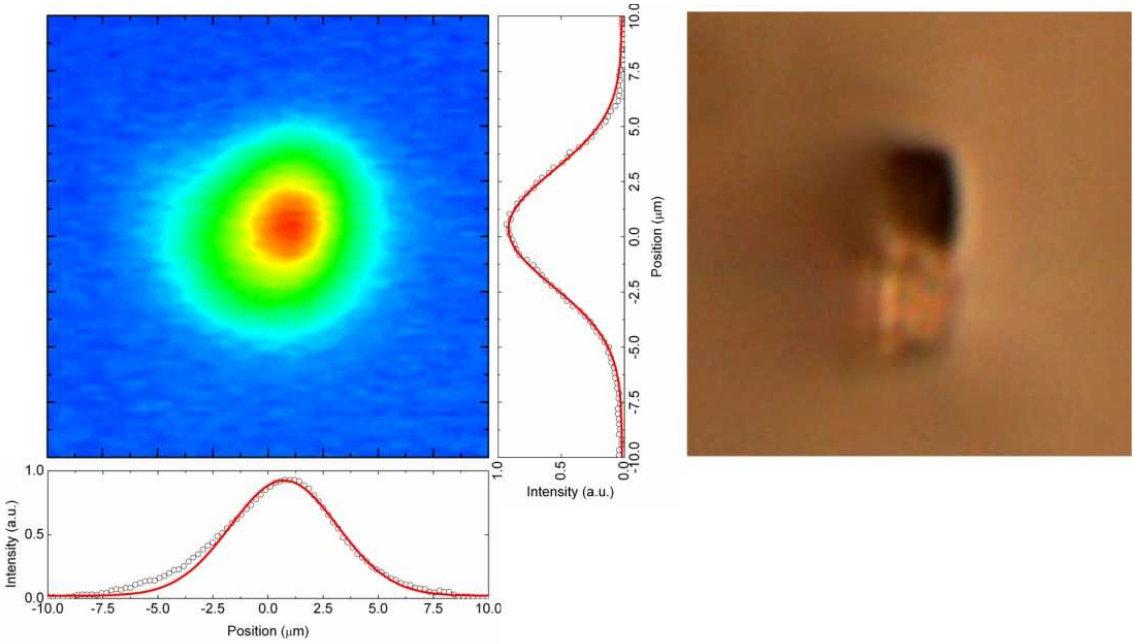

Figure 3.5. Left: false colour near field image of the 1550 nm guided mode. The intensity cross section is shown in dots with a Gaussian fit shown with a red line. Right: near field white light transmission micrograph of the waveguide facet. The field of view for both images is 20x20 µm.

The waveguide insertion loss (IL), coupling loss (CL) and propagation loss were obtained in the following manner, as shown in Figure 3.6. The light from the DFB laser was coupled via a polarisation controller into a short length of SMF-28, which was spliced to a piece of high NA, large core, multimode fibre and connected to a calibrated power meter. The reading from the power meter was taken as our reference. The SMF-28 fibre was then broken, cleaved and butt coupled to the waveguide, with index matching gel used to decrease losses due to Fresnel reflections. The difference between this and the reference is defined as the waveguide IL. Next the multimode fibre was broken, cleaved and butt coupled to the waveguide. This allows the CL to be measured, assuming that the multimode fibre collects all the light emerging as a result of it being of a higher numerical aperture and a greater core size.

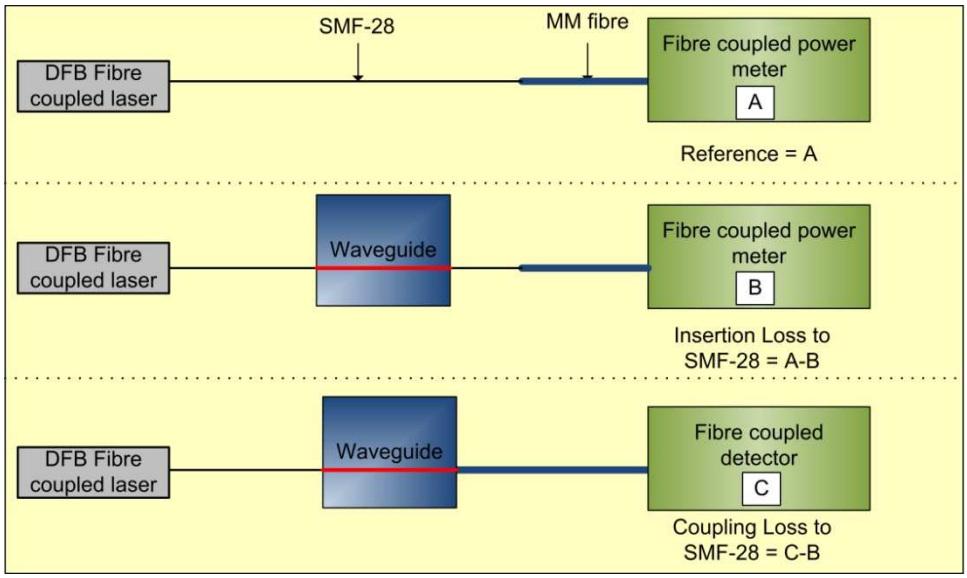

Figure 3.6. Schematic of the device test procedure for passive characterisation. The power emerging from the fibre is taken as a reference (A). By inserting the waveguide into the section of SMF-28 and measuring the power, an insertion loss is calculated (A-B). The coupling loss can be measured by assuming that since the multimode fibre is of a greater core size and numerical aperture, it will catch all light emerging from the SMF-28 or from the waveguide. Therefore the coupling loss to multimode fibre due to mode mismatch is zero so the coupling loss per facet can be calculated (C-B).

The IL of the waveguide was measured to be 2.6 dB with a polarisation dependent loss (PDL) of 0.3 dB. The PDL was measured using the "all states method" - measuring the insertion loss of the device as the polarisation controller is scanned through all of the

possible polarisation states. The CL was measured to be 0.4 dB/facet, agreeing with the 0.4 dB/facet predicted by a Gaussian mode overlap integral between the mode of the waveguide and the mode of SMF-28 fibre. Based on this CL we can infer a propagation loss of 1.8 dB for the device, including any losses due to increased scattering from the section close to the substrate surface.

3.2.3. **Changes to the external medium**

The suitability of the waveguide for sensing changes to the external medium was tested by placing a high index oil (Cargile refractive index liquid series A, n_D=1.64), with a refractive index of 1.608 at 1550 nm [75], on the substrate surface over the interaction section of the waveguide. With air in contact with the substrate surface the device supports a guided mode with an evanescent field extending beyond the substrate surface. Since the oil is of a higher index than the waveguide core, when a thick layer of oil is placed on the surface the waveguide no longer supports a guided mode. Light input into one end of the waveguide can tunnel through the low index cladding into the oil and the waveguide mode can be defined as a leaky mode. This mode has an attenuation coefficient dependent on the waveguide properties, the distance the light must tunnel and the index of the oil [76], see Figure 3.7.

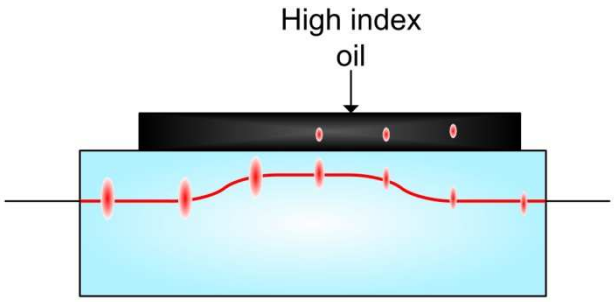

Figure 3.7. Device operation: in the presence of a high index layer the waveguide mode become leaky.

With the oil in uniform contact with the substrate surface, the device exhibited an increase in PDL of 1.0 dB and a polarisation averaged increase in IL of 3.7 dB. To test the temporal response of the sensor the polarisation controller was stopped from scanning - leaving a constant, arbitrary polarisation state input into the waveguide - and the output fibre was connected to a large area photo diode. The diode was connected to

an oscilloscope to monitor the voltage, Figure 3.8 shows the experimental configuration.

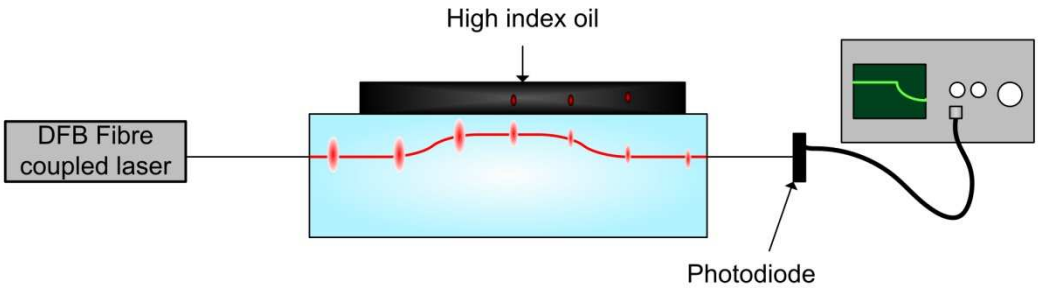

Figure 3.8. Experimental configuration for temporal studies of the waveguide sensor.

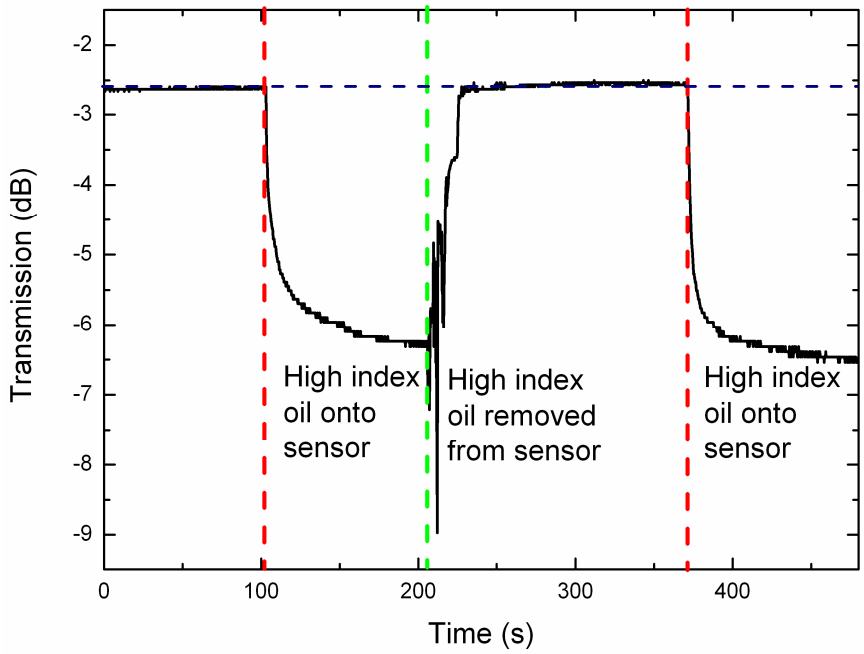

Figure 3.9. Sensor response as a function of time as the high index oil is introduced to the substrate surface, cleaned off with acetone and reintroduced for a constant arbitrary polarisation.

Figure 3.9 shows the recorded photodiode voltage as oil is introduced to the substrate surface, cleaned off with acetone and reintroduced. As the oil is introduced an immediate decrease in transmission is observed, the oil droplet then spreads out to cover the interaction section over ≈ 10 seconds. After this a slow decrease in transmission is observed, which is probably thermal in nature due to cooling of the high volatility oil. When the oil is removed with acetone and a cotton bud the transmission is fully

restored, showing a fully reversible change. These results were published in IEEE Sensors Journal [77].

A strong interaction has been demonstrated between the waveguide mode and the species on the substrate surface. This implies the suitability of this fabrication technique to evanescent field sensors and sensing networks. Another potential application is for the interaction of the guided mode with single walled carbon nanotubes to make saturable absorbers for modelocking lasers [78]. Work towards this is reported in Chapter 7.

3.3. Waveguide Bragg grating array

Previous ULI Bragg grating waveguides have been fabricated from single scan waveguides for both high and low repetition rate inscription lasers. This was done by selecting a translation speed such that single laser pulses are offset sufficiently to produce a longitudinal refractive index modulation for low repetition rate lasers (~1 kHz) [79, 80], or by external modulation of the inscription laser for high repetition rate inscription lasers (~1 MHz) [81]. The sensor described in this section features three waveguide Bragg gratings arranged in a triangular orientation to enable bend sensing through differential strain measurement.

3.3.1. **Flat fibre**

This work was undertaken in an experimental substrate obtained from the Optoelectronics Research Centre (ORC) at the University of Southampton. The substrate used is a ‘flat fibre’, which is an attempt to apply the mass production technology of fibres to the production of substrates for UV laser writing of planar lightwave circuits. More complete information on the planar fibre fabrication process is given by Webb *et al.* in [82], and details of one application is given by Holmes *et al.* in [83]. Briefly, however, a hollow preform is fabricated by the modified chemical vapour deposition (MCVD) of a heavily germanium doped silica layer inside a fused silica capillary. This leaves a hollow cylindrical tube featuring a germanium rich photosensitive high index layer surrounded by pure fused silica. By applying a vacuum during the drawing process the hollow tube can be collapsed into a planar structure, featuring a germanium rich core and silica cladding. Fabrication parameters from the previous sensor device, known to work in fused silica, were tested and found to produce

acceptable waveguides in the cladding of this flat fibre. Due to the nature of the cross section of the fibre, see Figure 3.10, identical waveguides could not be inscribed with the same parameters for all positions across the fibre. When writing directly over the curved sections, the cylindrical aberrations to the beam from the fibre were sufficient to lower the irradiance in the focal volume to below threshold, see Figure 3.10. From these studies a window of 500 μm around the centre was established where a fixed set of inscription parameters produced very similar waveguides.

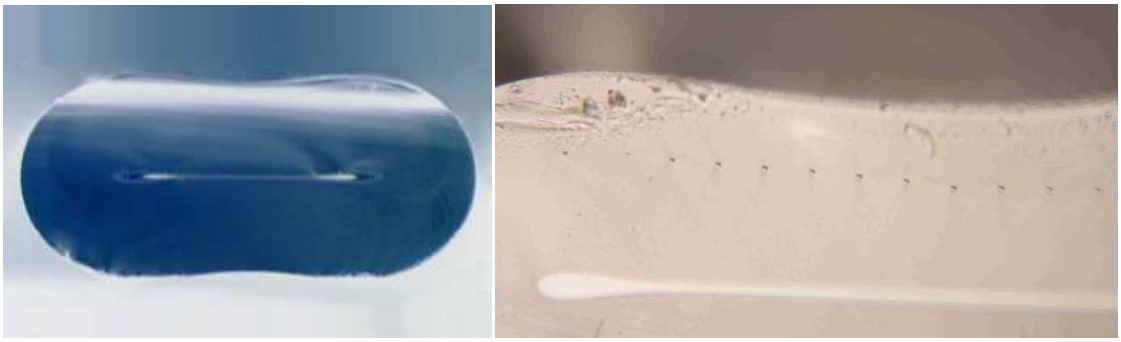

Figure 3.10. Left: flat fibre cross section, note the curvature. Right: waveguides written in the cladding region of the fibre.

3.3.2. **Multiscan ULI Bragg gratings**

Writing Bragg gratings using the multiscan technique poses several difficulties not encountered in other aspects of ULI. As with the rest of the waveguide, the grating section is built up of multiple scans, however each scan in the grating region contains a longitudinal index variation. A first order Bragg grating in fused silica designed to reflect 1550 nm light has a period of approximately 500 nm. For the grating to reflect, it is necessary to carefully control the phase of the index modulation of each scan, as any misalignment will result in a reduction in the reflectivity of the grating. From this it is clear that the position tolerance of the substrate relative to the laser focus is substantially less than 500 nm throughout all of the scans required for the waveguide inscription. For this reason the extremely low latency position sensitive output (PSO) of the Aerotech stages was used to trigger the acousto-optic modulator (AOM) used to modulate the inscription laser, this procedure is described by Brown *et al.* in [84]. The AOM was placed within a symmetric telescope, to reduce the beam size within the AOM, and to keep the effective NA of the objective the same as for the previous work. Since the amount of flat fibre was limited, device design and trouble shooting were carried out in

planar fused silica substrates, similar to those used for the side-polished fibre-like sensor described earlier.

The Aerotech control software makes provision for virtual I/O register commands within the software, which can be used to trigger events outside the Aerotech software itself. Two of these are routinely used within our systems to pass the value of a variable to a Labview program used to control the waveplates for power and polarisation control of the inscription laser. Another command within the software was defined to pass the required modulation frequency for the AOM to the signal generator used to modulate the AOM driver. The AOM was aligned in a zero order configuration, such that when the AOM was inactive the laser light reached the lens to be focused inside the sample and when the AOM was active only ~20 % of the light remained in the zero order to be focused inside the sample. An iris was aligned after the AOM to allow the zero order to pass but block all higher orders. The AOM driver was set to trigger from the PSO of the Aerotech stage driver, defining a spatial window along one of the position axes for which the AOM would fire continuously at the defined frequency. Multiple waveguides were inscribed with Bragg waveguide sections within them, to confirm that passing of the modulation frequency was occurring between the Aerotech software and the signal generator. Once this was verified within the silica test samples, Bragg grating waveguides were inscribed within the flat fibre to confirm fabrication conditions.

3.3.3. **Y-Splitters**

To allow multiple Bragg gratings within separate waveguides to be interrogated, a method of splitting and recombining light from a single source was required. 3x3 symmetric directional couplers have previously been demonstrated by ULI [85], but require careful control of inscription parameters and significant optimisation to achieve usable results. A far simpler, but less elegant, method is to use a Y-splitter [86]. Here the coupling between waveguides depends not on coupling of the evanescent field of the guided mode from one waveguide core to another, but upon the mode overlap between the waveguides at the splitting point, see Figure 3.11. A simple in-plane 3x3 Y-splitter was fabricated in fused silica. While energy transfer was not symmetric, sufficient energy was launched into each core to enable progression of the design to the next stage.

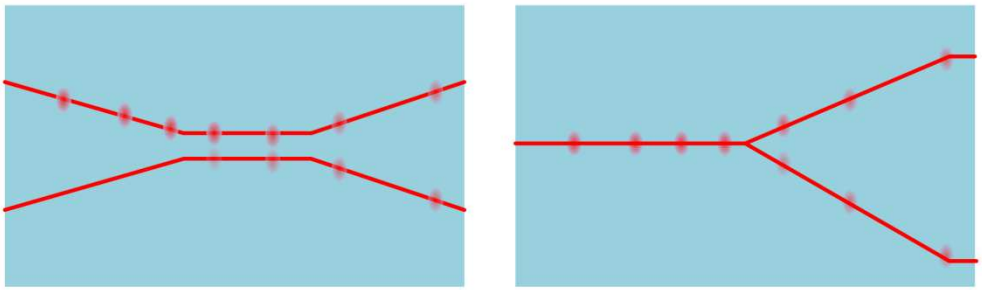

Figure 3.11. Left: a directional coupler. Within the interaction section energy passes from the guided mode of one waveguide to the guided mode of the other waveguide. If both waveguides have the same propagation constant, then complete energy transfer can occur, if the length of interaction section is correct. Right: a Y-splitter. Energy transfer occurs at an abrupt point and is based on the mode overlap between the input waveguide and each of the two output waveguides.

3.3.4. **Fabrication**

The intended device design aimed to mimic the Bragg gratings inscribed within multicore fibre [72]. The planar fibre would feature an in-plane 3x3 Y-splitter, a fan-out section to move the 3 waveguide cores out of a plane and 3 straight, parallel, waveguide sections, each featuring a Bragg grating. The three Bragg gratings would be designed to have different periods, so as to reflect different wavelengths. A device design schematic is presented in Figure 3.12.

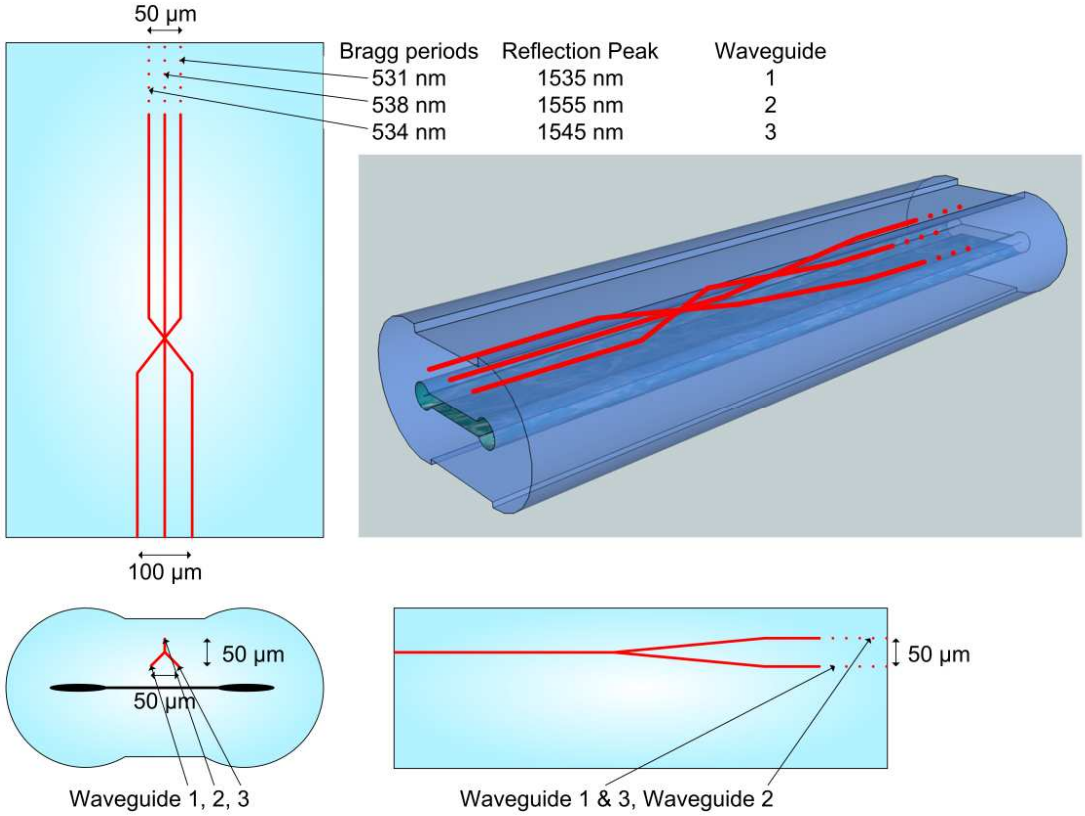

Figure 3.12 Schematic of the Device. An in-plane 3x3 Y-splitter followed by a fan-out section to move the waveguides out-of-plane, each waveguide contains a Bragg grating section of a different period.

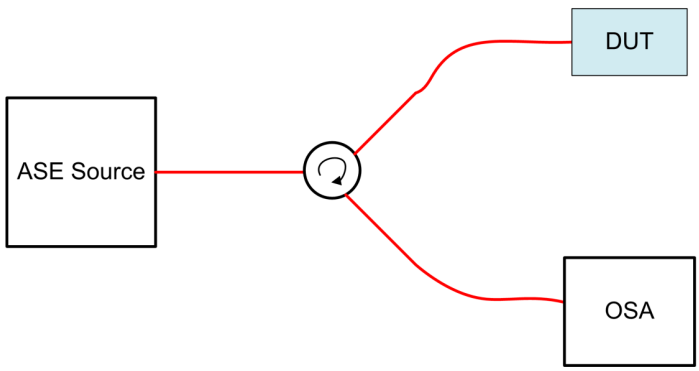

Figure 3.13 Schematic of the device being tested. The device under test (DUT) is interrogated by an erbium doped fibre amplified spontaneous emission source (ASE) via a circulator (Arrow). The spectrally resolved reflection from the device is measured on an optical spectrum analyser (OSA)

The complete device was fabricated in a piece of fused silica and interrogated, via a fibre circulator, by an erbium doped fibre amplified spontaneous emission (ASE) source. The third port of the circulator was connected to an optical spectrum analyser (OSA), see Figure 3.13. The three reflection peaks from the waveguides could be clearly resolved when coupling into any of the three input cores, so the device was replicated within a piece of flat fibre. A fibre v-groove was fabricated by irradiating undesired regions of a piece of fused silica and chemically etching in 4% HF aqueous to leave a 5x5x1 mm fused silica cuboid, with a two stage v-groove in the top. The first 2 mm long section made a tangent to a 125 µm circle (SMF-28 cladding diameter) and the 3 mm long section made a tangent to a 250 µm circle (SMF-28 buffer diameter). A partially stripped fibre section was placed in the v-groove, had optical adhesive (Norland Optical Adhesive 61) applied and a flat piece of fused silica placed over the fibre to sandwich it in place. The v-groove was clamped and exposed to light from a UV lamp for 5 minutes. The fibre was then cleaved and the fibre v-groove was polished at an angle of ~8º. The flat fibre was hand polished to an angle of ~8º and the fibre in the v-groove was aligned to each of the 3 cores in turn, while viewing the strength of the reflection peaks. The strongest peaks were visible for alignment into the central core, so the fibre v-groove was bonded to the flat fibre in this position using optical adhesive. Unfortunately some misalignment of the fibre to the waveguide occurred during the bonding process, lowering the reflectivity of the reflection peaks by ~ 4 dB, also, during this process the reflection outside of the reflection band of the gratings increased significantly. Since there was no simple method for realignment, the device characterisation was carried out under these unfavourable conditions.

3.3.5. **Device characterisation**

For temperature characterisation of the device, it was placed next to a thermocouple in an oven and the oven was heated to 80 ºC. The heating element of the oven was then switched off and a reading of the wavelength corresponding to the reflection peak for each grating, was taken for every degree drop in temperature, see Figure 3.15. A linear relationship is clearly visible, with the core in close proximity to the heavily dope central region (grating 2) of the fibre having a slightly higher gradient than the other two gratings. The three cores displayed temperature sensitivities of 10.5, 12.2 and 10.1 pm/ ºC respectively. The full width at half maximum (FWHM) of the 3 peaks are ~250 pm.

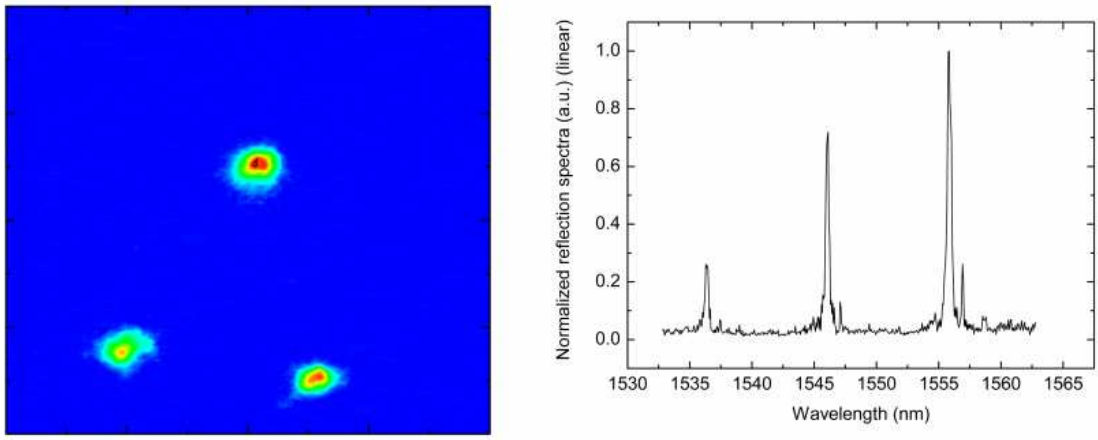

Figure 3.14, Device characteristics. Left: a false colour near field image of the flat fibre end facet when coupling into the central input waveguide. Right: the spectra measured by the OSA for coupling into the central waveguide.

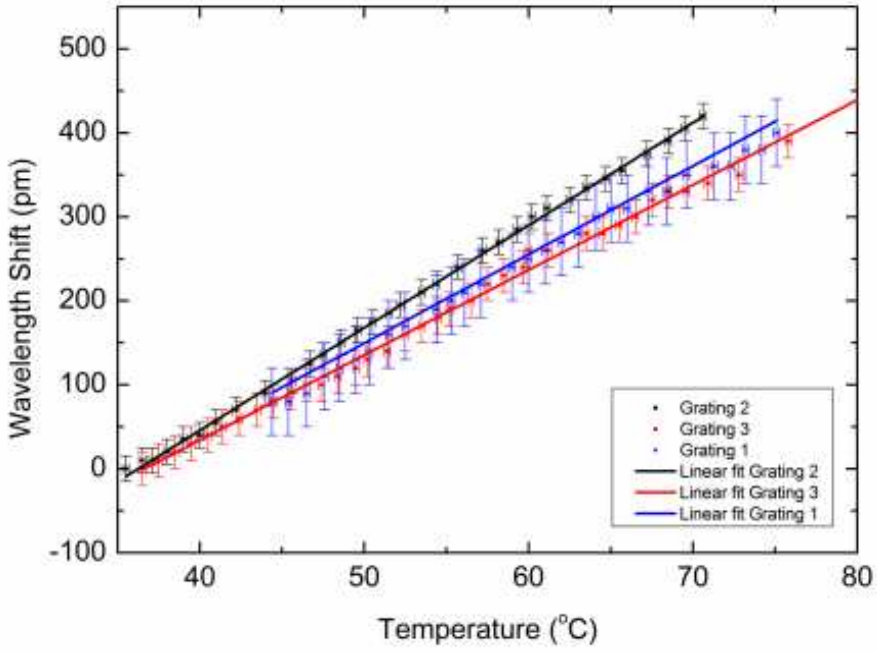

Figure 3.15, Device characteristics. the shift in reflection peak wavelength for changes in temperature for the three Bragg grating waveguides and linear fits to the data.

3.3.6. **Strain characterisation**

For the strain testing a sample holder and actuator were designed with the help of the Physics mechanical workshop staff at Heriot-Watt University. The holder was required to keep the bonded region and coupling section unstrained, but allow strain to be placed on the flat fibre section containing the Bragg gratings. The final design selected is shown in Figure 3.16. A metal rod is bonded to the device, the rod is supported at one

end by a metal block while the other end is left free to allow actuation. If one makes the assumption that the glass is thin and malleable, then the metal rod will bend uniformly along its free standing length see Figure 3.17. This is an oversimplification of the problem, but will provide an estimate of the radius of curvature of the flat fibre for each deflection of the metal rod. If we also assume that the device is aligned perfectly on axis to the rod in the horizontal plane, the strain in each core for any given deflection in the horizontal plane can be calculated using basic geometry. These estimates of the strain in each core are shown as the solid lines in the left panel of Figure 3.18. A similar assumption could be made for deflection in the vertical axis but requires knowledge of the distance between the centre of the rod and the position of the waveguides, the nature of the bonding process prevents this.

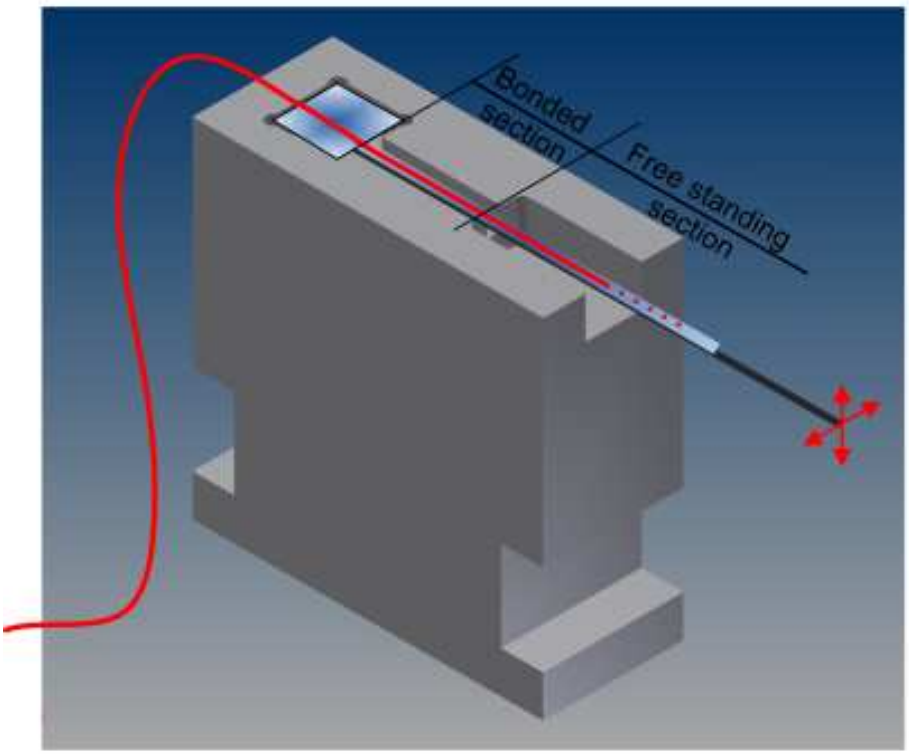

Figure 3.16. Device holder design. A metal block provides a pivot for a metal rod, the rod is bonded to the sensor.

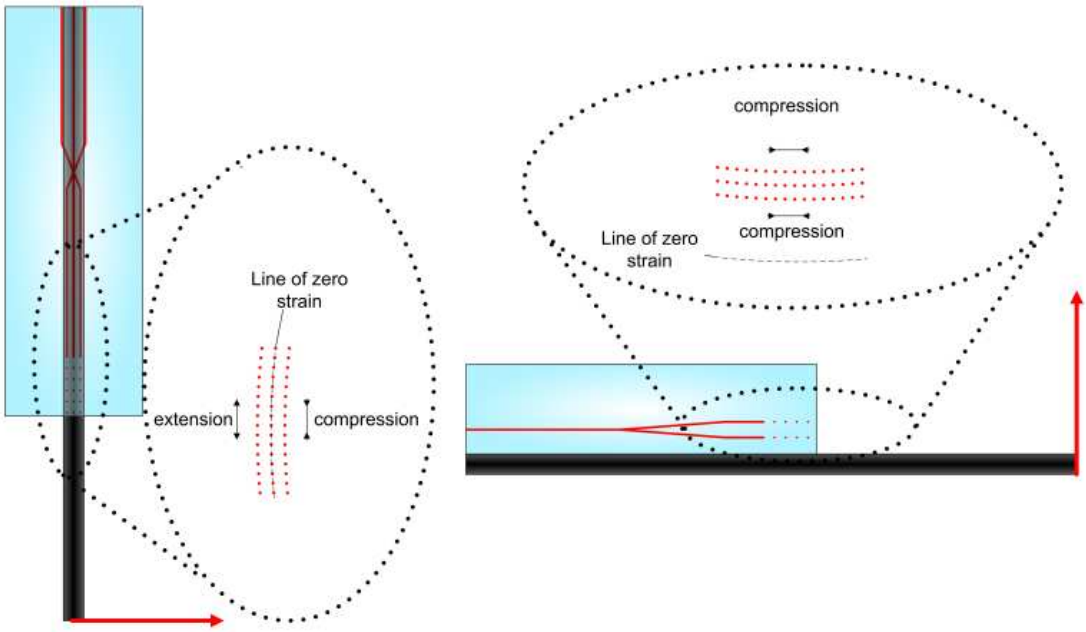

Figure 3.17. By actuating the rod, strain is placed upon the device, through measuring the difference in the shifts in the reflection peaks the strain and strain direction can be measured.

After assembly of the holder and device, the end of the rod was deflected by a manual micro translation stage. For each deflection, the reflection peak of each of the gratings was measured. By recording the reflection peaks for a range of deflections, the device can be analysed.

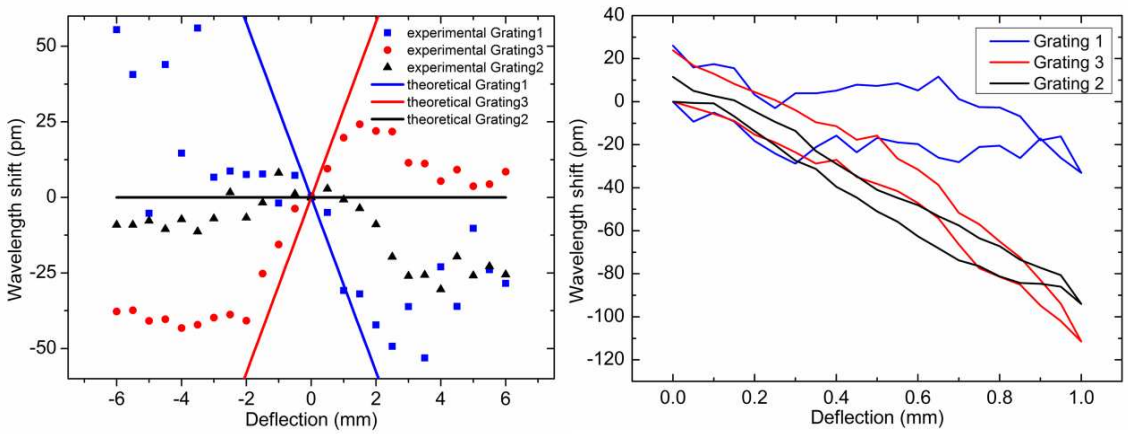

Figure 3.18 Wavelength shift with deflection for- Left: the horizontal plane and Right: the vertical plane.

As Figure 3.18 shows, for the horizontal plane some agreement with theory is visible for small deflections. As the deflection increases some relaxation of the device occurs,

causing a plateau in the wavelength shift. This is likely to be due to the adhesive between the device and the metal rod and could possibly be remedied through better bonding. It is also likely that as the rod is actuated some twisting of the rod also occurs due to the glass above it, this is not accounted for by the simplified model. For the vertical direction significant distortion to the peak shape of grating one occurs, this renders the results inconclusive. The hysteresis loops visible in the reflection peak position for vertical strains also imply problems with the adhesive used.

The device shows strong potential for future development, but in its current form is not ready for the intended application as a 2D strain sensor. Further optimisation of inscription parameters may stop distortions of the reflection peaks, but most crucially for improved results is better bonding between the flat fibre and the metal rod.

3.4. Conclusions

This chapter has presented details on the fabrication and characterisation of two sensors fabricated using ULI. The side-polished fibre-like sensing element shows significant potential for environmental sensing. Integration with Y-splitters, as used for the flat fibre strain sensor, could allow for single chip Mach-Zehnder interferometers to detect changes in the guided mode's effective index. Another method of detecting changes to the mode's effective index would be via the inscription of a Bragg grating section in the region close to the surface. The geometry of a single sensing element would allow for them to be spatially multiplexed, allowing 1 dimensionally spatially-resolved sensing within a single substrate. This spatial resolution is limited by the proximity of the waveguides before evanescent coupling between them starts to occur, this is of the order of 20 µm, a typical spacing for linear image sensors. One end of the array could feature cascaded Y-splitters for coupling from a single light source, and the other could be directly bonded to a linear image sensor, to allow spatially resolved absorption measurements, in an integrated device. The waveguide Bragg grating array shows potential for its intended application, but was limited in usability by the quality of the bond to the rod whose strain it was intended to measure. The flat fibre proved to be a suitable substrate for ULI and could be utilised for a variety of other applications. One possibility would be to write waveguides in the cladding region which are coupled to UV written waveguides within the core of the fibre. This would allow UV written waveguide circuits to probe the surface at selected positions. Ultimately the strength of ULI as a sensing technology is in the diversity of components that can be fabricated in a

single substrate, and in the ability to arrange them in three dimensions. The flat fibre work has provided a step towards this goal.

One attractive aspect of ULI is in the diversity of materials that can be processed. The next chapter investigates waveguides inscribed in the nonlinear crystal monoclinic bismuth borate for SHG. The index change responsible for the guiding occurs due to strain induced in the material and a novel approach is taken to increase the overlap between the orthogonally polarised modes which are required for birefringently phase matched SHG.

Chapter 4. Waveguides in monoclinic bismuth borate for nonlinear applications

4.1. Waveguides for nonlinear applications

Under certain conditions, a guided mode geometry has several benefits over free space propagation for nonlinear interactions. Perhaps the most notable example of this is photonic crystal fibre (PCF) [11], which allows significant spectral broadening of ~1 octave from relatively low pulse energies, due to its ability to control chromatic dispersion and preserve high irradiances over long distances. Another significant application of guided mode nonlinear optics is in SHG, which relies on the second order, or $\chi^{(2)}$, nonlinearity. For this reason SHG requires a noncentrosymmetric medium, normally requiring the long range order of a crystal with an appropriate lattice system, although some work on SHG has been done in periodically poled silica PCF [87], most waveguide SHG work has been performed in periodically poled lithium niobate (PPLN), with waveguides fabricated by annealed proton exchange [88], or with titanium or zinc indiffusion [89, 90]. Cutting techniques have also been used to remove material, increasing the waveguide index contrast [91].

The use of a waveguide allows the light to be confined to a high irradiance for interaction lengths longer than would normally be permitted with free space focussing. Waveguide SHG is of most use for CW sources, where the limited peak powers do not allow efficient SHG with conventional focussing and where the spectral bandwidth of the source is small enough to allow for the use of long crystals, see Section 2.2.2.

4.2. Monoclinic bismuth borate (BiBO)

Monoclinic bismuth borate has a large nonlinearity, is transparent throughout the visible and NIR and can be grown in large optical quality crystals [92]. Phase matching for $\chi^{(2)}$ and $\chi^{(3)}$ processes can be achieved through birefringent phase matching. The crystal used for this study was cut and polished for normal incidence along an internal propagation direction of $\theta = 168.8°$, $\phi=90°$. This internal propagation angle enables type I phase matching in the optical yz-plane for SHG for a pump wavelength near 1047 nm at room temperature. The linear optical properties for BiBO are well reported in the literature

[93], based on this data, Professor Derryck Reid (Ultrafast Optics Group) from Heriot-Watt University wrote a Matlab® program to model the efficiency of SHG for different pump wavelengths, at various internal propagation directions within the BiBO crystal, see Figure 4.1.

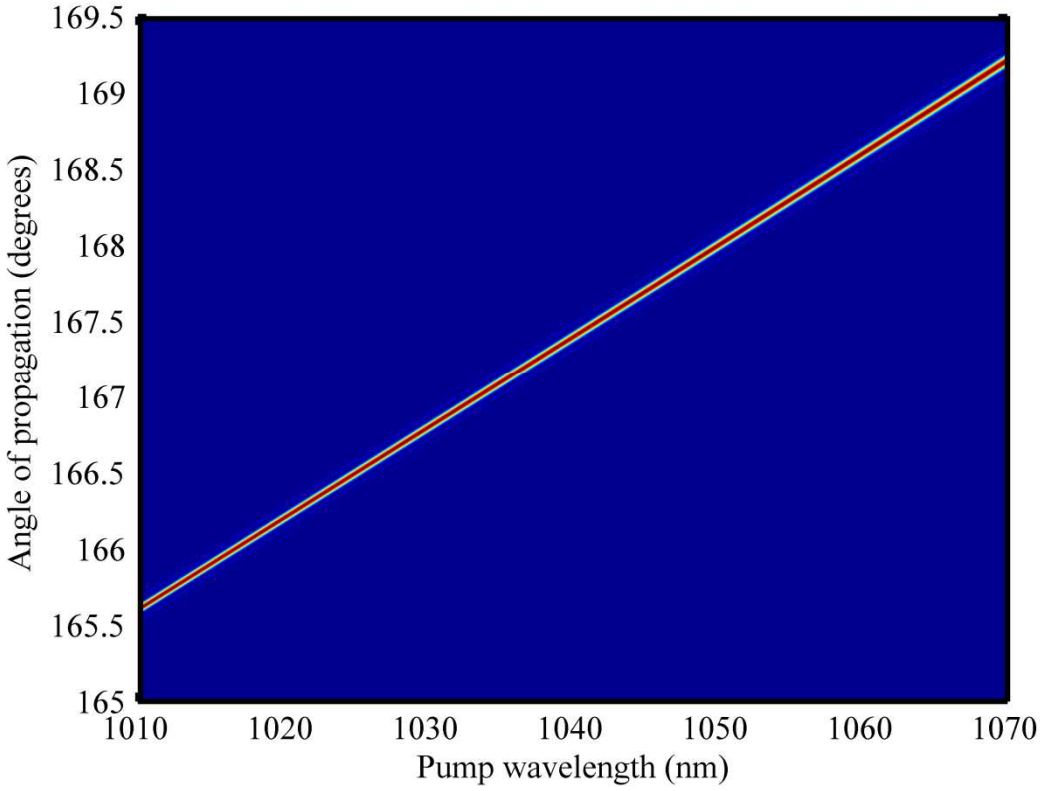

Figure 4.1 The predicted angle tuning of BiBO for type I SHG. The x-axis describes a fundamental wavelength and the y-axis an internal propagation direction. The false colour shows the normalised efficiency of the process, for a 10mm long crystal, (red shows the highest efficiency and blue the lowest).

4.3. Type II ULI waveguides

The waveguides described in this chapter are type II ULI waveguides, introduced in Section 2.9. Most type II waveguides feature two damage lines separated by 10 – 20 μm's. These structures aim to have a positive interaction between the strain fields generated by each of the damage lines, resulting in the region under most strain being between the two damage lines. This design can lead to a greater index change than can be achieved for a single damage line and so increase the modes separation from the regions of damage. It can also result in an almost symmetrical mode profile for the correct fabrication conditions. The position of the guiding region relative to the damage

lines is dependent on the substrate; different crystal structures behave differently and often the two orthogonal linear polarisations (OLP) are guided in spatially separated regions.

4.4. Pre-inscription measurements

The intention was to use the BiBO waveguide for the efficient frequency doubling of a home built, diode pumped, Yb:KYW laser, constructed by D. Reid. The laser could be operated in two configurations: modelocked by a semiconductor saturable absorbing mirror (SESAM); or wavelength tunable CW by the addition of a prism in front of the SESAM and an additional cavity end mirror. When modelocked the laser produced a spectrum of ~ 5 nm (FWHM) centred at about 1060 nm. A similar oscillator to this is presented in [94]. The laser was weakly focussed with a 10 cm focal length lens and the crystal was secured in an angle adjustment mount, placed at the focus of the laser. The crystal was angled and the optical power of the second harmonic was measured. For the angle corresponding to a maximum conversion, the reflection from the front facet of the crystal was traced back to level with the laser source. The external angle to the crystal for phase matching of the 1060 nm pumped SHG was then calculated. The crystal was removed from the angle mount and mounted onto the Aerotech translation stages, used to translate the substrate during waveguide inscription.

4.5. Two damage line structures

Waveguide inscription was carried out using the Fianium® laser inscription system, see 2.6.2. The laser was set to a repetition rate of 500 kHz and the pulse duration was measured at 350 fs pulses (FWHM). A 0.4 NA aspheric lens was used for focussing and the polarisation was set to be circular. An initial study of two line structures, with the two damage lines inscribed in the same direction on different passes of the crystal through the laser focus, was undertaken. Waveguides were inscribed for line separations of 10, 15 and 20 μm at pulse energies of 680, 560, 470, 390, 320, 270, 220 and180 nJ at a translation speed of 6 $mm \cdot s^{-1}$. Previous reports have shown some inscription direction dependence in low symmetry crystals [34], so all inscription parameters were repeated for both substrate translation directions.

After inscription the polarisation dependent guiding characteristics of the structures were investigated by imaging the output facet of the waveguide, through a linear polariser, onto a silicon CCD. The polarisation of the light entering the waveguide was varied with a polarisation controller, see Figure 4.2.

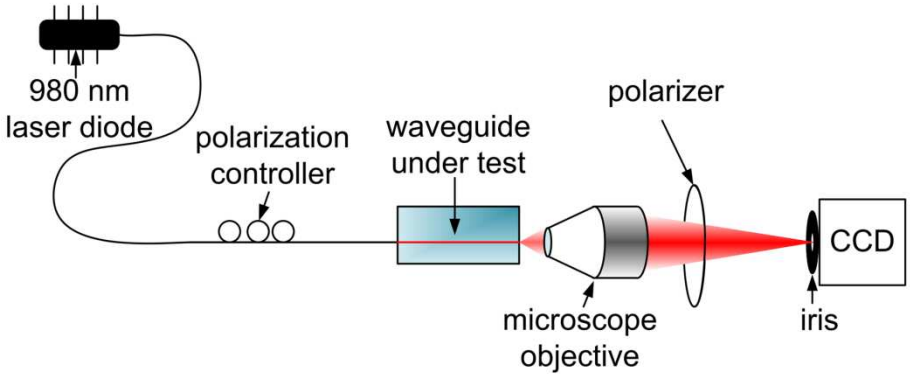

Figure 4.2. Experimental configuration for investigating the polarisation dependent guiding characteristics.

Images of the guided mode for the horizontal polarisation (H-pol), orthogonal to the inscription laser propagation direction, and vertical polarisation (V-pol), parallel to the inscription laser propagation direction, were captured. The fibre was then removed and the white light from a lamp was used to capture another image, allowing the positions of the guided modes relative to the damage lines to be established. For each waveguide there were several regions which exhibited guiding for either H-pol or V-pol light, but no region was found for any of the waveguides which supported both H-pol and V-pol modes. Figure 4.3 shows a superimposition of both the H-pol and V-pol modes over the white light illuminated image. This waveguide exhibited the best confined V-pol mode but the image is typical of all of the 48 waveguides inscribed and measured.

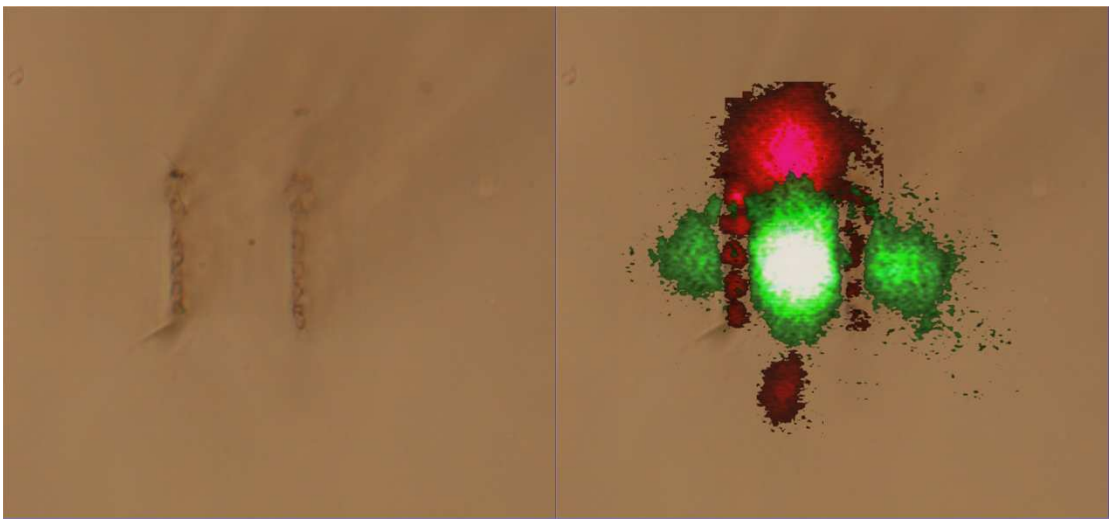

Figure 4.3. The polarisation dependent guiding characteristics for one of the two line structures. Left: a white light transmission micrograph of the waveguide facet. Right: the same micrograph but with the guided 980 nm modes superimposed on top. The H-pol mode is shown in green and the V-pol mode in red.

All the waveguides had an H-pol mode between the two damage lines and a V-pol mode above and between the two lines. Efficient birefringent phase matching requires a high degree of spatial overlap between the three fields, this could not be achieved using this type of waveguide. A new design of waveguide was proposed, it would feature two pairs of damage lines, vertically offset from one another. The aim of this four damage line structure was to attempt, through control of the vertical offset, to bring into alignment the H-pol mode from one pair of lines with the V-pol mode from the other pair of lines, see Figure 4.4.

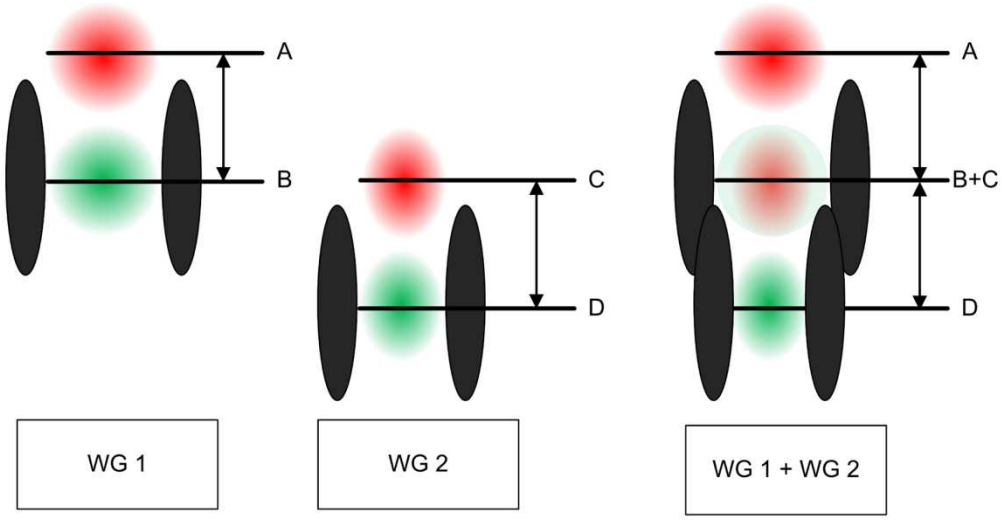

Figure 4.4. The proposed design for the four line structure. The H-pol mode (B) of waveguide 1 (WG1) is overlapped with the V-pol mode (C) of waveguide 2 (WG2) to achieve the guiding of both polarisations (B+C) (WG1+2)

4.6. Four damage line structures

Due to the large number of parameters for this new structure, the separation of the bottom two lines was fixed at 20 μm and the inscription pulse energy for all the damage lines was fixed at 680 nJ. The top pair of lines were inscribed with separations of 22.5, 25 and 27.5 μm, and the vertical offset between the bottom pair of lines and the top pair of lines was varied between 0 and 37.5 μm, in steps of 2.5 μm, for each of the three horizontal separations. By imaging the output of the waveguides in the same method as for the two line structures, the effect of the vertical separation between the two pairs of lines was investigated. Figure 4.5 presents the vertical separation between the OLP modes (B and C in Figure 4.4) for different vertical separations between the two pairs of damage lines. The solid line in this plot is the expected offset of the OLP modes if the two pairs of damage lines acted independently, based on the two line structure in Figure 4.3. The right pane of Figure 4.5 shows the waveguide with the best mode overlap between the H and V mode. It can be seen that the degree of spatial overlap for the four line structure is far higher than for the two line structure. The structure with the highest degree of overlap between the OLP modes was selected for nonlinear characterisation.

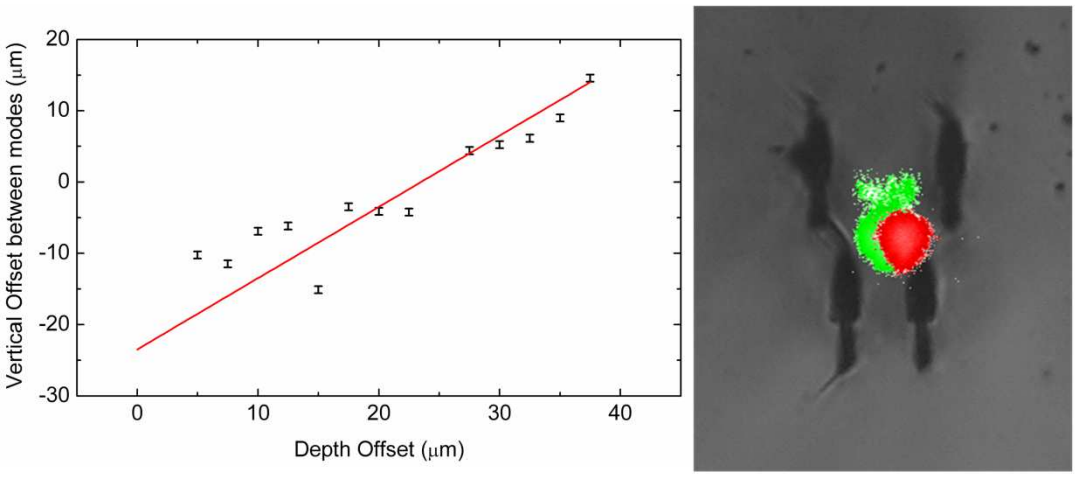

Figure 4.5. Left: the vertical offset of the modes as a function of depth offset between the pairs of damage lines. This is for upper lines with a 25 μm separation and lower lines with a 20 μm separation. The points show experimentally measured differences in mode position between the H-pol and V-pol modes. The line shows a prediction of the vertical mode offset assuming each damage line pair has no effect on the strain fields caused by the other pair of damage lines, based on the work in two lines structure (see Figure 4.3). Right: the H-pol and V-pol modes for the waveguide which exhibits the best vertical mode overlap between the H-pol and V-pol modes.

4.7. Nonlinear characterisation

An initial investigation was carried out by coupling the light from the Yb:KYW oscillator, operating in CW mode, into the waveguide using a 0.07 NA aspheric lens. Light was collected from the other side of the waveguide by a 0.25 NA lens. The light was then spectrally filtered with a Schott BG39 coloured glass filter to remove the fundamental wavelength and the power of the second harmonic was measured by a Newport 1930C power meter with a 918-UV detector head. The spectrum of the laser was tuned by angling the end mirror after the prism. The spectrum of the laser was captured using an OSA, the power of the laser was measured and then the power of the second harmonic emerging from the waveguide was measured. Wavelength tuning the laser in this manner was not ideal - as the laser was spectrally tuned both the spectral width of the laser and the average power of the laser changed substantially. Since the efficiency of the SHG is dependent on the square of the intensity, the second harmonic power was divided by the square of the fundamental power for plotting. This value is shown for each input wavelength in Figure 4.6.

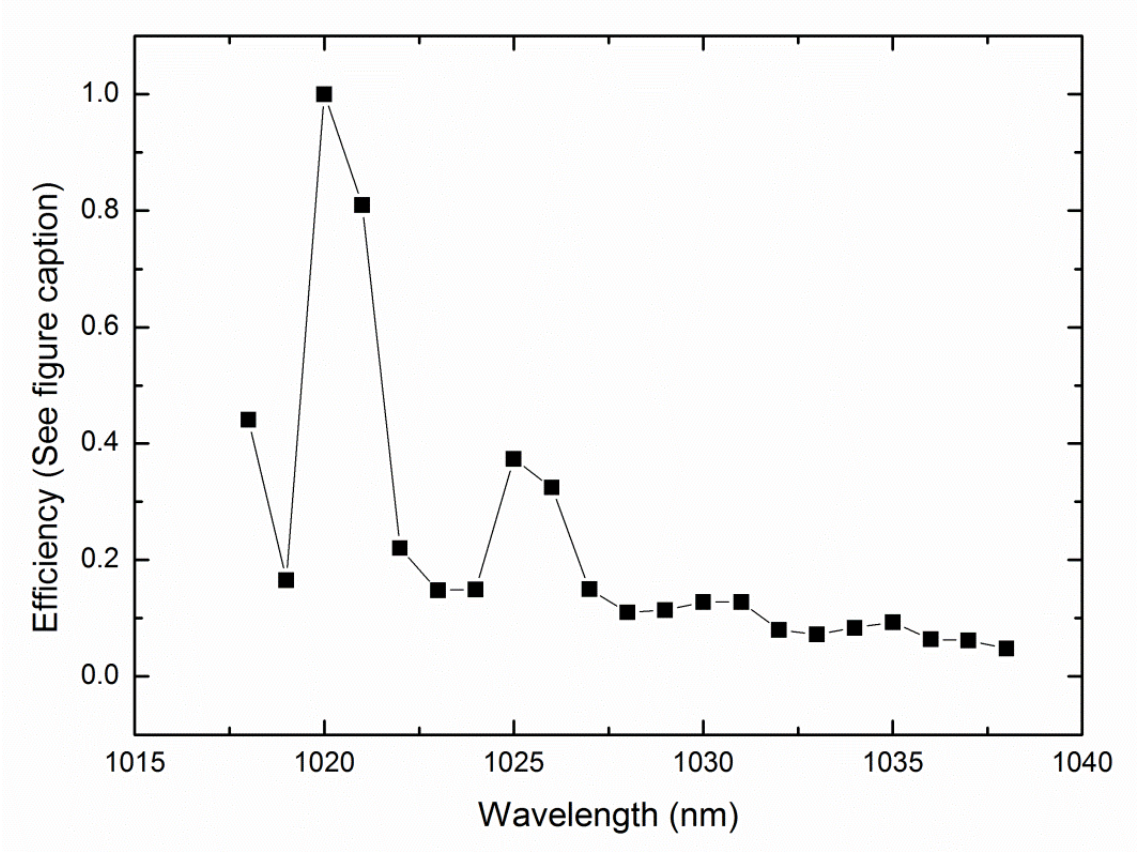

Figure 4.6. Wavelength tuning SHG in the BiBO waveguide. The efficiency plotted on the y-axis is the power of the SHG divided by the square of the fundamental power, these values are then normalised to the highest value.

In spite of the difficulty in finely tuning the laser, it was clear that something was not functioning as expected. The lasers power tailed off around 1018 nm, so tuning to shorter wavelengths was difficult and unstable, but from the pre-inscription measurements the maximum conversion efficiency was expected to be close to 1060 nm. It appeared that between the measurement of the optimum angle for the crystal, and the crystal being mounted on the stages for the first inscription run, the crystal had been inverted. Thus the waveguides were inscribed at a different angle from that desired and this pushed the phase matching to a shorter wavelength than for normal incidence, instead of to the longer wavelength than for normal incidence which was intended. This is in keeping with the model plotted on Figure 4.1, if the waveguides were inscribed close to 166° instead of the intended 169°. Normal incidence for the crystal was 167.8°, this is about half way in between the inscribed waveguide angle and the intended waveguide angle. 1020 nm is not a common laser wavelength, it can be emitted by a correctly designed Yb:fiber laser, but no sources were immediately available at this wavelength. Consequently, temperature tuning of the BiBO crystal was investigated

using the phase matching code written D. Reid, but adapted to include the thermo-optic coefficients for BiBO from [95]. The two available sources with the closest wavelengths to the required 1020 nm were a 980 nm fibre coupled laser diode and a 1047 nm CW Nd:YLF, diode pumped solid state laser. The result of temperature tuning the BiBO crystal for these pump wavelengths is shown in Figure 4.7-Figure 4.9.

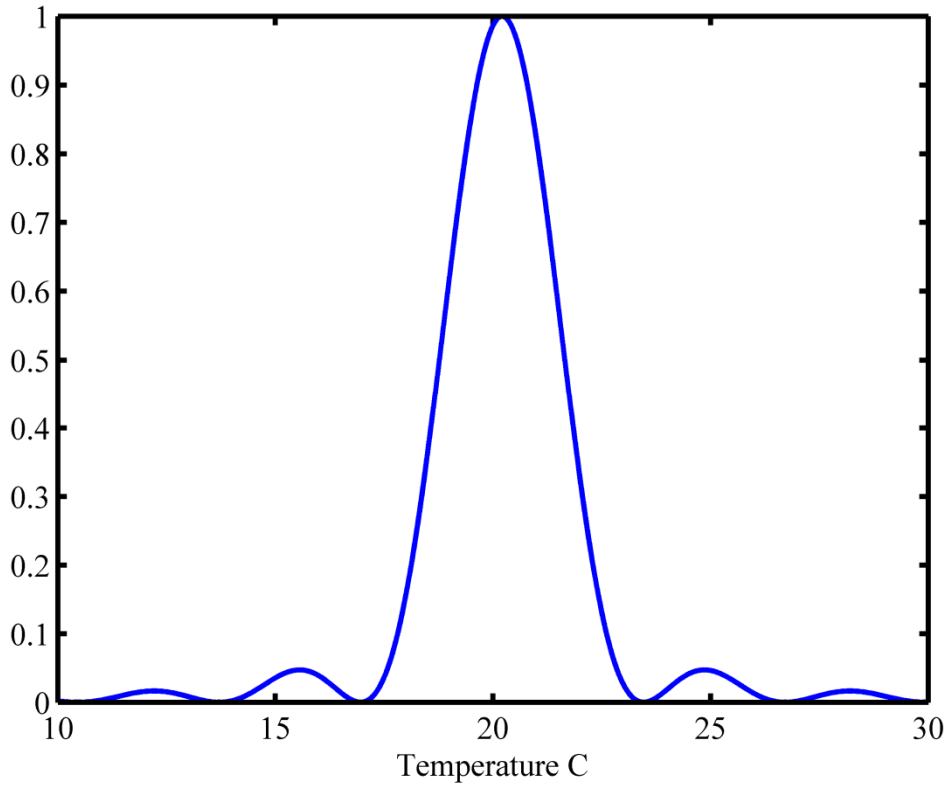

Figure 4.7. Modelling of temperature tuning for a fundamental wavelength of 1017 nm for an internal propagation direction of 166°.

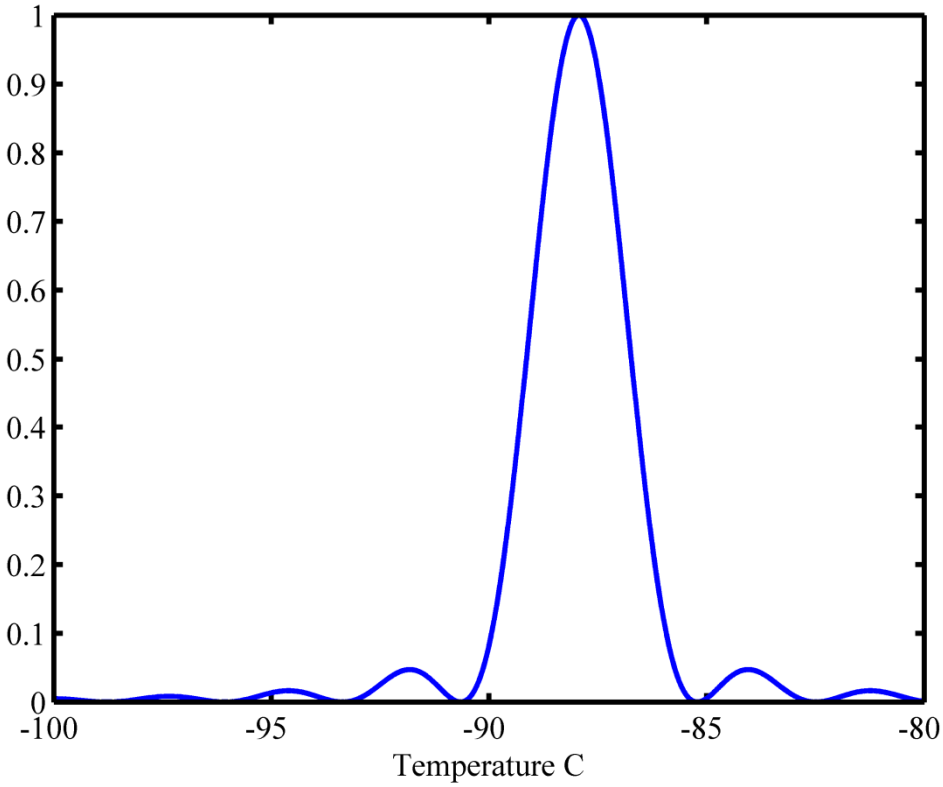

Figure 4.8. Modelling of temperature tuning for a fundamental wavelength of 980 nm for an internal propagation direction of 166°.

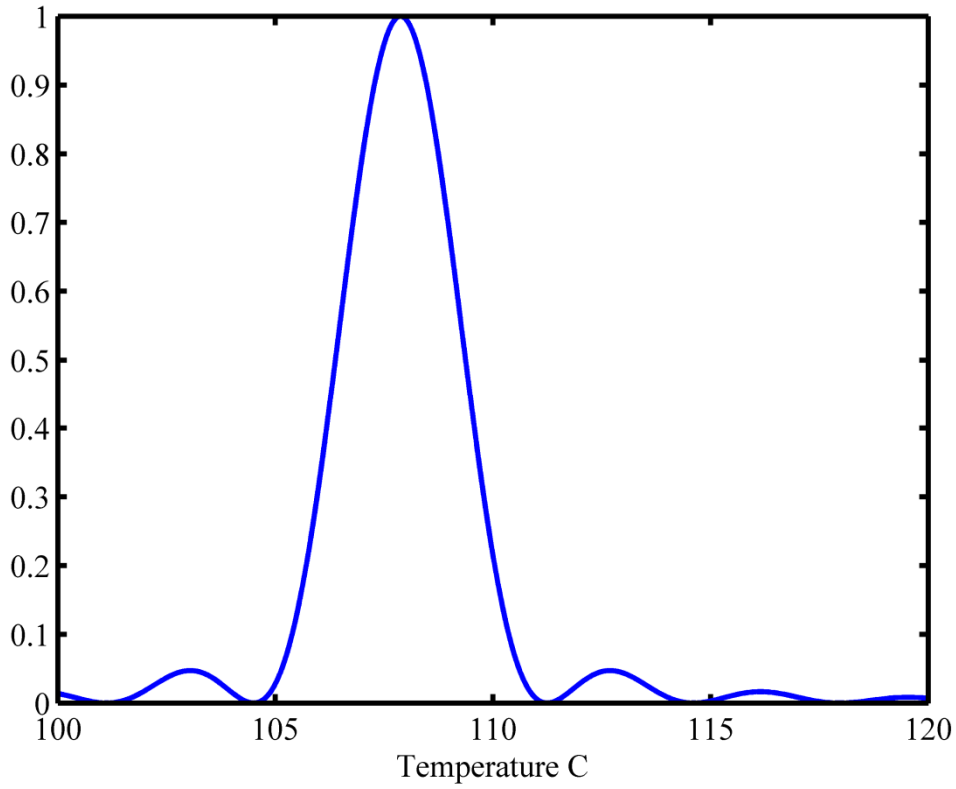

Figure 4.9. Modelling of temperature tuning for a fundamental wavelength of 1047 nm for an internal propagation direction of 166°.

Based on this analysis the crystal would need to be cooled to -88° for phase matched SHG with a pump wavelength of 980 nm, or heated to 109° for phase matched SHG using a pump wavelength of 1047 nm. It was deemed easier to heat the crystal than to cool it, so the 1047 nm pump source was selected. The crystal was mounted on a stack of microscope slides bonded together with super glue. This was stuck to the top of a micro-translation stage with nail varnish, the multiple microscope slides were intended to insulate the sample from the micro-translation stage, slowing down conductive cooling of the crystal. A metal piece with a gap for the crystal and a resistor screw fixed to the top (with thermal paste at the interface) was used as a heat source. A thermocouple was mounted in a hole in the metal piece, as close to the crystal as possible, for accurate temperature measurement. A cardboard box was placed over the waveguide, metal oven and micro-translation stage, to reduce air currents which may cause rapid temperature changes. The crystal was heated, and measurements of power of the second harmonic were taken. Figure 4.6 presents the results of temperature tuning the BiBO crystal for a 1047 nm pump wavelength.

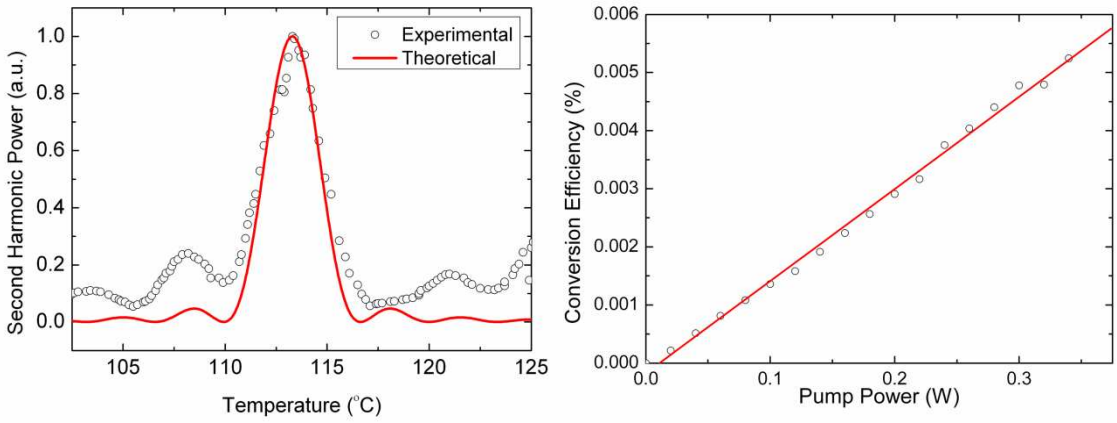

Figure 4.10. Temperature tuning the BiBO crystal for a pump wavelength of 1047 nm. Left: the experimental and theoretical phase matching curves for an internal propagation direction of 165.9°. Right: the conversion efficiency of the process.

Strong agreement can be seen between the theoretical and experimental phase matching curves for the temperature tuning, see Figure 4.10. Both theoretical and experimental data show a temperature acceptance bandwidth of ~ 3.3 °C (FWHM) for the 8 mm crystal. This shows that the crystal was indeed inverted between the pre-inscription measurements and the inscription of the waveguides. The SHG power measured shows the expected quadratic dependence on pump power (an efficiency is shown here, this is expected to increase linearly with power), but the efficiency is far lower than expected.

To understand this a propagation loss measurement for the waveguide was taken using the streak method [96]. For this measurement the top of the waveguide is imaged onto a calibrated CCD while light is coupled into the waveguide. By fitting an exponential decay to the 'streak' of light scattered out of the waveguide, the propagation loss of the waveguide can be measured. This measurement yielded a propagation loss of 5.0 dB/cm for the pump. The loss for the second harmonic was not measured, but is likely to be higher due to the shorter wavelength, leading to increased Rayleigh and Mie scattering, and the increased overlap of this polarisation mode with the regions of catastrophic optical damage, see Figure 4.5. This work has been published in Optics Letters [97].

The code used to plot Figure 2.1-Figure 2.3 was adapted to add a loss term to the coupled wave equations, to investigate the effect of a 4 dB propagation loss (for the 8mm sample length) on the efficiency of the process. The constants at the beginning of the coupled wave equations have been simplified into a single constant. This constant is back-calculated to give the observed conversion efficiency for 0.3 W of pump, a propagation loss for the pump of 4.0 dB and a propagation loss of 6.0 dB for the second harmonic. While this is not scientifically rigorous, it aids in understanding the role of the high propagation losses for nonlinear processes.

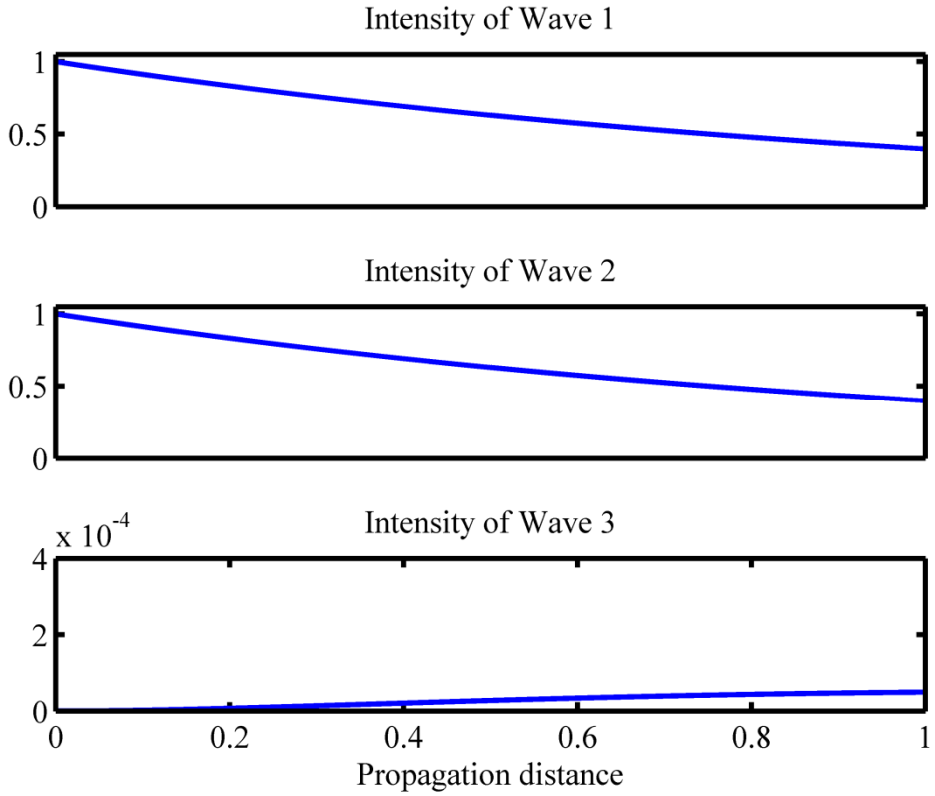

Figure 4.11. Conversion efficiency for a pump loss of 4.0 dB and a second harmonic loss of 6.0 dB, the gain term (ie d) has been fitted to the experimental data for 0.3W of pump.

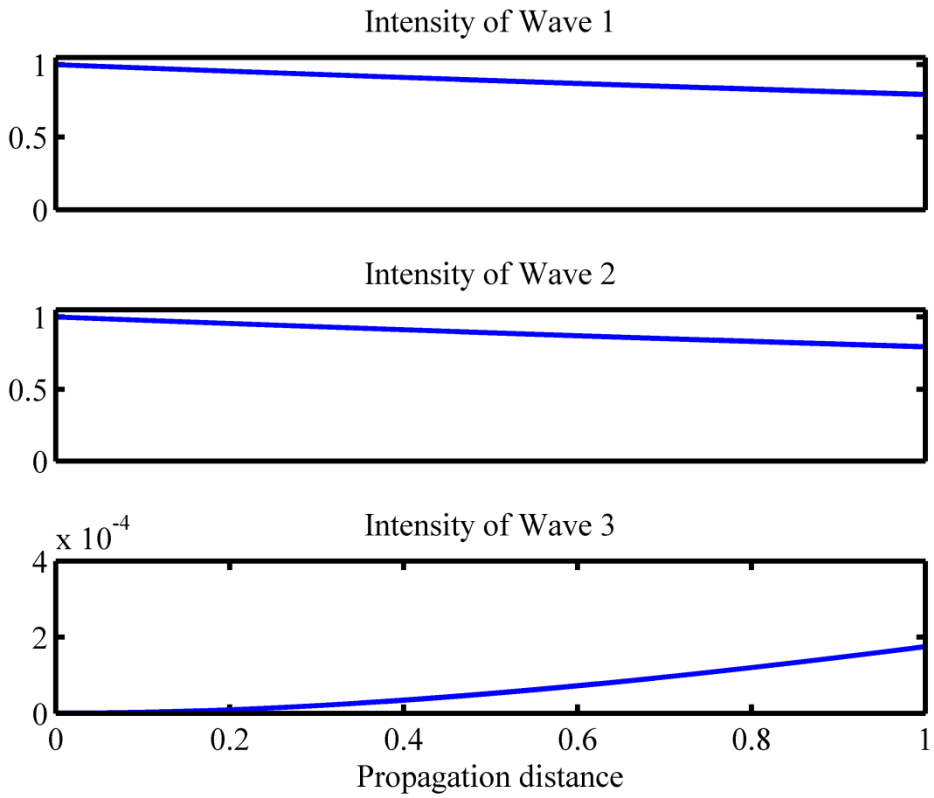

Figure 4.12. Conversion efficiency for a pump loss of 1.0 dB and a second harmonic loss of 1.0 dB, the gain term (ie d) is the same as for the earlier plots. These propagation losses are considered realistic for high quality type II ULI waveguides and typical for many waveguides fabricated by the Ti indiffusion technique.

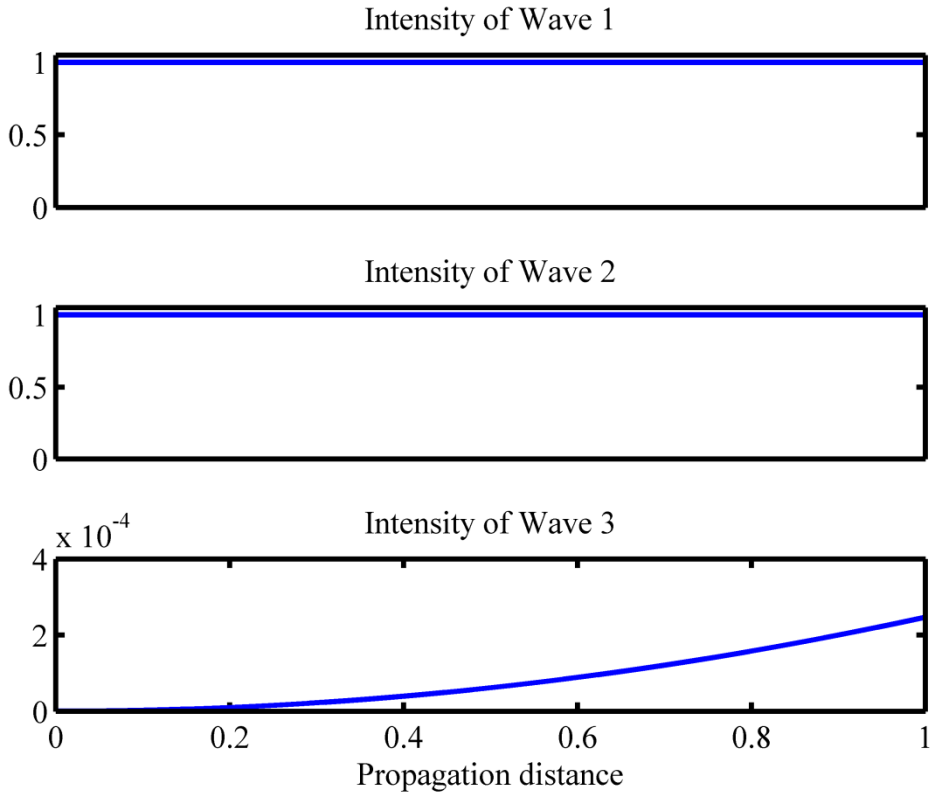

Figure 4.13. Conversion efficiency with no losses. The gain term (ie d) is the same as for the earlier plots.

By decreasing the propagation losses the efficiency increases, but not by anything like the amount required to bring this in line with the normalised conversion efficiencies quoted for other waveguide fabrication techniques. This implies that there are other significant limitations in the design, some of these are readily identified:

1. The effective nonlinearity of BiBO is less than the d_{33} nonlinearity for lithium niobate used for quasi-phase matched processes including SHG.
2. The mode size is relatively large in comparison to some other techniques; the limitation of ULI to relative index changes of ~ 10^{-3} limits the irradiances that can be guided, for a given power. Air clad structures produced by techniques such as wafer bonding and dicing can obtain far higher index contrasts, and hence field strengths, significantly increasing the normalized efficiency.
3. The pump and second harmonic modes are not perfectly overlapped. This mode mismatch between the pump and second harmonic waves decreases the efficiency.

4.8. Conclusions

While this chapter has not presented a successful demonstration of efficient SHG, it has shown that there is scope for the tailoring of type II ULI structures beyond the classic two line design. This work's greatest benefit could come in applications where polarisation combining or splitting is required. By control of the offset of the modes over a distance, it should be possible to construct integrated polarisation dependent components through ULI. With type II ULI waveguides for phase matched nonlinear optical processes, birefringent phase matching will always pose more difficulties than quasi-phase matching. Providing good mode overlap between OLP modes causes significant difficulties and can be avoided entirely for quasi-phase matched materials such a periodically poled lithium niobate. For integration into compact laser sources these materials would be preferable, however not all materials can be easily poled. For this reason further optimisation of damage line placement and the inscription parameters will be required in order to increase the quality of birefringently phase matched nonlinear processes in type II ULI waveguides.

The next chapter presents waveguide inscription in an erbium doped bismuthate glass to make a high gain, compact, optical amplifier for the telecommunication C-band. The high erbium solubility in bismuthate glass allows high gains per unit length to be realised. This gain element is built into a travelling wave fibre laser cavity and a Rigrod type analysis is undertaken.

Chapter 5. Continuous wave erbium doped bismuthate waveguide laser

In the 1990's optical fibre based communications started being used to connect most major towns and cities. At this time it was natural to think that fibre optics would become pervasive at a local metropolitan network level and then, home level (fibre to the home). Optical fibre communication is based largely in the optical C-band (1530-1565 nm) due to this region being a low loss window for optical fibre and this wavelength range being compatible with erbium doped fibre amplifiers (EDFAs). The gain per unit length from EDFAs at this time was limited by the low erbium ion solubility in silica. This problem, coupled with the prospect of fibre to the home, lead to research interest in compact, guided mode amplifiers for this spectral region, capable of higher gains per unit length than attainable from fibre. It was therefore deemed of great importance to find glass hosts with high erbium ion solubility, within which high quality optical waveguides could be fabricated. Ultimately, fibre technology has allowed for glasses other than silicates to be used for erbium doped fibres, but erbium doped waveguides are still of interest for applications requiring small footprints and for laser applications.

5.1. The trivalent erbium ion

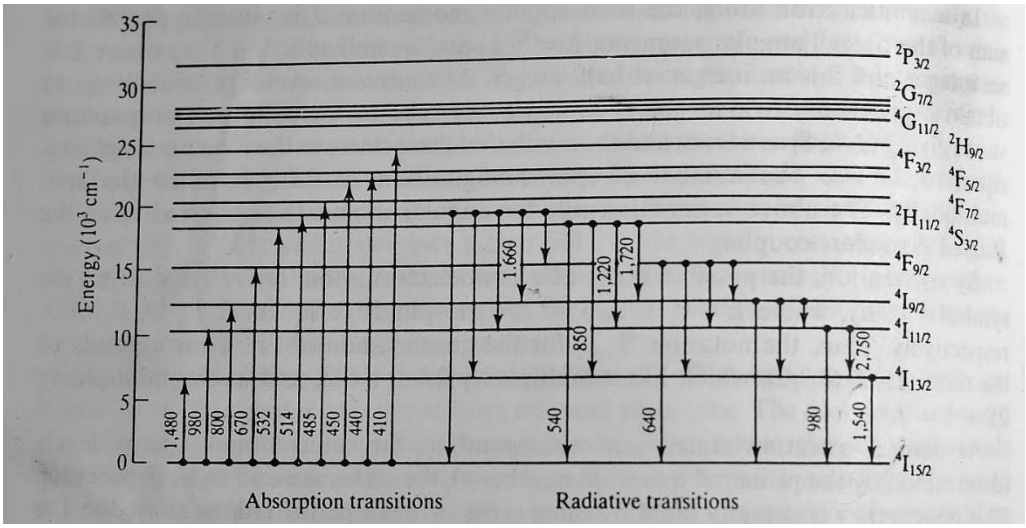

Figure 5.1. Energy levels of the Er^{3+} ions. For EDFAs, pumping between the $^4I_{15/2}$ and the $^4I_{11/2}$ manifolds is most commonly employed using 980 nm laser diodes, although pumping between the $^4I_{15/2}$ and the $^4I_{13/2}$ manifolds can be employed with 1480 nm laser diodes (in-band pumping). Gain, centred around 1540 nm, occurs from the $^4I_{13/2}$ to $^4I_{15/2}$ radiative transition. Figure taken from [98].

Trivalent erbium ions (Er^{3+}) do not have a simple electronic structure. For telecommunication applications, the emission between the quasi stable $^4I_{13/2}$ manifold and the ground state, $^4I_{15/2}$, is used, making erbium a three level system. This emission is centred at around 1550 nm, and in glasses can span multiple 10s of nm. EDFA's and erbium doped fibre lasers are most commonly pumped using high brightness, single transverse mode, 980 nm laser diodes to pump between the ground state, $^4I_{15/2}$ and the short lived $^4I_{11/2}$ energy level. In-band pumping between the $^4I_{15/2}$ and $^4I_{13/2}$ can also be used, but results in less population inversion. The doping concentration is limited by the need to avoid concentration-dependent quenching effects, such as pair induced quenching [99]. The ion concentrations at which these quenching effects start to occur are dependent on the host glass.

5.2. Erbium doped waveguide amplifier

During the second year of my PhD. R. Thomson was working on an ultrafast laser inscribed erbium doped waveguide amplifier (EDWA) in a bismuthate glass host. To learn the techniques necessary for characterisation of active waveguides I shadowed him for the duration of this work. This subsection highlights the amplifier results for the optimum waveguide from this investigation. This waveguide was later used as the gain element in a guided mode laser. The following work is described more completely in a publication in Optics Express [60].

The waveguide was fabricated in an erbium doped bismuthate glass containing > 70 wt.% Bi_2O_3 and doped with 0.63 wt.% Er, available commercially from the Asahi Glass Company, Japan. A glass of a similar composition had previously been used for an Er^{3+} doped waveguide amplifier [100], but no previous ULI investigation in high bismuth oxide content glasses had been published.

After inscription parameter optimisation, high quality waveguides were realised. The sample end facets were ground and polished at an angle of 8 ° from normal to the waveguide axis and amplifier characterisation was carried out. The waveguide was found to exhibit a significant net fibre-to-fibre gain across the whole of the optical communications C-band (>9 dB gain) and also over some of the L-band (1565-1625 nm), see Figure 5.2. Following amplifier characterisation, the waveguide was investigated for laser applications.

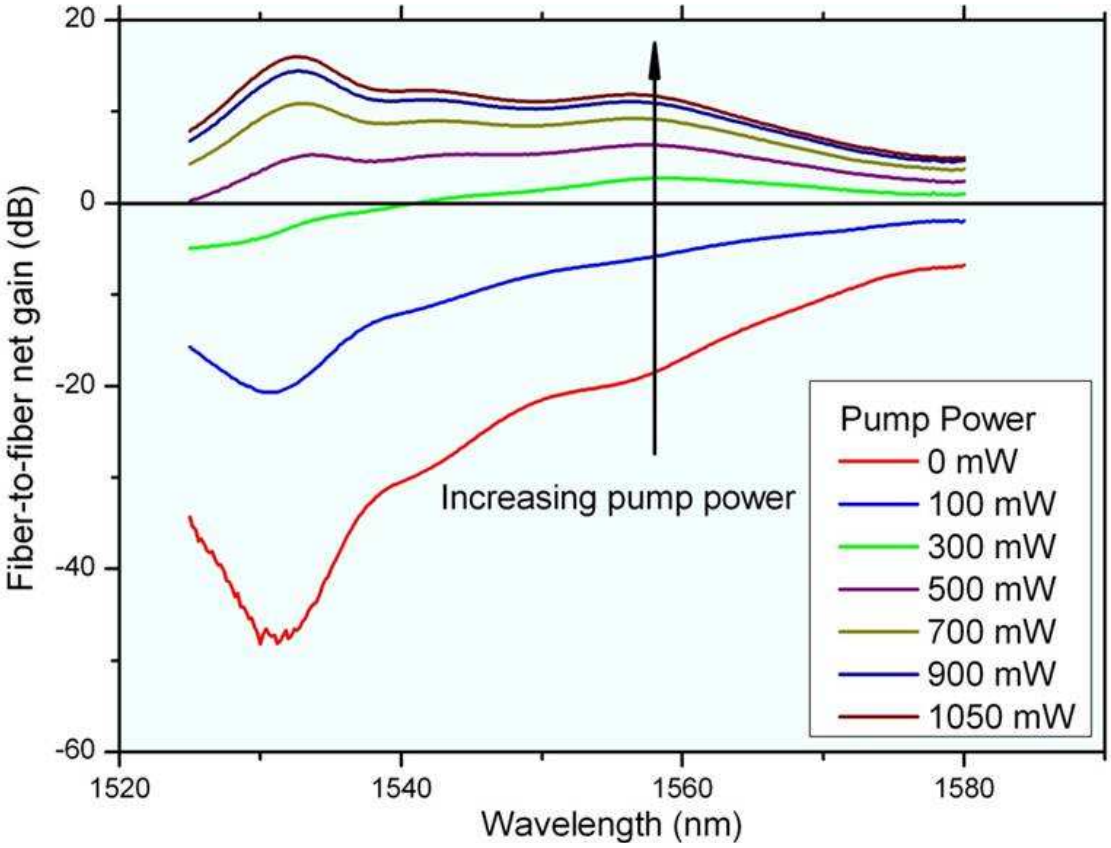

Figure 5.2. Net fibre-to-fibre gain for different pump powers. The gain peak of 16 dB is at 1533 nm. Figure adapted from data presented in [60].

5.3. Laser cavity construction

The waveguide was built into a travelling wave fibre cavity, to provide the feedback necessary to achieve oscillation. An intra-cavity fibre isolator was used to achieve unidirectionality and output coupling was accomplished using a fused fibre directional coupler, see Figure 5.3. The efficiency of energy extraction from an oscillator featuring high intra-cavity losses is dependent on the order of the intra-cavity elements. For this reason output coupling is carried out as soon after the gain element as possible. Due to mode mismatch between the waveguide and the coupler fibre used for the wavelength division multiplexers (WDMs) and the refractive index difference between these two media, a coupling loss at this interface of 0.9 dB occurs. There is a further loss of 0.45 dB due to mode mismatch between the coupler fibre and the SMF-28 used for the directional coupler. The light that is not output coupled then experiences an additional loss of ~0.5 dB, the IL for the isolator. There is a further loss of 0.45 dB, due to mode

mismatch after the polarisation controller, and of 0.9 dB when the light is reintroduced to the waveguide. The propagation loss for the waveguide was previously inferred from insertion loss and coupling loss measurements to be ~2.0 dB or 0.2 dB/cm.

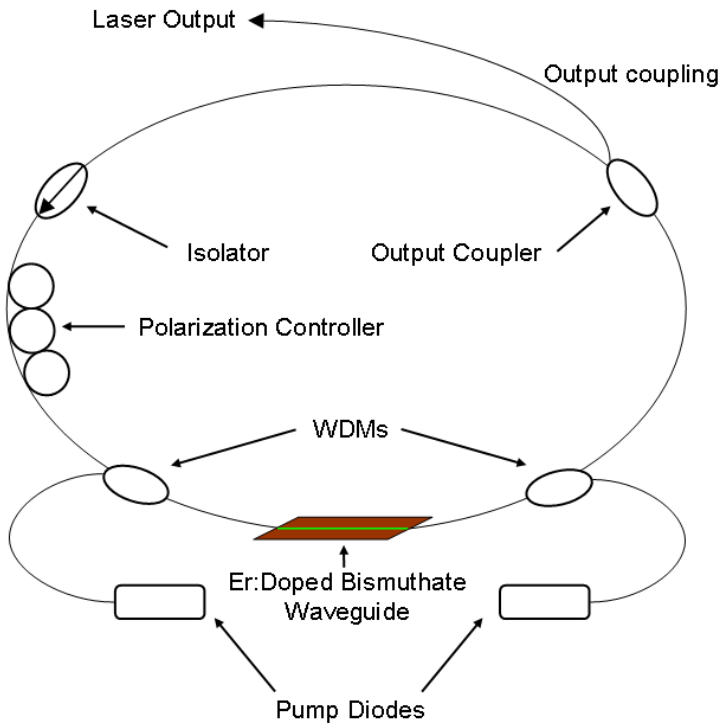

Figure 5.3. The laser cavity design: pump diodes are ~600 mW, 980 nm single mode laser diodes. WDMs are 1550/980 nm fused fibre wavelength division multiplexors, Output coupler is a fused fibre directional coupler.

The fibre cavity elements were fusion spliced together, the fibres were aligned to the waveguide and the pump diodes were switched on. The output power was measured, then a new directional coupler was fusion spliced into the cavity. This was repeated for multiple directional couplers to allow a Rigrod type analysis to be undertaken [101], it should be noted that this is a travelling wave laser cavity so the appropriate formulisation is different from the original paper by Rigrod and can be found in [102]. Appendix A looks at the applicability of a conventional Rigrod analysis to waveguide lasers, and investigates through modelling the cases where good agreement exists and where the assumptions made break down. For this system a Rigrod type analysis is valid.

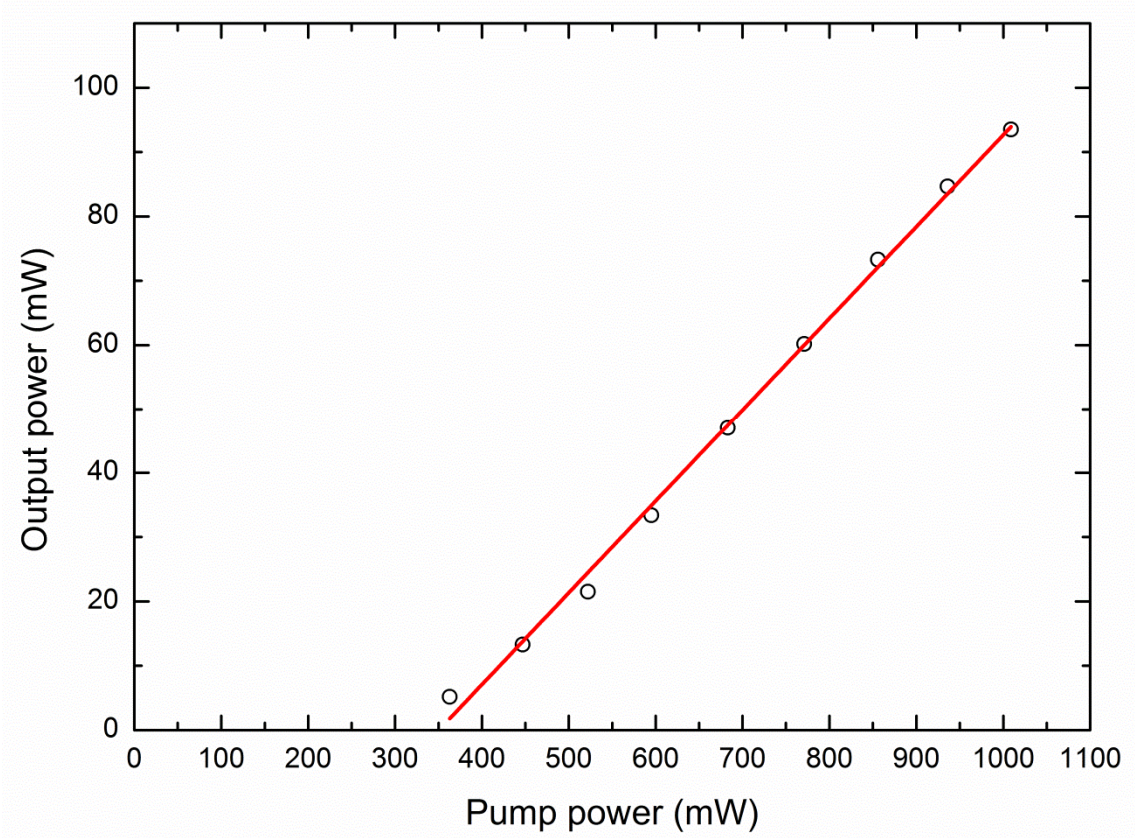

Figure 5.4. The Laser performance with 50% output coupling. The slope efficiency is 14%.

The best performance from the laser was attained for output coupling of between 50% and 60%, and the laser still oscillated with 80% output coupling. The peak optical to optical efficiency is fairly modest at ~9% but this would likely be substantially higher if the intra-cavity losses for the signal and the coupling losses for the pump could be reduced. The simplest route to accomplishing this would be by moving to a standing wave cavity design. Feedback could then be provided by dielectric mirrors, either directly coated on to the waveguide facets, or coated onto a conventional substrate and butt-coupled to the waveguide facets as reported in [103]. Feedback could also be provided by two Bragg reflectors inscribed into either end of the waveguide or a distributed Bragg reflector (DBR) structure as described by Marshall *et al.* [104].

Component/interface	Loss (dB)	Source
WG to Fibre CL	0.9	Experimentally measured
Fibre to fibre CL	0.45	Calculated from MOI
Isolator IL	0.5	Taken from spec sheet
Fibre to fibre CL	0.45	Calculated from MOI
Fibre to WG CL	0.9	Experimentally measured
Waveguide propagation loss	2.0	Inferred from measured IL and CL
Total parasitic loss for round trip	5.2	Calculated from values above

Figure 5.5. Table of cavity losses for components: WG is waveguide, CL is coupling loss, IL is insertion loss, MOI is Gaussian mode overlap integral.

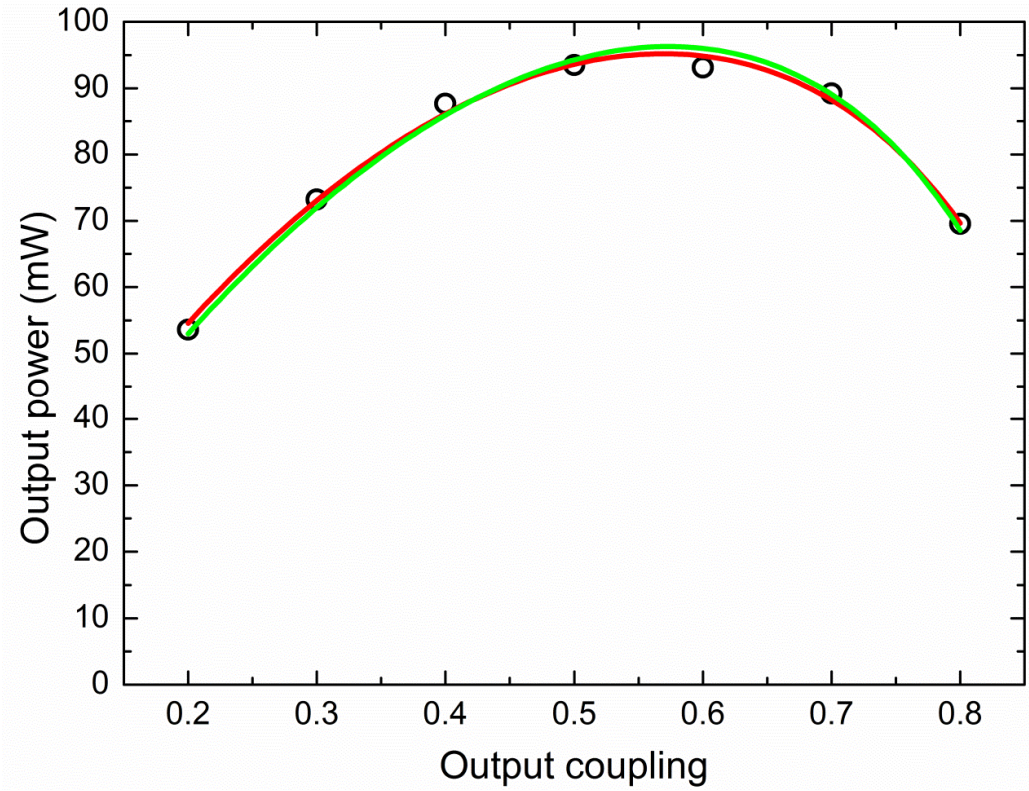

Figure 5.6. The output coupled power from the laser for 1 W of pump power. The red line shows a fit using the function from [102], with the small signal gain, cavity loss and saturation power left as free variables, values of 1.55, 0.6 and 175 respectively, are found to be the best fit values. This yields a parasitic loss lower than the total parasitic loss calculated in Figure 5.5. The green line uses the same fitting function but fixes the loss variable to the value calculated in Figure 5.5, 0.698. The best fit values for small signal gain and saturation power are then found to be 1.62 and 200, respectively.

Rigrod analysis is sometimes used instead of independent techniques for measuring the loss, small signal gain and saturation intensity of a waveguide laser system. For bulk solid state systems this type of analysis may be sufficient to extract this information, however in this case it was found that the results extracted had large uncertainties, and the loss, measured via an independent technique sat outside these bounds. Taking independent measurements by as many techniques as possible should always be undertaken if accurate results are required from any investigation. This can be seen by how close the red and green lines in Figure 5.6 are, despite the large difference between the loss values used to plot them.

5.4. Conclusions

A high gain waveguide was fabricated in an erbium doped bismuthate glass and this waveguide was shown to be suitable for use as the gain element in a fibre laser cavity. With optimal output coupling, an optical to optical efficiency of 9% was demonstrated. Further design to reduce coupling losses throughout the cavity, or reducing the number of cavity elements by moving to a standing wave configuration, would result in a substantial output power increase for the same pump power.

The next chapter looks at adapting this cavity design to incorporate a saturable absorber. By increasing the cavity round trip losses for CW operation, this element makes it more energetically feasible for the laser to run in pulsed operation. Pulses of 320 fs are extracted from the laser cavity.

Chapter 6. Modelocked erbium doped bismuthate glass waveguide laser

In the previous chapter CW operation of an Er doped bismuthate glass waveguide laser was demonstrated. In this chapter we will introduce a saturable absorber to the laser cavity to initiate modelocked operation.

6.1. Modelocking

Through control of the phases of adjacent longitudinal modes, temporal interference effects can lead to a laser producing a pulsed output with an inter-pulse spacing of the cavity round trip time [105]. This 'locking' of the phase of longitudinal cavity modes is referred to as modelocking. Modelocking can be achieved by an intracavity element with a loss which varies, either temporally at the cavity repetition rate (active modelocking), or with incident power so as to favour the high intensities produced by a pulsed source in comparison to a CW source (passive modelocking).

6.1.1. The role of dispersion

By Fourier analysis it can be shown that a short pulse must consist of a range of spectral frequencies. To decrease pulse durations, the spectral bandwidth of the pulse must increase. A pulse of the shortest duration for a given spectral bandwidth is called bandwidth limited. The different spectral components of a polychromatic wave travelling through a dispersive medium travel with different velocities and consequently a bandwidth limited pulse will spread out in time and acquire a chirp (a time dependent spectrum). In the absence of other effects a bandwidth limited pulse, injected into a laser cavity will temporally spread out over the course of many cavity round trips. This increase in pulse duration, coupled to the spectral narrowing of a gain medium, will lead to a narrow bandwidth CW laser output.

6.1.2. The role of nonlinearities

As explained in Section 2.2, at sufficiently high intensities, for example at the focus of a modelocked laser cavity, nonlinear optical effects can occur. Of particular importance for modelocked lasers is the $\chi^{(3)}$ based optical Kerr effect. This manifests as an intensity dependent refractive index, capable of providing spectral broadening for a time varying

electric field. By increasing the bandwidth of a short pulse, coupling light into adjacent longitudinal modes, while maintaining the phase difference between the adjacent modes, it can potentially decrease the pulse duration. A pulse propagating in a medium with Kerr nonlinearity also sees a chromatic dispersion from this effect, for this reason most short pulse solid state lasers are constructed such that the cold cavity dispersion is anomalous for media with a positive Kerr nonlinearity. This anomalous dispersion, in addition to the intensity dependent positive dispersion from the optical Kerr effect, can lead to a zero round trip dispersion for a pulse of a certain duration and pulse energy. This balancing of the linear dispersion and nonlinear dispersion leads to a "wave of translation", a pulse envelope which does not change as the pulse propagates, this is called a soliton. The optical Kerr effect also has significance for modelocked lasers because its lensing effect can be used, through appropriate cavity design, as a saturable absorber (Kerr lens modelocking).

6.1.3. **The role of the saturable absorber**

Passive modelocking is often preferable to active modelocking. Passive modelocking typically produces shorter pulses than active modelocking and does not require any electronic external modulation, which must be carefully synchronised to the cavity round trip time. Three different regimes exist for achieving short pulses through modelocking with a passive saturable absorber [106].

1. Fast saturable absorber: for this regime the loss from the saturable absorber is dependent on the instantaneous power, see Figure 6.1 (a). This effect is very fast and can lead to the shortest pulses directly from an oscillator. Examples of this regime include the Kerr lens modelocked Ti:Sapphire laser and the nonlinear polarisation evolution (NPE) fibre laser.
2. Slow saturable absorber and a gain medium which experiences dynamic gain saturation: this system has a slow saturable absorber, whose loss is dependent on the energy absorbed by the saturable absorber from earlier in the pulse. This leaves a window of reduced loss open for a long period after the pulse has finished. The reason the pulse does not build up a tail behind it is because the gain medium has been depleted of its population inversion, so the gain experienced is significantly reduced for the final part of the pulse, see Figure 6.1 (b). Examples of this include a dye laser with gain provided by a dye and

another dye used as a saturable absorber and a semiconductor laser with a semiconducting saturable absorbing mirror (SESAM).

3. Slow saturable absorber and a gain medium with steady state gain saturation: as in point 2 (above), a window of low loss is left after the pulse has finished, however in this case there is still gain available. The laser output can remain pulsed if the tail the pulse grows behind it increases at the same rate as the leading edge of the pulse is absorbed by the saturable absorber, see Figure 6.1 (c). Examples of this include a SESAM modelocked solid state laser and a carbon nanotube modelocked fibre laser.

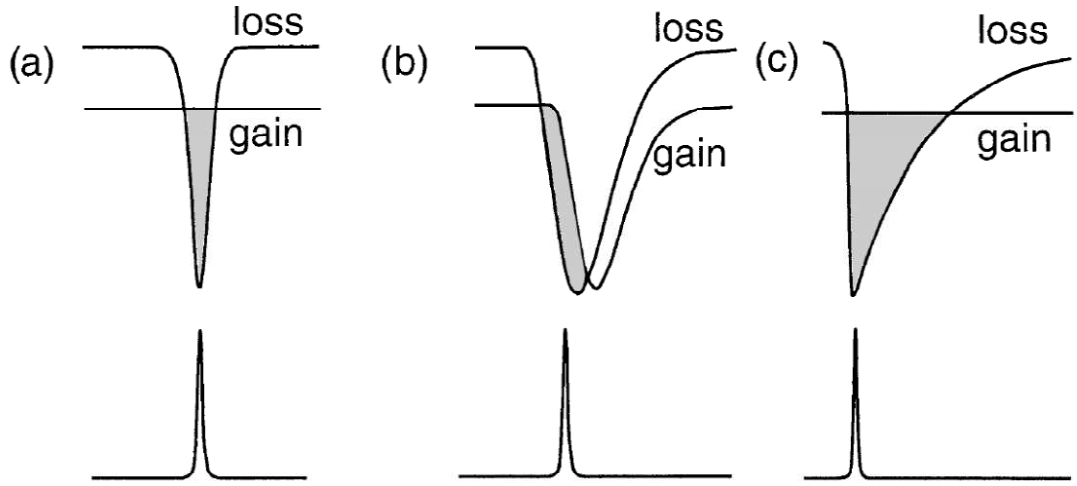

Figure 6.1. The role of time dependent loss and gain as pulse shaping mechanisms. (a) A fast saturable absorber and temporally flat gain. (b)A slow saturable absorber and dynamic gain saturation. (c) A slow saturable absorber and temporally flat gain. Figure taken from [106].

6.1.4. **Ultrafast fibre lasers**

In most free space, solid state, modelocked lasers the round trip gain is relatively low and spectral broadening occurs over a short length relative to the length of the cavity (typically a few hundred microns of the meter long cavity). The pulse duration and spectral width remain relatively constant over a round trip, however this is not the case for all designs of guided mode ultrafast oscillators. Described below are two fundamentally different designs of ultrafast fibre oscillator. The first design has two different examples given. For illustrative purposes a Matlab® simulation of each has been carried out based on the split step Fourier method popularised by G. Agrawal [107]. The code used is based on the generalised nonlinear Schrödinger equation

(GNLSE) code distributed by Professor John Dudley at the Scottish University Summer School in Physics (SUSSP 66) in the summer of 2010. The code has been adapted to add a spectrally dependent gain, including steady state gain saturation. The cavities are constructed from different segments of fibre, output couplers and saturable absorbers. The simulation is run for multiple round trips of the laser cavity. The simulations have not been run to their conclusion and include the initial build up before a steady state has been reached. These figures are for illustrative purposes only. By request of Professor Dudley the code is not included as an appendix.

Conventional soliton modelocking

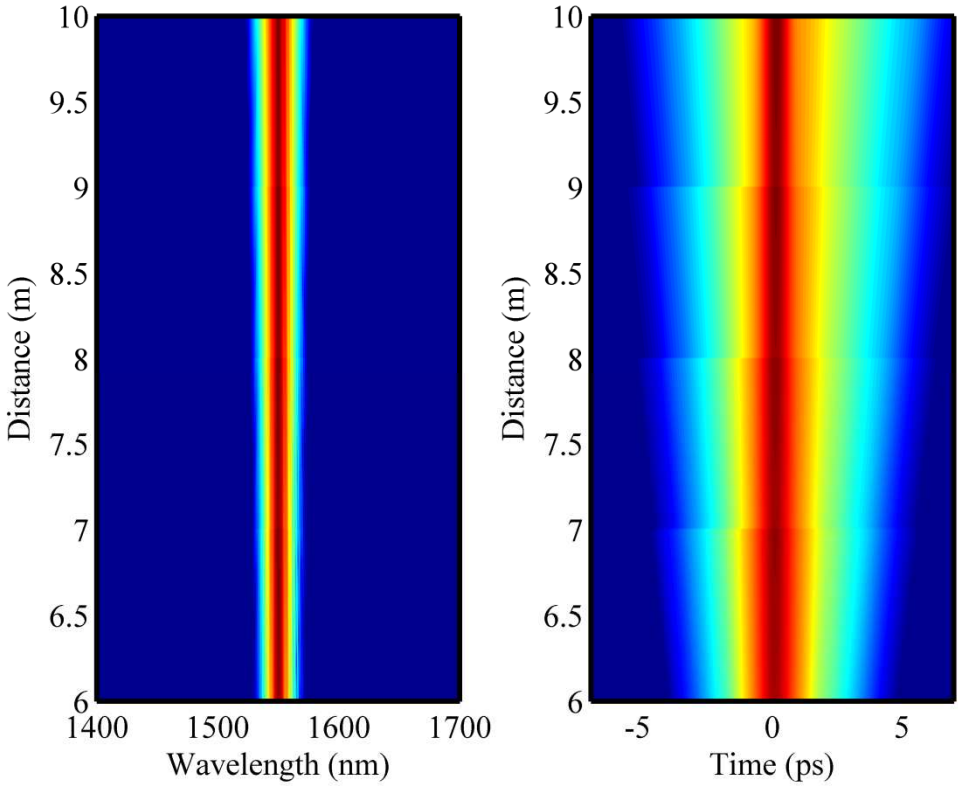

Figure 6.2. 10 round trips of a soliton fibre laser cavity while the laser approaches steady state operation. At steady state roundtrip changes in spectral width and pulse duration are minimal.

The 1 m fibre cavity has a uniform, anomalous dispersion map. The pulse maintains a duration close to bandwidth limit throughout the cavity, allowing output coupling of a bandwidth limited pulse from any cavity position. Soliton area theorem limits the peak power and pulse duration of stable modelocking for a given fibre type. The dominant shaping mechanism for the pulse is the soliton (dependent on the dispersion of the fibre,

the nonlinearity of the fibre and the energy of the pulse), as the saturable absorber only acts to initiate modelocking and to stabilise it by reducing ASE.

Dispersion managed soliton (breathing soliton)

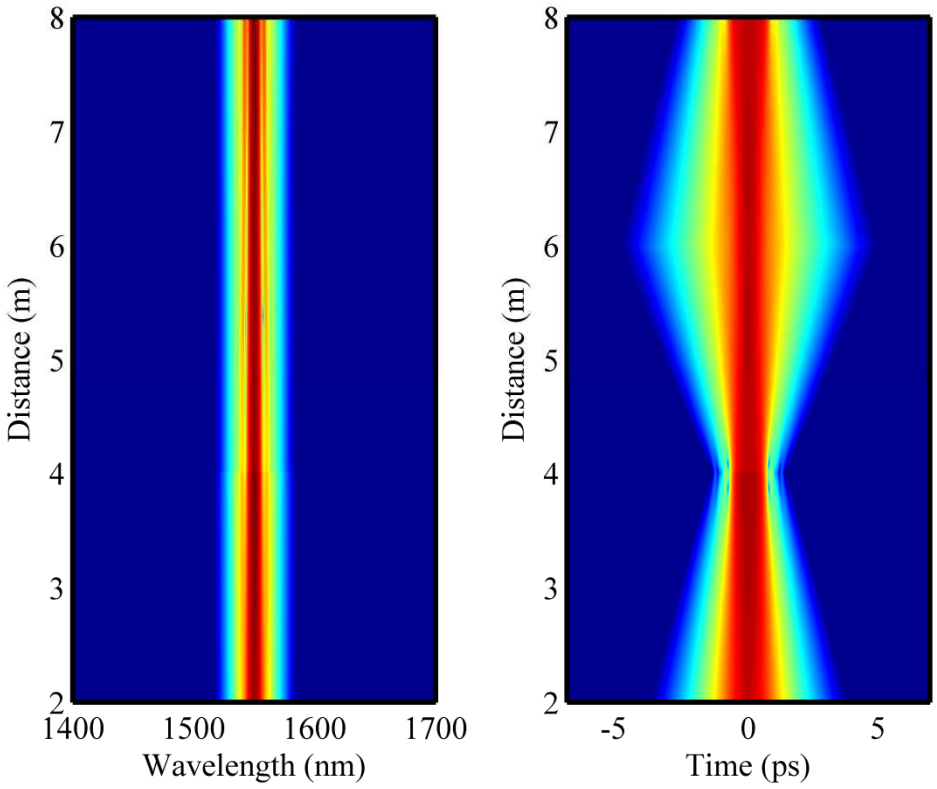

Figure 6.3. One cavity round trip of a dispersion managed soliton fibre laser approaching steady state. At steady state round trip changes to the bandwidth are minimal but the pulse duration 'breathes', this means the pulse is only bandwidth limited for a small distance on each round trip.

The cavity has two fibre segments with different dispersions, one is positive and the other is negative. The lengths of these two fibres are selected such that the net cavity dispersion is anomalous. The breathing of the soliton decreases the average intensity of the pulse over its round trip, allowing higher peak powers for the pulse when at bandwidth limit than attainable for a conventional soliton laser. The spectrum does not change substantially throughout the cavity but pulse duration does. Output coupling must occur at the correct position to achieve bandwidth limited pulses, but can occur anywhere if compensation for the pulse's chirp is to be used.

All normal dispersion (ANDi) laser

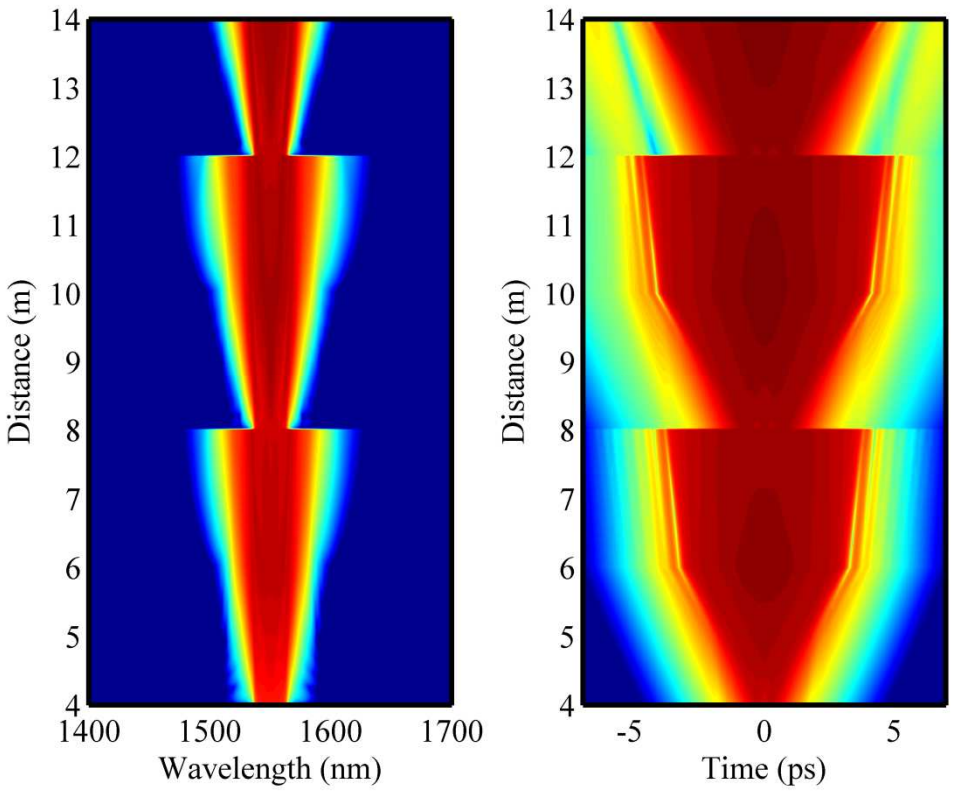

Figure 6.4. All normal dispersion (ANDi) fibre laser approaching equilibrium. Both the spectral width and the pulse duration change by large amounts on each round trip. The pulse is never at bandwidth limit.

For the all normal dispersion fibre laser, the cavity only consists of normally dispersive fibre making soliton propagation impossible. At no point in the cavity is the pulse at bandwidth limit, but instead it has a strong linear chirp. The pulse is at its shortest when its bandwidth is smallest, typically a few nm FWHM. It is then amplified in a section of gain fibre before spectral broadening occurs in a passive fibre. Output coupling then occurs, followed by spectral filtering of the pulse. Since the pulse has a linear chirp removing the spectral wings also removes the temporal wings from the pulse. Here the dominant shaping mechanism is the spectral filter, the saturable absorber acts only to initiate and stabilise the modelocking. Output coupling can only occur at one point and external compression of the chirp is required for femtosecond pulse durations.

6.2. Laser design

6.2.1. Cavity design

The waveguide was built into a fibre cavity similar to that described in Chapter 5, but featuring a single walled carbon nanotube (SWNT) saturable absorber, see Figure 6.5. The saturable absorber was obtained through a collaboration with the Nanomaterials and Spectroscopy Group in the Department of Engineering at The University of Cambridge. The cavity contained 239 cm of Corning® SMF-28, 112 cm of Corning® Flexcore 1060, 152 cm of OFS Clearlite® 980-16 and the 87 mm Er-doped bismuthate waveguide. The linear dispersions of these components at 1560 nm are estimated by their manufacturers to be 17.9 ps/nm·km, 8.0 ps/nm·km, -1.0 ps/nm·km and -120 ps/nm·km respectively, resulting in a net cavity dispersion of 40 ± 2 fs/nm (-0.051 ps^2). This anomalous net cavity dispersion enables soliton modelocking.

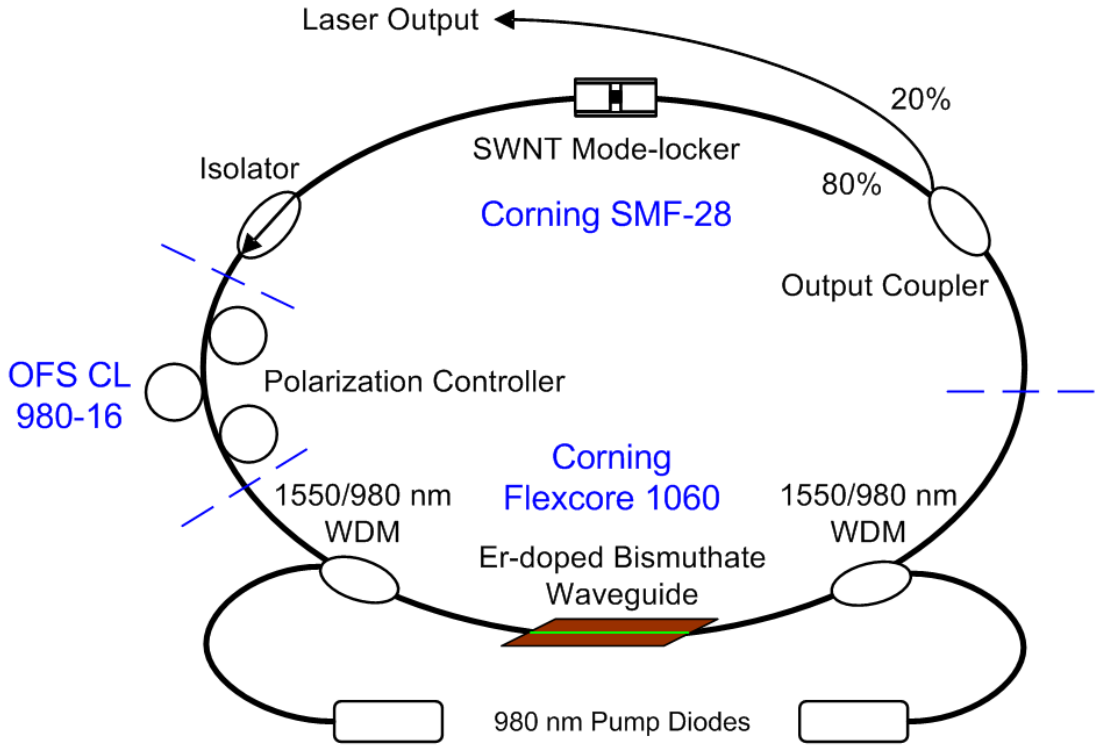

Figure 6.5. Cavity diagram: SWNT modelocker is the single walled carbon nanotube saturable absorber. WDM is 980/1550 nm wavelength division multiplexer. Fibre types for the different sections are shown in blue.

6.2.2. **The saturable absorber**

Our collaborators at The University of Cambridge fabricated a fibre coupled SWNT saturable absorber for use close to 1550 nm, see Figure 6.6. The SWNTs are exfoliated through strong ultrasonification in ortho-dichlorobenzene (O-DCB). The dispersed SWNTs are then centrifuged to remove large unexfoliated bundles which would otherwise act as scattering centres. The upper 90% of the supernatant is then collected and filtered through a 1 μm glass filter and sonicated with polycarbonate pellet for 1 hour. The mixture is drop cast in a petri dish and left in a vacuum chamber at room temperature. Slow evaporation of the O-DCB results in a 30 μm thick SWNT polymer. The absorption peak of the SWNT polymer is ~1600 nm, corresponding to the first optical transition in the semiconducting tubes. The thin film polymer was then sandwiched between two FC/PC fibre connectors in a fibre bulkhead. The connectorised device had a small signal transmission of ~ 80% and was expected from previous experiments to have a modulation depth of ~9% (this value was not measure for the device used but is expected based on measurements of other devices fabricated under the same conditions by the group).

Although the transparency of polycarbonate at 1550 nm is high, some absorption still occurs. For this reason the average power incident upon the saturable absorber must be limited to avoid thermal issues that ultimately lead to catastrophic failure of the device. An average power of 5 mW had previously been shown to cause no degradation over extended periods (many months), so this value was chosen as an initial limit to the intracavity average power.

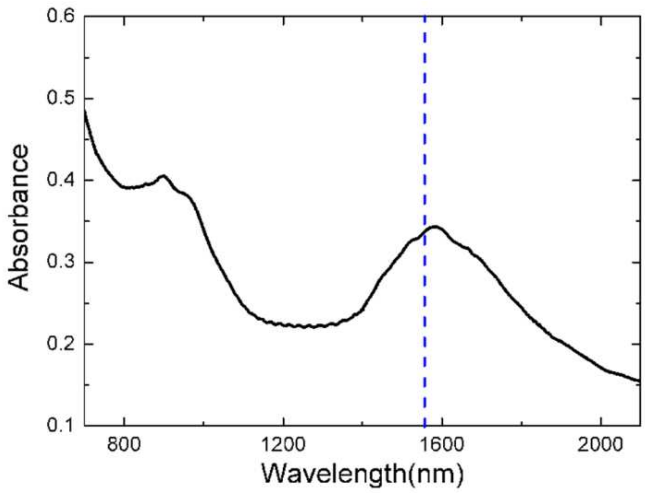

Figure 6.6. The linear absorbance of the single walled carbon nanotube saturable absorber under low intensity irradiation. The dotted line shows 1550 nm.

6.3. Laser performance

The pump diodes were turned on and ramped up while observing the average power coupled out of the cavity until 1.25 mW was reached (corresponding to 5 mW of average power at the SWNTs). This occurred for 130 mW of co-propagating and 220 mW of counter-propagating 980 nm pump light. A fast photodiode and RF spectrum analyser confirmed a 40 MHz pulse repetition frequency, corresponding to the fundamental repetition frequency of the cavity. No Q-switching instabilities were observed. The output coupled laser light was collimated by a connectorised singlet lens and input into a home built nonlinear, Michelson type, collinear autocorrelator. The interferometer was constructed from a wedged plate beamsplitter, a loud speaker with a gold mirror glued to its centre and another identical gold mirror mounted on a manual micrometer screw gauge. For the nonlinear detector a singlet aspheric lens focussed the output from the interferometer onto a silicon photodiode. The bandgap of silicon corresponds to a photon with a wavelength of ~1 μm making it transparent to 1550 nm radiation. Two photon absorption in silicon can occur for high intensity 1550 nm irradiation making silicon a suitable, readily available, nonlinear detector for use in an autocorrelator. The voltage from the silicon photodiode was viewed on an oscilloscope while a sine wave from a signal generator was used to translate the mirror mounted on the loud speaker. The amplitude of the speaker movement was selected so that the autocorrelation trace occurred over a small section of the speaker's movement, close to the equilibrium position. This ensures that the speaker's movement can be well approximated as linear over the range of interest. The intracavity polarisation controller was adjusted to minimise pulse duration and then the oscilloscope trace was captured. The laser was left for 30 minutes and another oscilloscope trace was captured to check stability of the system.

The captured traces were loaded into a graphing program (Origin®) and the time spacing (in scope time) between fringes was used to calibrate the time base of the autocorrelator, based on the knowledge that the laser was operating at 1560 nm and that the speed of light is 2.998×10^8 m/s. The interferometric autocorrelation was then smoothed by applying adjacent averaging across the entire waveform to remove the fringes and leave an intensity autocorrelation. The FWHM pulse duration from this intensity autocorrelation was then measured to be 490 fs. This corresponds to a pulse duration of 320 fs, assuming a deconvolution factor of 0.65 for a sech^2 temporal pulse profile,

consistent with soliton modelocking stabilised by a slow saturable absorber. Figure 6.7 presents the autocorrelation of the laser output, no measurable difference was observed between the autocorrelations taken 30 minutes apart.

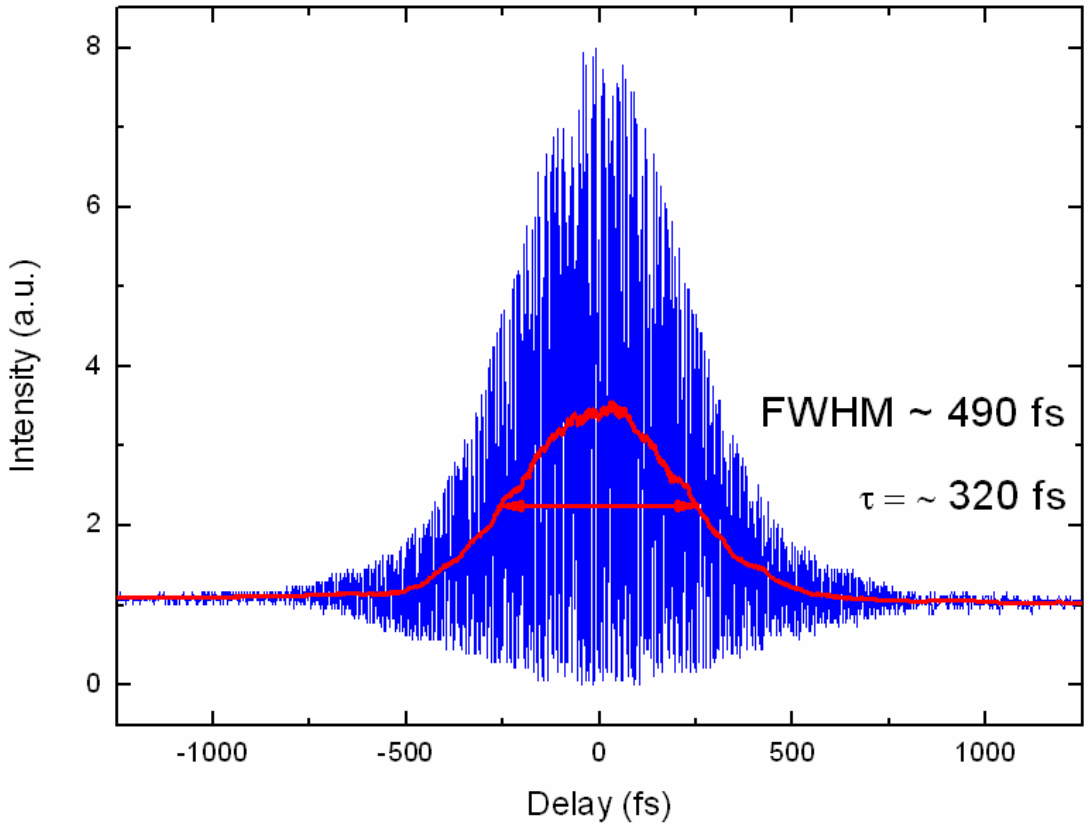

Figure 6.7. A nonlinear autocorrelation of the laser output. Blue: the interferometric autocorrelation, Red: the inferred intensity autocorrelation.

The laser output was then coupled into an OSA, see Figure 6.8. The laser had a FWHM spectral bandwidth of 8.9 nm, yielding a time bandwidth product of 0.351, close to the bandwidth limit of 0.315. This small discrepancy can be accounted for by the 0.8 m length of SMF-28 between the cavity and the autocorrelator.

Strong spectral sidebands are visible in the optical spectrum produced by the laser. These result from phase matching between the soliton-like pulse and the dispersive waves shed by the soliton-like pulse as it experiences the loss, gain and different dispersion characteristics of the cavity components [108]. Over multiple round trips the components of the dispersive wave resonant with the soliton-like pulse can be enhanced, allowing us to estimate the total cavity dispersion from the offset of the spectral sidebands, see Figure 6.9 [109]. Assuming the pulse is bandwidth limited within the

cavity and neglecting all dispersive terms above the 2nd order, the total cavity dispersion is estimated to be 42 ± 2 fs/nm (0.054 ps^2), in excellent agreement with the cavity dispersion calculated from the characteristics of the optical fibres and substrate given by the manufacturers. These results were published in Applied Physics Letters [110].

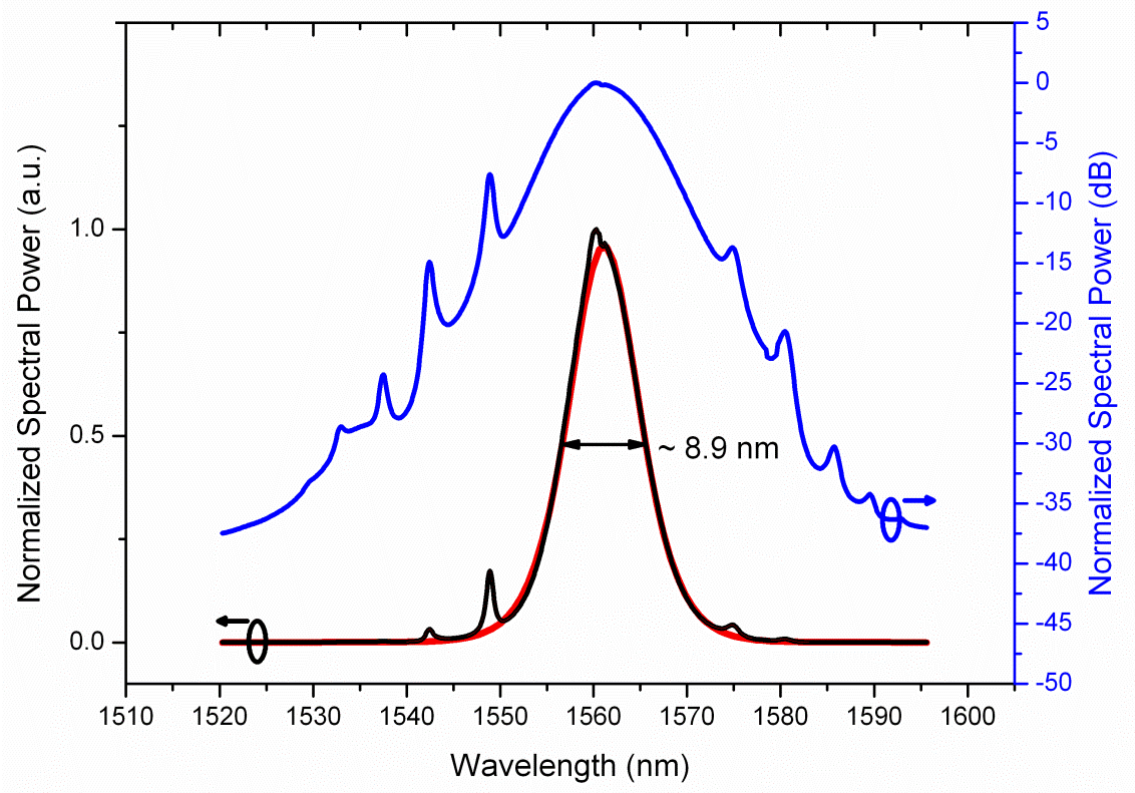

Figure 6.8. The optical spectrum of the modelocked laser. Blue shows a logarithmic scale. Black shows a linear scale with red a sech^2 fit to the linear scaled spectrum with the resonant sidebands masked.

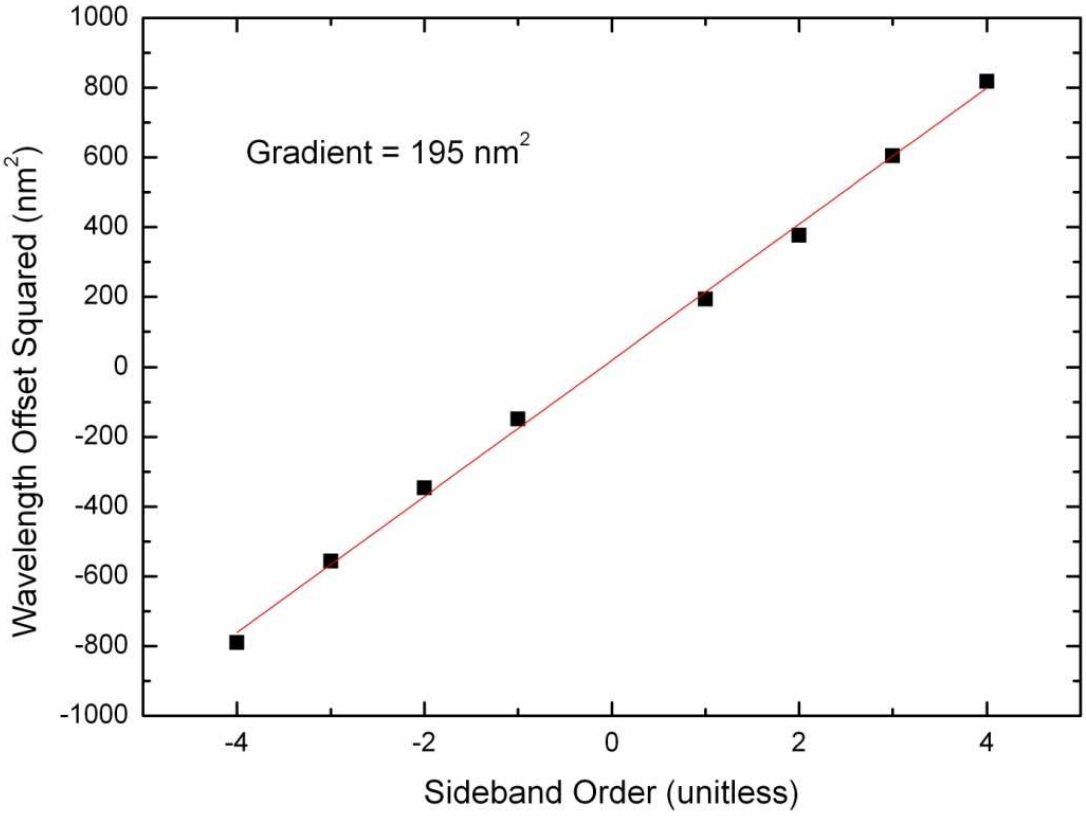

Figure 6.9. Cavity dispersion calculation. The square of the offset of the central position of the sidebands are plotted and a linear fit applied.

6.4. Conclusions

In conclusion the applicability of ULI waveguides to femtosecond pulse generation has been demonstrated. Self starting, single pulse modelocking was demonstrated with a pulse duration of 320 fs. While the specifications of this laser could be more simply achieved using a commercial erbium doped fibre as the gain element, the performance would be difficult to achieve using a piece of only 83 mm. Further work should concentrate on the integration of cavity components to decrease the cavity length, leading to higher repetition rates - hopefully reaching the 1 GHz level. For dispersion managed NPE lasers, repetition rate limits are often the direct result of the gain fibre length (typically in excess of 0.4 m), so high gain ULI waveguides could be of real use for increasing the repetition rate of these lasers. Other work should concentrate on the amplification of ultrafast laser pulses within these waveguides, the strong spectral dispersion should allow high peak powers (for a given core size) before wavebreaking effects are observed. Chapter 8 numerically investigates parabolic pulse amplification of femtosecond pulses within the waveguide used as the gain element for this study.

In this chapter we demonstrated that a ULI device could be used as the gain element in a femtosecond laser. The repetition rate was limited by the length of the fibre components required. In Chapter 7 we will look at working towards the integration of the SWNT saturable absorber with ULI technology to allow for higher repetition rates.

Chapter 7. Towards the integration of single walled carbon nanotube polymer composites with ULI waveguides

7.1. High repetition rate modelocked lasers

From the last chapter it should be clear that one of the major obstacles in achieving fundamental, high repetition rate (>200MHz) modelocking from a guided mode laser is reducing the fibre length between components. ULI has shown applicability to the fabrication of most of the fibre coupled components in Figure 6.5, including directional couplers [111], and WDMs. This leaves two components to address: the optical isolator and the integrated saturable absorber. Optical isolators are most normally based on the Faraday rotation of light in a strong magnetic field. Commercial fibre isolators are micro-optic devices, collimating the fibre input, before having small bulk optics to polarise and rotate the light. Due to the difficulties in the device manufacture of isolators, the saturable absorber was selected as the first of these components to attempt to fabricate by ULI.

Two schemes were investigated for their applicability to this problem. The first relied on the ability of ULI to accurately align waveguides and regions for removal by selective chemical etching. The second relied on an evanescent interaction from a device of similar design to that described in Section 3.2.

7.2. Slotted waveguides

7.2.1. Design and fabrication

This device was designed to operate in the same manner as the existing connectorised SWNT device. A waveguide would intersect a narrow channel, which could be filled with a solution similar to that drop cast into the petri dishes for SWNT modelocker fabrication.

Straight waveguides were inscribed in the fused silica sample with the same parameters described in Chapter 3. A waveguide was written, commencing and terminating inside the substrate. After this, another waveguide was written such that the two waveguide axes were aligned, this allowed coupling from one waveguide into the other. This was repeated and the distance between the waveguide pairs was varied. An initial distance of

0 μm was used (the waveguides ends met) and this distance was increased by 0.5 μm for each waveguide pair. After a complete set were inscribed, the laser parameters were changed. The pulse energy was increased to 800 nJ and the polarisation was changed to be linear, perpendicular to the translation direction and then a channel was inscribed. The channel was one scan wide and started 300 μm below the substrate surface, another scan occurred, parallel to the first but with the substrate lowered by 4 μm. This was repeated until the substrate was below the laser focus. The sample was then etched in dilute HF in an ultrasonic bath at room temperature for 1 hour, at which point the sample was rinsed in deionised water and inspected under the microscope. A schematic of the device is shown in Figure 7.1.

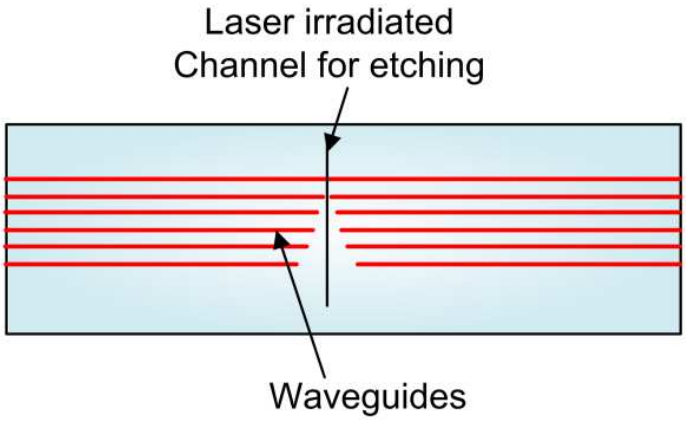

Figure 7.1. Slotted waveguide schematic. Waveguides are inscribed with a gap between them, a channel is then inscribed and etched out.

The waveguides which terminated close to the channel showed signs of etching, implying that the sample had been etched for long enough that the material in the channel would be removed. Figure 7.2 shows the channel before and after etching.

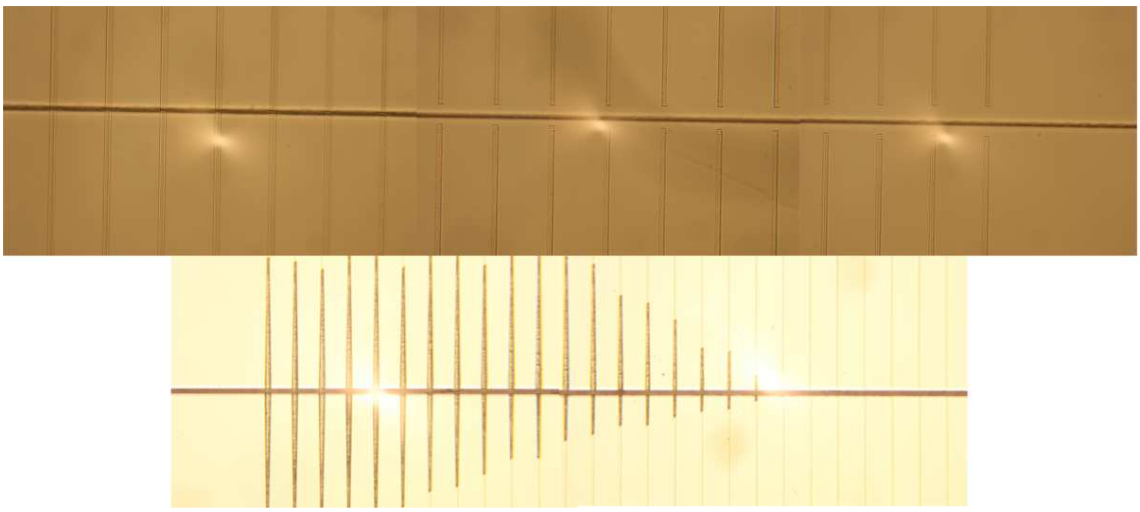

Figure 7.2. Top: the sample before etching, this image is a collage of three microscope images, the left image shows the end with the smallest spacing between the waveguides and the right image the end with the largest spacing between the waveguides. Bottom: the sample after etching, this image is a collage of two microscope images, showing the decrease in the length of the etched region in the waveguides as the distance between the waveguide pairs was increased.

With the central region etched, the sample was sent to our collaborators at The University of Cambridge for deposition of the SWNT polymer. The SWNT polymer was prepared as described in Section 6.2.2, and drop cast into the channel. The sample was then returned to our labs for characterisation.

To avoid etching the outer waveguide facets, the waveguides had been terminated inside the sample. The waveguide ends were cut off with a diamond band saw by Neil Ross, Heriot-Watt University, to leave waveguides 16 mm long, this did not leave a well polished face but further polishing was deemed unwise for fear of delaminating the SWNT polymer from the fused silica substrate. In the future, polishing of the sample should be carried out prior to SWNT polymer deposition.

7.2.2. **Nonlinear characterisation**

For nonlinear characterisation, Keith Serrels from the Ultrafast Optics Group, Heriot-Watt University, kindly allowed me to use an NPE, dispersion managed soliton, erbium doped fibre laser that he had built. The laser was turned on, the waveplates adjusted to give stable modelocking and the pulse duration was measured with a nonlinear autocorrelator, similar to that used to measure the duration of the laser described in Chapter 6. The pulse duration was measure to be ~100 fs. The NPE laser had a linearly polarised free space output, this was coupled via an isolator, two mirrors

and a variable attenuator (reflection type) into a single element aspheric lens for coupling into the waveguide. The waveguide output was imaged onto a phosphor coated CCD to allow the waveguide pair with the smallest separation and no signs of etching to be located. The light emerging from the waveguide was then imaged onto a calibrated power meter. An input/output measurement for the waveguide was conducted with the setup shown in Figure 7.3.

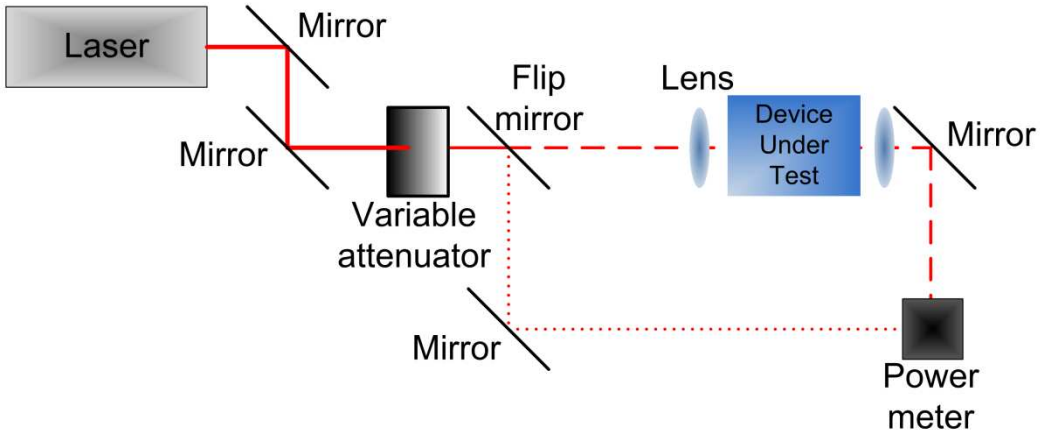

Figure 7.3. Schematic of the setup for input/output experiments. By flipping the flip mirror, the path that the beam takes is selectable. The variable attenuator allows the pulse energy to be controlled.

The transmission of a saturable absorber should increase as the pulse energy of the input light is increased, until it approaches a point where only the nonsaturable loss remains. Figure 7.4 presents the results of the input/output experiment for the slotted waveguide. The green line shows a fit to the theoretical behaviour of a saturable absorber, with the third data point (an outlier) masked. The blue line shows a theoretical fit with all the data points included. The device shows the expected shape for a saturable absorber, best fitted using a modulation depth of ~9% and a saturation pulse energy of ~0.18 nJ. These values are close to ideal for the modelocking of fibre lasers. Unfortunately the nonsaturable losses of this device are of the order of 60%, substantially higher than for the device this aimed to replace.

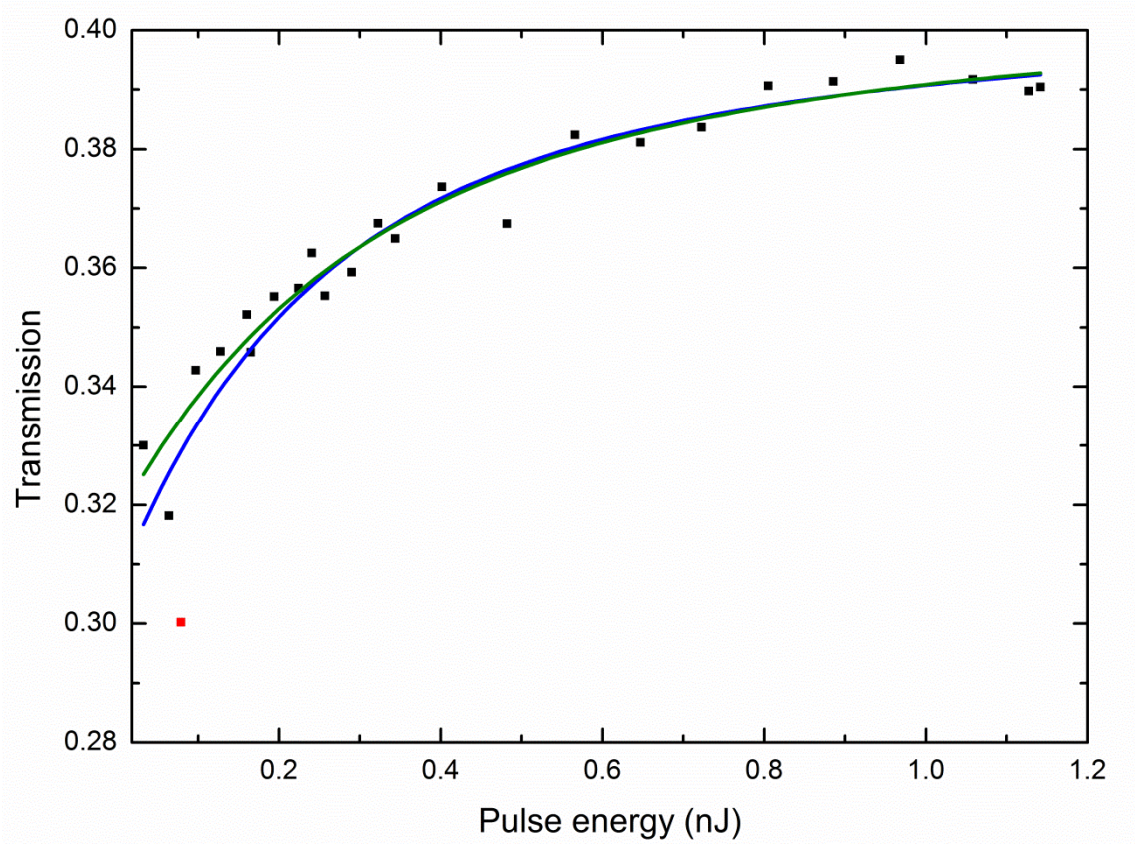

Figure 7.4. Input/output measurements on the slotted waveguide device. The green line is a fit with all the points used, yielding values of 0.593, 0.089 and 0.178 nJ for the nonsaturable losses, modulation depth and saturation energy. The blue line is the same fit but with the red point, an outlier, masked. This yields best fit values of 0.595, 0.098 and 0.14 nJ respectively.

A fibre laser cavity was constructed, similar to that shown in Figure 6.5 but with a 0.5 m length of Leikki^{TM} Er doped fibre replacing the gain element and the fibre coupled saturable absorber replaced with the slotted waveguide device developed in this section. Considerable time was spent optimising the alignment into the waveguide, adjusting the polarisation controllers and varying the pump power. However no modelocking was obtained. It was concluded that no successful result was likely to be obtained with this setup. This is probably due to the high nonsaturable losses, although other devices with similar performance characteristics have previously successfully been used to modelock fibre lasers.

7.3. Evanescent field waveguides

The side-polished fibre-like waveguide fabricated in Section 3.2 was sent to our collaborators at the University of Cambridge for the deposition of SWNT polymer onto

the top surface. The host polymer used for deposition was polyvinylalcohol (PVA) due to the ability to make larger homogenous areas than for the polycarbonate used for the other SWNT devices [112]. Characterisation of the device upon it's returned showed a significant increase in the device insertion loss. Nonlinear characterisation, as described in the previous section, showed no saturation for pulse energies up to 1.1 nJ. Literature on the subject showed that the polymer used for the deposition has a refractive index higher than that of the waveguide core (~1.45) , so the thick film above the waveguide would cause loss in the same manner as the high index oil used in Section 3.2.3, [113]. In response to this, two new glasses, N-SSK5 and N-LAK (Schott®) were selected for the investigation of evanescent devices. These glasses were selected due to their refractive indices being slightly higher than that of the host polymer, allowing effective penetration of the evanescent field. Neither of these glasses, to the best of the author's knowledge, had previous reported studies of ULI within them, so a full parameter investigation was necessary. Based on successful inscription of waveguides sufficiently close to the substrates surface for interaction between the mode and an external medium in fused silica, the parameters for this work were used as a starting point for waveguide inscription in the N-SSK5 and LAK-14 glasses.

7.3.1. **Waveguides in N-SSK5**

Inscription using a 0.67 NA objective and the multiscan technique described in Section 2.7.4, for 500 kHz repetition rate, circular polarisation and scan speeds of 1, 2, 4 and 8 mm/s for pulse energies between 575 and 95 nJ resulted in no positive index change. Negative index change was seen for the higher pulse energies, but no guiding was observed for the multiscan structures.

A cladding-written structure was investigated, this structure was fabricated by modifying the region surrounding the unmodified waveguide core, see Figure 7.5. Guiding was demonstrated, but only for large modes, ~20 µm diameter, inhibiting the possibility of low loss coupling to SMF-28. However, with development this structure may be of use for integration with large mode area fibre oscillators.

Figure 7.5. Microscope image of one of the cladding written waveguides inscribed in N-SSK5.

7.3.2. **Waveguides in LAK-14**

The same parameters were investigated for inscription in LAK-14. After inscription, viewing of the sample with a transmission microscope showed structures which appeared to be peppered with inhomogeneous damage, however the structures guided light.

Initial observations with a phosphor coated CCD showed the waveguides inscribed with pulse energies between 575 and 400 nJ all supported multiple transverse modes. The waveguides inscribed at lower pulse energies were single mode, until ~ 200 nJ, at which point the structures became very weakly guiding. The insertion losses to an SMF-28 transmission line for 1550 nm light are shown in Figure 7.6, the region of lowest insertion loss is highlighted in green.

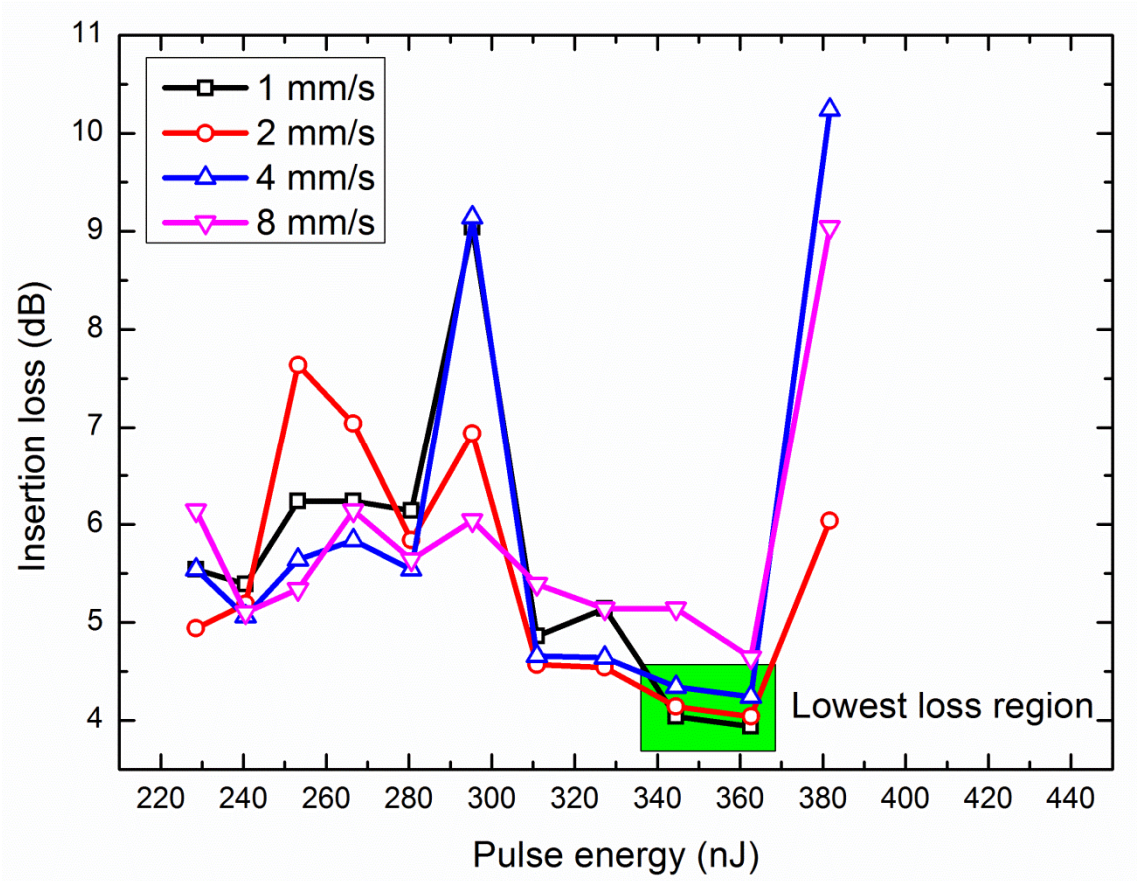

Figure 7.6. The insertion loss to an SMF-28 transmission line for waveguides inscribed in LAK-14. The lowest insertion loss waveguides are highlighted in green.

None of the waveguides inscribed in LAK-14 were of a sufficiently low loss for development into evanescent, SWNT polymer composite coated, saturable absorbers. Investigation of a greater parameter space is necessary to reduce the losses of waveguides in this substrate.

7.4. Conclusions and scope for further work

ULI may be applicable to the fabrication of guided mode structures that can be integrated into saturable absorbers. Multiple different schemes exist which may provide benefits over the sandwiched patchcord device described in Section 6.2.2. The slotted waveguide device, which closely emulates the sandwiched patchcord, showed saturation of absorption under illumination from a moderate pulse energy modelocked Er fibre laser. This device provides the advantage of tailoring the mode field diameter at the waveguide to SWNT polymer interface, through a longitudinal tapering of the waveguide. This can be achieved by either changing pulse energy, translation speed, or

mulitscan separation. This, coupled with the ability to vary the width of the slot, could make this sufficiently useful to justify the processing time (waveguide inscription, selective etching, grinding, polishing and alignment). The other possible use of this design would be for speciality fibres, which do not splice to SMF-28 (either due to losses from mode mismatch or difficulties in alignment due to microstructures e.g. air holes). This class of device could be integrated into an oscillator based on a large mode area active fibre to allow for higher pulse energies.

While no proof of principal demonstration of the evanescent device is reported here, it is predicted that sufficient inscription parameter investigation for the two glasses and potentially increasing the number of glasses, with refractive indices close to 1.65 investigated, is likely to result in a functioning device. Saturable absorbers relying on the interaction of the evanescent field of the guided mode have several advantages over the more conventional devices. One advantage is that the pump may not have to be separated from the signal with a WDM, because the mode field diameter of the pump mode will be substantially smaller, resulting in less energy overlapping the SWNT composite region. Another advantage is that the three parameters: saturation fluence, modulation depth and nonsaturable loss, can all be relatively independently tailored by varying the distance between the waveguide and the surface, the length of the interaction section, the concentration of SWNTs in the polymer and the thickness of the polymer layer. This should allow for saturable absorbers to be optimised for a large range of fibre oscillators, from high repetition rates at multiple GHz to ultralow repetition rate of 100s kHz. The cladding written structure could be one attractive route towards this, by changing the position of the cladding scans along the length of the waveguide, the mode can be brought into overlap with the SWNTs for the required distance.

In this chapter we have identified methods of integrating SWNTs into ULI waveguides for modelocking compact ultrafast lasers. In Chapter 8 we will look at a method of increasing the power available from these devices, while preserving their performance. This will involve exploiting the strong linear dispersion within the erbium doped bismuthate waveguide amplifier presented in Chapter 5 and Chapter 6, in combination with the waveguide's high gain for the amplification of short pulses.

Chapter 8. The use of erbium doped waveguide amplifiers for ultrafast pulse amplification

8.1. Introduction

In Chapter 6 a modelocked laser featuring a ULI gain element was presented. Chapter 7 shows investigations into methods of integrating one of the fibre elements from this, the SWNT modelocker, into ULI compatible technology. In this chapter the applicability of the Er doped bismuthate to the amplification of short pulses is investigated, to allow for power scaling of the outputs from ultrafast ULI oscillators. Numerical modelling is performed using Matlab® to establish the feasibility of using the Er doped bismuthate glass waveguide presented in Chapter 5 and Chapter 6 for the parabolic pulse amplification of short pulses. A regime is identified in which this gain medium can be used to achieve significant amplification and a decrease in pulse duration of nearly a factor of 10 from input pulse to linearly compressed output pulse is shown.

As detailed in Chapter 6, several different designs exist for ultrafast fibre laser oscillators. Ultimately, the pulse energy is limited by the degree of nonlinear phase shift within a cavity round trip. This is dependent on the pulse energy, the pulse duration and the mode size. Increasing the mode size while maintaining single mode performance leads to low numerical apertures. Thus large bend radii are required for acceptable losses and the fibres used for high energy pulse amplification are often rods that cannot be bent. For scaling to higher pulse energies, a master oscillator power amplifier (MOPA) architecture is often employed; this has the advantage of allowing for greater nonlinear phase shifts while still remaining stable. Further reductions in the nonlinear phase shift can then be achieved by increasing the pulse duration by chirping the pulse, amplifying and then recompressing - this is known as chirped pulse amplification (CPA). CPA is commonly employed in solid state lasers, where the distance the light travels through the gain medium is small and therefore the dispersion experienced by the pulse is also small. In guided mode configurations the propagation distance can be much greater, allowing a different amplification technique to be exploited, parabolic pulse amplification, although fibre CPA is still used extensively.

Parabolic pulse amplification relies on using nonlinearity to shape the pulse as it propagates through a normally dispersive gain medium. As the pulse propagates it

experiences dispersion, thus becoming chirped, however the pulse also experiences amplification and spectral broadening from the gain medium. This can, under the correct conditions, lead to the pulse acquiring a parabolic temporal profile. After amplification, the linear chirp on the pulse can be compensated for by a grating pair, or pair of prisms. Due to the spectral broadening it is possible, under the correct conditions, to compress the output pulse to a duration shorter than the bandwidth limit of the input pulse.

The Er doped bismuthate waveguide used as the gain element for the work presented in Chapter 5 and Chapter 6, has some interesting properties, both linear and nonlinear, which are attractive for parabolic pulse amplification. The strong linear dispersion of the bismuthate glass, coupled to the high gain per unit length, should allow for high gain, short pulse parabolic amplification within shorter lengths than are permitted with conventional fibre. This is important for high pulse energy work where the large mode field diameters required lead to a large, inflexible length of gain medium being used.

In the next section the basis for a model of the parabolic pulse amplification of short pulses in the Er doped bismuthate glass waveguide is detailed. The results for the simulation of the waveguide detailed in Chapter 5 and Chapter 6 are then presented, identifying a regime in which this gain medium can be used to achieve significant amplification.

8.2. The model

Short pulse propagation in optical fibres can be well explained using the generalised nonlinear Schrödinger equation [107]

$$i\frac{\partial A}{\partial z} + \frac{i\alpha}{2}A - \frac{\beta_2}{2}\frac{\partial^2 A}{\partial T^2} + \gamma|A|^2 A = 0 \qquad (12)$$

where A is the slowly varying pulse envelope, α is the propagation loss of the field, β is the group velocity dispersion, γ represents the nonlinearity, z is distance and T is time.

For amplification, the second term of this equation, which represents a loss, can have its sign changed to represent a gain (g). This gain is in general a function of optical frequency.

$$i\frac{\partial A}{\partial z} - \frac{ig}{2}A - \frac{\beta_2}{2}\frac{\partial^2 A}{\partial T^2} + \gamma|A|^2 A = 0 \qquad (13)$$

This equation can then be rearranged into the form of

$$i\frac{\partial A}{\partial z} = \left(\hat{D} + \hat{N}\right)A \qquad (14)$$

where *D* is a differential operator that accounts for the dispersion and gain within the fibre and *N* is a nonlinear operator which governs the effect of the fibre nonlinearity on the pulse propagation.

The dispersion, gain and nonlinearity act together along the length of the fibre to govern the propagation of a pulse and this equation is, in general, not analytically solvable. The split-step Fourier technique approximates this problem by splitting the fibre into small sections and assuming that over a small distance the dispersive (and gain) effects can be considered to act independently of the nonlinear effects, and vice versa.

The code provided by Professor Dudley at SUSSP 66 was adapted to include the gain term from equation (13) and tested for accuracy by comparison with the results described in [114]. This paper models results using a simplified, spectrally flat gain function. The results published in [114] are shown in Figure 8.1, and bare strong resemblance to those acquired from this model, shown in Figure 8.2, confirming the validity of the model.

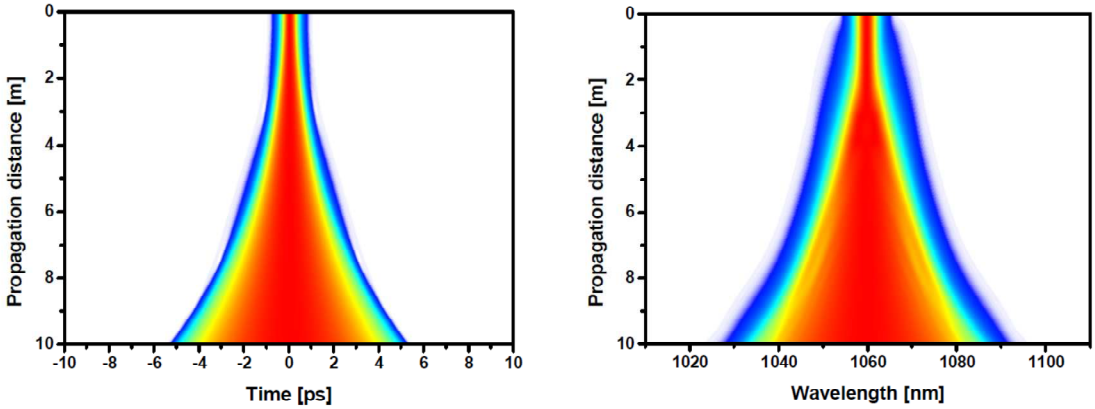

Figure 8.1. Results of a simulation of parabolic pulse amplification within a large mode area Yb doped optical fibre by Limpert et al. Figure taken from [114].

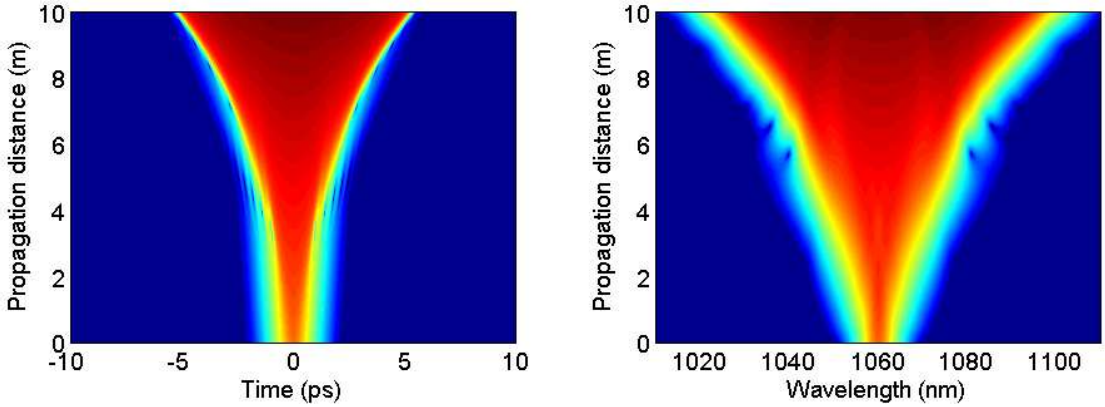

Figure 8.2. Results of the simulation using data from Limpert et al. [114]. Figure calculated using a code distributed by Professor Dudley at SUSSP66, modified to incorporate gain.

8.3. Modelling the erbium doped bismuthate waveguide amplifier

An estimate for the nonlinearity of the waveguide (gamma in equation (13)) was made based on the n_2 of the material, provided by the Asahi Glass Company, and the measured mode field diameter. The group velocity dispersion was also provided by the Asahi Glass Company. The spectrum of the gain was simplified by assuming it to be parabolic in frequency space. The measured and simulated gain spectra are shown in

Figure 8.3. For seeding the amplifier, a 500 fs bandwidth limited $sech^2$ pulse was chosen. For a pulse energy of 1 nJ the performance from two passes of the amplifier is shown in Figure 8.4. Spectral broadening of the pulse occurs beyond the spectral width of the modelled gain.

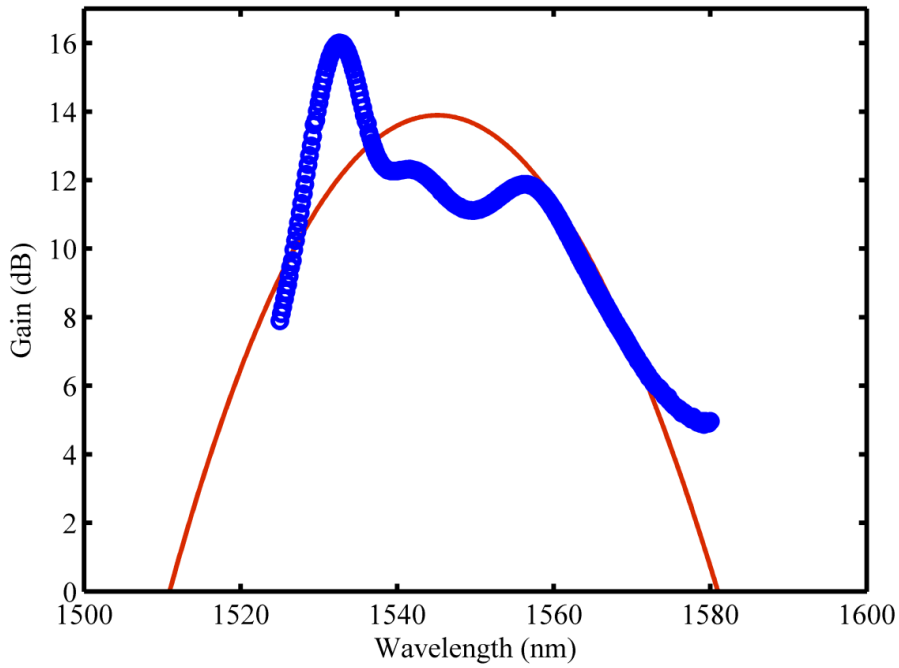

Figure 8.3. The small signal gain of the erbium doped bismuthate waveguide. Blue circles show the experimentally measured gain values at different wavelengths and the red line shows a simplified gain spectrum used for the model.

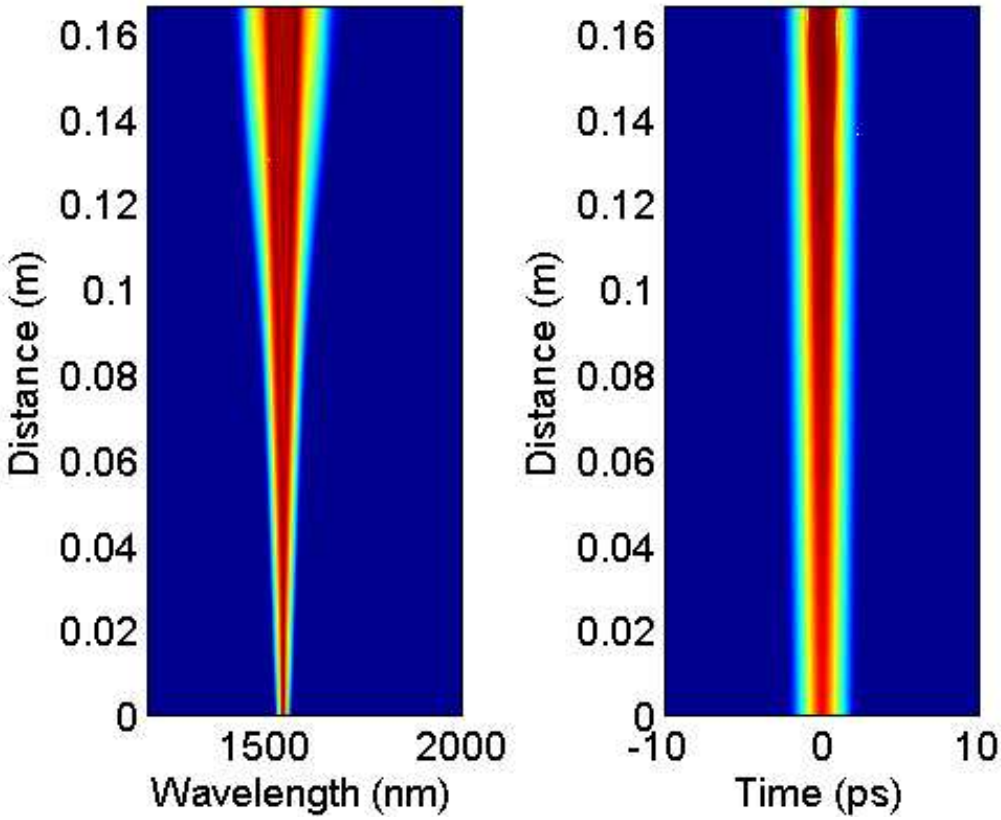

Figure 8.4. A simulation of pulse amplification in the erbium doped bismuthate glass waveguide amplifier. The seed pulse is a bandwidth limited 500 fs, 1 nJ pulse centred at 1550 nm.

8.4. Results

Under these conditions spectral broadening of the pulse occurs in the waveguide, but no pulse break up is observed. Figure 8.5. presents the temporal profile of the pulse at the end of the waveguide, and the same pulse once it has had the linear dispersion compensated for. As can be seen from the recompressed pulse, a 10 fold decrease in pulse duration has occurred between the seed pulse and the compressed amplified pulse. The peak power has increased from 2 kW for the seed pulse to over 100 kW. Similar behaviour could be attained for higher pulse energies by increasing the mode size and thus decreasing the nonlinearity of the waveguide.

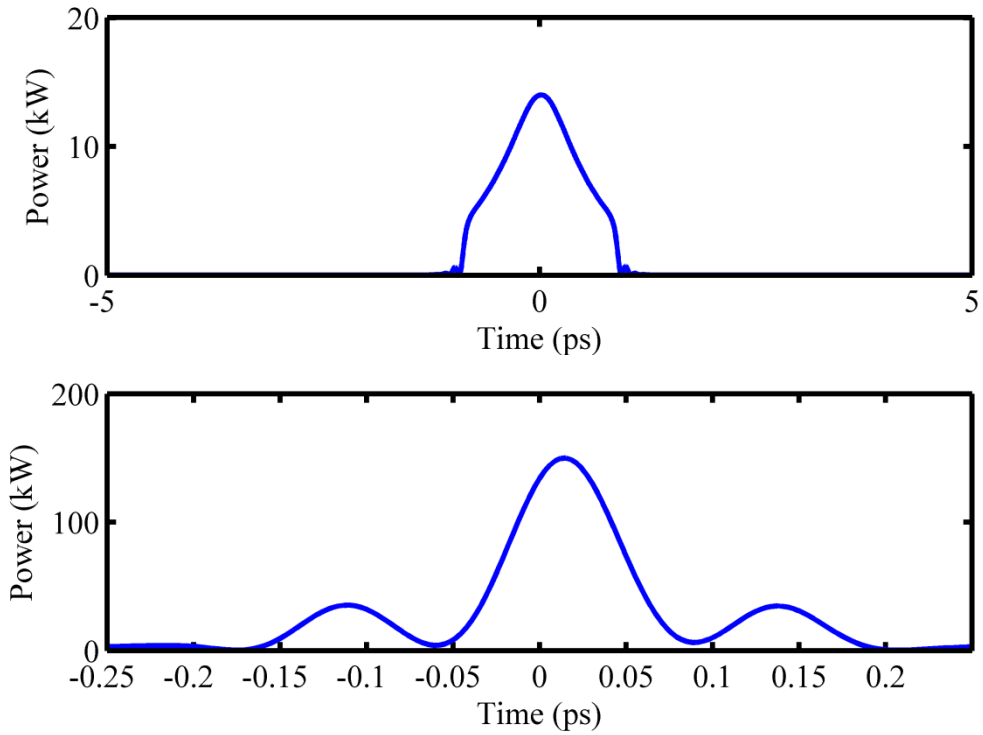

Figure 8.5. The temporal profile of the pulse. Top: the pulse emerging from the waveguide. Bottom: the pulse emerging from the waveguide after -0.0187 ps^2 of 2nd order dispersion (linear chirp).

8.5. Conclusions

This amplification scheme could be an attractive alternative to fibre CPA for the production of pulse energies in the 10's of nJ range for mode sizes similar to SMF-28 and up to 1 μJ for mode sizes of 50 μm. The high gain per unit length of the waveguide, in addition to the strong chromatic dispersion, make it an ideal choice for high gain parabolic pulse amplification within a short length. This short length is of importance for large mode sizes, as with the low NAs necessary for single mode performance even slight bends can result in significant losses. This limits low NA fibre technology to large footprint devices. In contrast, the footprint of a device utilising this waveguide could be extremely small. It is hoped that this simulation will be experimentally verified.

In this chapter I have presented a model demonstrating the potential application of ULI waveguides to parabolic pulse amplification. This could be used to amplify pulses from modelocked ULI waveguide lasers, such as that investigated in Chapter 6, or modelocked fibre lasers. In Chapter 9 conclusions will be drawn from the results presented in this thesis and further work increasing the versatility of ULI will be considered.

Chapter 9. Conclusions and further work

9.1. Conclusions

The work reported in this thesis has focussed on three distinct applications and presents work in a range of different materials, from amorphous glass to a highly ordered single crystal. Chapter 3 presents work on two different sensors inscribed into different substrates. Chapter 4 presents work within the nonlinear crystal monoclinic bismuth borate. Chapters 5 and 6 report upon the continuous wave and modelocked operation of an erbium doped bismuthate glass waveguide laser, while Chapter 7 presents initial attempts to integrate a saturable absorber with ULI technology, enabling modelocking in a compact system. The following provides a summary of the work presented in each chapter.

Chapter 3: Two classes of fibre sensor are replicated by ULI. A side-polished fibre-like waveguide is demonstrated. This waveguide is fabricated in a single step and shows a significant reduction in transmission when a high index oil is placed on the substrate surface. This shows potential for evanescent sensing applications. A Bragg grating array is fabricated in a flat fibre. This device features a 3x3 Y-splitter allowing a single fibre input to interrogate three waveguide Bragg gratings. The gratings are arranged in a triangular orientation permitting athermal directional strain sensing via analysis of the spectrum reflected by the device.

Chapter 4: Waveguides are inscribed in the nonlinear crystal monoclinic bismuth borate. A novel inscription geometry is employed to increase the mode overlap of OLP modes. The waveguide design features four damage lines arranged as two pairs. Each pair of damage line has the ability to independently control one of the linear polarisations guided by the device. By control of the relative positions of the two pairs of damage lines, mode overlap between the two OLP modes is improved. Type I phase matched SHG is demonstrated in the waveguide using this OLP mode control and modelling of the nonlinear interaction is carried out.

Chapter 5: A ULI erbium doped bismuthate glass waveguide is built into a fibre travelling wave cavity for use as a laser. Rigrod analysis is employed to extract information about the waveguide's properties. For a pump power of 1050 mW, an output power of 95 mW is reached. An optical to optical efficiency of 9% is

demonstrated. The efficiency of this device could be substantially improved by decreasing the high cavity losses.

Chapter 6: The erbium doped bismuthate glass laser from the previous chapter is adapted to include an SWNT saturable absorber. This saturable absorber initiates and stabilizes CW modelocking of the system. The laser is run with an anomalous net cavity dispersion allowing for soliton shaping of the intracavity pulse. This laser produces near bandwidth limited pulses of 320 fs duration at 1560 nm.

Chapter 7: An investigation into the integration of the SWNT saturable absorber with ULI devices is undertaken. Two geometries are explored: a slotted waveguide featuring a channel full of SWNT polymer and a side-polished fibre-like waveguide aiming to exploit an evanescent interaction between the guided mode and the SWNT polymer. Nonlinear characterisation of the slotted waveguide shows saturable absorption occurring, but the device could not initiate the modelocking of a fibre laser. The evanescent device requires further optimisation to reach the required specifications.

Chapter 8: Modelling is performed to establish the potential of using the erbium doped bismuthate glass waveguide presented in Chapter 5 and Chapter 6 as an amplifier for ultrafast pulses. The strong normal dispersion and high gain per unit length permit high gain parabolic pulse amplification in shorter lengths than is achievable with conventional fibre technology.

9.2. Further work

The side-polished fibre-like sensor developed in chapter 3 was demonstrated with the guided mode becoming a leaky mode when a thick high index layer was placed onto the substrate surface. This permitted the presence of the liquid to be measured based on the transmission of the device. For sensing of the refractive index of the overlay, a few simple changes could be made to the device. The first would be to inscribe a Bragg grating section into the side-polished-like section of the waveguide, a change in the refractive index of the overlay would result in a change to the effective index of the mode and therefore a shift of the reflection peak of the grating. The other possible change would be to place the side-polished-like section in one arm of a Mach-Zehnder interferometer. This could be constructed with either 2 Y-splitters or directional couplers. A change in the refractive index of the overlay would then result in a shift in

the interference fringes observed at the output. Since this geometry is well suited to thin film processing, functionalisation of the top of the device should be trivial, e.g. coating with palladium for hydrogen sensing. A 1D array of these elements could be written in a single substrate, interrogated by a single source, to give spatially resolved measurements. This design of device could also be used as a saturable absorber by coating the surface with SWNTs, as was attempted in Chapter 7.

The Bragg grating array showed the possibility of working in substrates differing from the planar substrates normally employed for ULI. The potential to integrate ULI with UV writing is of promise, as most of the fabrication equipment, other than the laser, is identical. It could be that ULI would be used for modifying material to be removed by selective etching, or for writing waveguides which move out of the plane to which UV writing is inherently limited. ULI of waveguides has since been demonstrated in conventional single mode fibre [115], this opens many new avenues for ULI with the potential to modify existing fibre devices from their 1D properties to 3D.

The waveguides in BiBO were, in their current form, of little use for SHG. While further optimisation of parameters would lead to substantially better waveguides, it is my strong belief that efficient SHG in this wavelength range is more easily and consistently achieved in PPLN, either with type I or conventional type II waveguides. For wavelengths outside of the transparency range of PPLN other crystals, which may not be quasi-phase matched, may have to be used, for example BBO for blue/UV. For these birefringently phase matched materials this four damage line approach may have to be used. I consider the more significant result from this work to be the ability to demonstrate independent control of the linear polarisations in ULI waveguides. If the losses can be reduced sufficiently then devices based on this work could be an enabling technology for quantum information processing [116].

The erbium doped bismuthate substrate shows great promise for CW lasers, amplifiers and pulsed laser and amplifier applications. The optical to optical efficiencies quoted in the CW work could be vastly improved by moving to a different cavity design. The amplifier characteristics (both linear and nonlinear) could be tailored by changing mode size throughout the device. Ultimately ULI can compete favourably with other technologies anywhere where a longitudinal change in the waveguide properties is required. Be this for DBR lasers, tapered waveguide amplifiers or single chip passively q-switched master oscillator power amplifier devices featuring a Bragg grating output

coupler. Another interesting use of this waveguide would be as the gain element in an NPE fibre laser cavity. There is strong anecdotal evidence of a length law between the length of the fibre oscillator and the pulse durations attainable from the oscillator [117]. If this is the case, the erbium doped bismuthate glass waveguide could be capable of taking the record for the shortest pulses generated by a guided mode erbium doped laser.

The work on the integration of SWNTs with ULI technology requires more time to develop usable devices. Ultimately, for high repetition rate modelocked oscillators, I consider this to be the wrong design to use and standing wave cavities, featuring fewer components, are far more favourable for this application. SWNT integration into this geometry could easily be accomplished, for example by coating the output coupler with SWNTs. The modelocker designs presented do however have merit, but must exploit the strengths of ULI. The slotted waveguide design could be used to fulfil the role of the connectorised SWNT device for fibres not readily available pigtailed, for example large mode area fibre. The evanescent device is potentially of great use for its ability to independently tailor the SWNT modelocker's properties, saturation fluence and modulation depth, over a large range. This makes it an attractive prospect for a range of fibre laser designs, perhaps most importantly low repetition rate oscillators, with their high pulse energies.

The modelling performed on pulse amplification in the erbium doped bismuthate waveguide should be tested experimentally to establish the feasibility of power scaling the output from ULI waveguide lasers in this manner. This will hopefully allow for simple, integrated sources producing short pulses of 10's of nJ at high repetition rates.

After 15 years, ULI is still finding new applications, increasing the versatility of substrates that can be processed and the complexity of the devices that can be fabricated. It is only now that it is starting to be more than a research curiosity. In the last few years two companies have been founded, commercialising products fabricated by ULI [118, 119]. As inscription lasers become more affordable this trend is set to continue, hopefully leading to the use of ULI devices in a range of scientific fields from photonics, where they started, through to microfluidics in biology.

Appendix A. The applicability of Rigrod type laser analysis to waveguide lasers.

A.1. Introduction

The Rigrod analysis of laser oscillators with large output coupling makes several assumptions about the system. It assumes a homogenously saturable gain medium, with no distributed losses. In a standing wave cavity it is assumed that the intensity of both of the counter propagating waves contribute to the saturation of the gain at any position within the cavity, for the travelling wave treatment only the intensity in one direction must be taken into account. The following model is based on the standing wave case, primarily because the derivation of Rigrod analysis for this case is well described in Lasers by Seigman [120], a book most of the readers of this thesis will have access to, while the travelling wave case is often badly explained. Primarily we will investigate how Rigrod analysis behaves when one of the major assumptions, no distributed loss, is not met. This is often the case for waveguide lasers, where distributed losses along the waveguide make up a substantial part of the total losses of the system.

A.2. The model

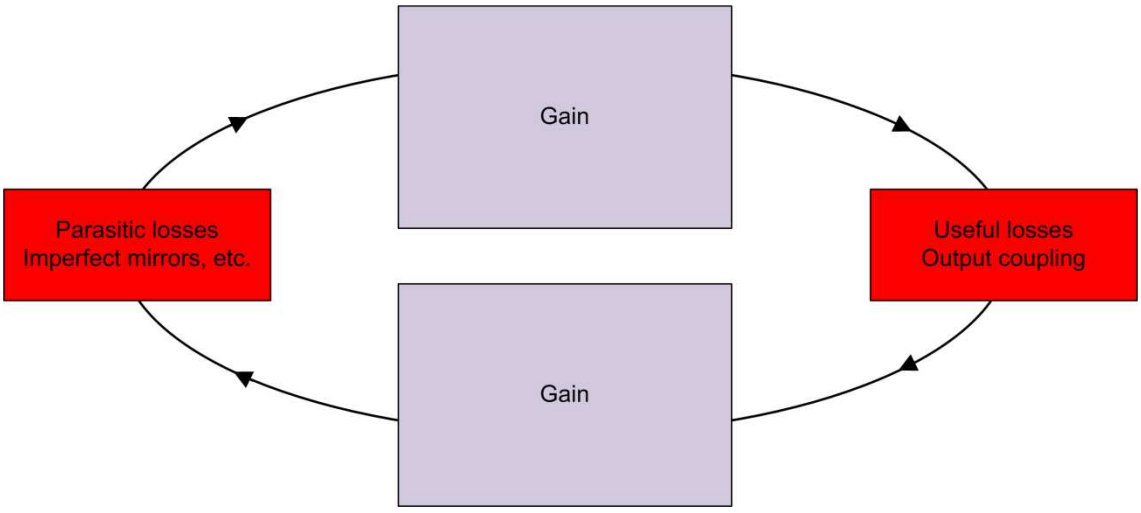

Figure A.1. Concept of Rigrod analysis, the intracavity circulating intensity sees the gain medium, the lumped cavity parasitic losses, the gain medium again and then the output coupler. Saturation of the gain is contributed to by the intensity from both propagation directions.

The variables within Rigrod analysis are small signal gain, Gss, Saturation intensity, Isat, and parasitic losses, Loss. Gss is the single pass gain experienced by an infinitely

small signal, Isat is the intensity at which the gain drops to Gss/e, Loss is the total loss of the system, excluding the output coupler. A Matlab® model was made to simulate a waveguide laser, see figure A.2. for the concept. A value was input into the loop to represent an average intracavity power. Based on the given values of Gss and Isat, the amount of gain for a small step through the gain medium was calculated and the new power was input into the next step through the gain medium. The power at each point in the cavity was kept in a look up table so the sum of both the forward propagating and counter propagating power could be used for any position in the cavity. When the end of the gain medium was reached, output coupling occurred and this value was stored for later comparison. The power then started counter propagating through the gain medium until it reached the discrete loss section, when the discrete loss was applied. The power then started forward propagating again.

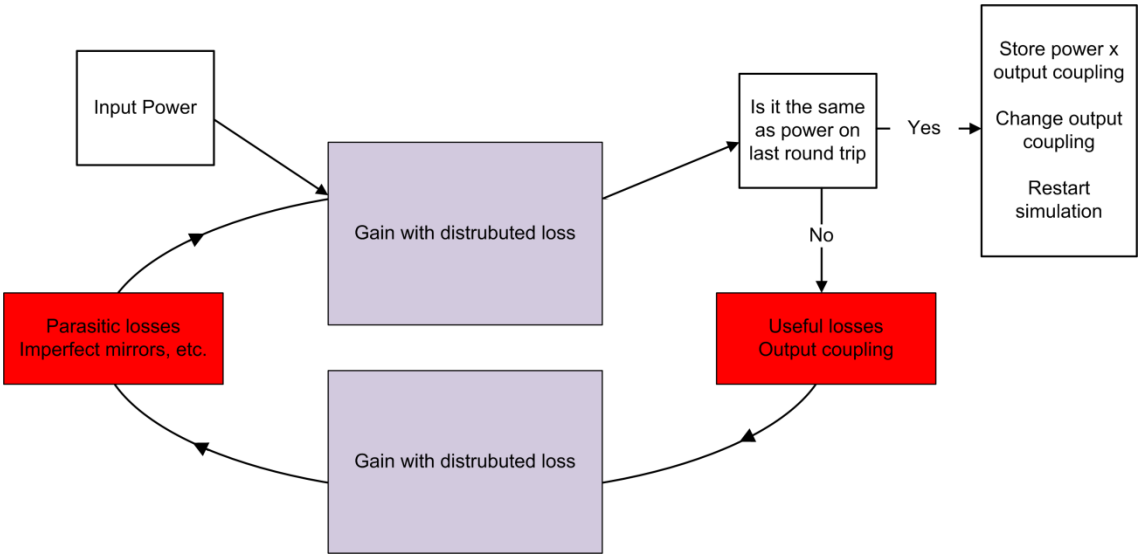

Figure A.2. Concept of the Matlab® program used to investigate the effect of distributed losses within the gain medium and how this affects Rigrod analysis. The power stored is the power which would come through the output coupler.

The program ran until it reached stability (less than 0.001 relative variation from round trip to round trip) and then the output coupling was changed and the program was repeated. The resultant output coupling curve was fitted to with a conventional standing wave Rigrod analysis. The expectation was that for no distributed losses the fitting would be perfect and the Rigrod analysis would yield the correct values for Gss, Isat and Loss. For cases with distributed losses built into the steps through the gain medium it was expected to underestimate both Gss and Isat.

A.3. Results with no distributed losses

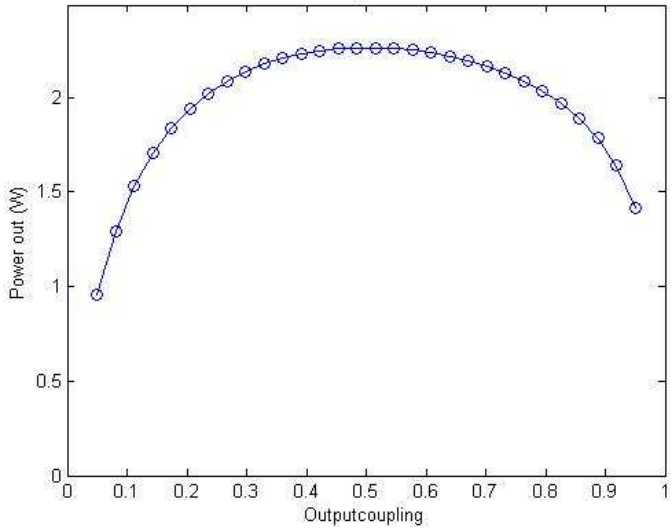

Figure A.3. A comparison between the simulation and Rigrod analysis for no distributed losses. Dots are the values calculated by the stepwise simulation and the line is the analytical solution for the same values of Gss, Isat and Loss. Perfect agreement is found. Small signal gain is 3 per pass, Isat is set to unity and the reflectivity of the nonoutput coupler mirror is set to 0.9 (ie Loss = 0.1).

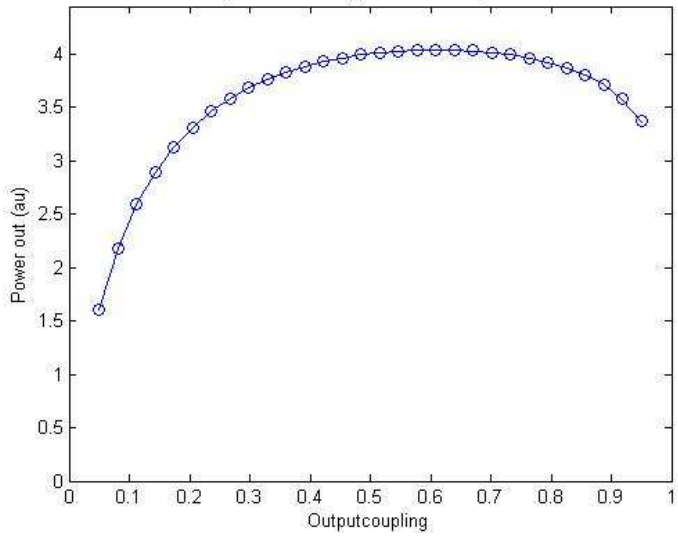

Figure A.4. A comparison between the simulation and Rigrod analysis for no distributed losses. Dots are the values calculated by the stepwise simulation and the line is the analytical solution for the same values of Gss, Isat and Loss. Perfect agreement is found. Small signal gain is 5 per pass, Isat is set to unity and the reflectivity of the nonoutput coupler mirror is set to 0.9 (ie Loss = 0.1).

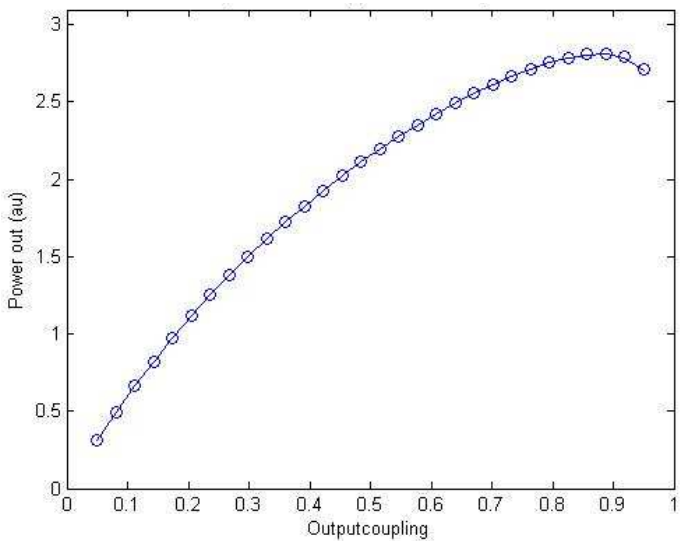

Figure A.5. A comparison between the simulation and Rigrod analysis for no distributed losses. Dots are the values calculated by the stepwise simulation and the line is the analytical solution for the same values of Gss, Isat and Loss. Perfect agreement is found. Small signal gain is 5 per pass, Isat is set to unity and the reflectivity of the nonoutput coupler mirror is set to 0.5 (ie Loss = 0.1).

The simulation was deemed to work well for a wide range of gains and discrete losses, so distributed loss was added to the system.

A.4. Results with distributed losses

The same simulation was used but a small propagation loss was included in each step through the gain medium, obviously the line calculated from the analytical solution would no longer fit since this has no scope for distributed loss. Rigrod analysis is commonly used to extract useful information about the laser cavity from experimental results, so the simulation was fitted to as if the data were from a real experiment. For this part, fitting was performed in Origin because more user control of the fitting is readily attainable than using the 'fminsearch' command in Matlab®. Figure A.6. presents the results for a Gss of 3, an Isat of unity and discrete losses of 0.1 for different values of propagation loss. The propagation losses are from top to bottom, 0, 0.1, 1, and 3dB for the Black, Red, Blue and Pink o's respectively. The Olive line shows the analytical solution for a Gss of 3, Isat of unity and discrete loss of 0.1. The Black, Red, Blue and Pink line are best fits to the data sets allowing Gss, Isat and Loss to vary.

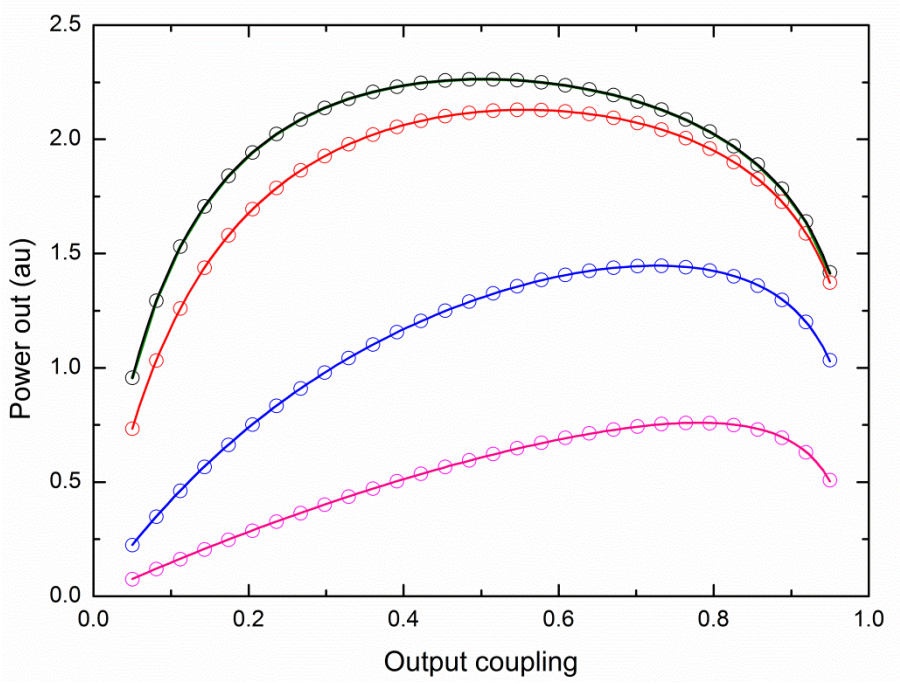

Figure A.6. The effect of distributed losses. All plotted data points have a Gss of 3, an Isat of 1 and a discrete loss of 0.1. Propagation losses of 0 dB, 0.1 dB, 1 dB and 3 dB per pass are plotted. These data are then fitted to using a Rigrod analysis, shown as lines.

A.5. Conclusions

The fitting line still fits well in these cases due to the 3 degrees of freedom in the fitting function, however the values yielded deviate from the real values for large propagation losses.

Propagation loss, dB, for simulation	Isat, from Rigrod analysis	Loss, from Rigrod analysis	Gss, from Rigrod analysis
0	1	0.1	3
0.1	1.00	0.14	2.992
1	1.02	0.42	2.916
3	0.973	0.72	2.824

We will concentrate primarily on loss, as Rigrod analysis is often used as an alternative to an independent measurement of loss for waveguides in gain media.

Propagation loss, dB, for simulation	Real total loss per round trip (discrete + 2x prop loss), linear	Predicted loss, linear, from Rigrod	Difference (Real – Rigrod fit), linear	Difference (Real – Rigrod fit), dB
0	0.1	0.1	0	0
0.1	0.141	0.140	0.000377	0.00164
1	0.432	0.421	0.010598	0.04627
3	0.774	0.723	0.05095	0.2271

As the propagation losses increase, the value gained by Rigrod analysis starts to underestimate the losses of the system.

The same simulation was carried out for a highly reflective mirror at the nonoutput side of the waveguide (99% reflective).

Propagation loss, dB, for simulation	Real total loss per round trip (discrete + 2x prop loss), linear	Predicted loss, linear, from Rigrod	Difference (Real – Rigrod fit), linear	Difference (Real – Rigrod fit), dB
0	0.01	0.01	0	0
0.1	0.054557	0.5439	0.000167	0.000727
1	0.375352	0.36617	0.009182	0.040062
3	0.751323	0.70058	0.050743	0.226163

We can see Rigrod consistently under predicts losses but only by a small amount, probably not of great significance for the majority of studies where this analysis is used.

References

1. G. Goubau and F. Schwering, "On the guided propagation of electromagnetic wave beams," IRE Trans. Antennas and Propag. **9**, 248-256 (1961).
2. E. Marcatili and R. Schmeltzer, "Hollow metallic and dielectric waveguides for long distance optical transmission and lasers(Long distance optical transmission in hollow dielectric and metal circular waveguides, examining normal mode propagation)," Bell System Technical Journal **43**, 1783-1809 (1964).
3. C. K. Kao, "The Nobel Prize in Physics 2009: For groundbreaking achievements concerning the transmission of light in fibers for optical communication" (2009), retrieved 28/03/2012, http://www.nobelprize.org/nobel_prizes/physics/laureates/2009/.
4. A. Yariv and R. C. C. Leite, "Dielectric-waveguide mode of light propagation in p-n junctions," Appl. Phys. Lett. **2**, 55-57 (1963).
5. W. L. Bond, B. G. Cohen, R. C. C. Leite, and A. Yariv, "Observation of the dielectric-waveguide mode of light propagation in p-n junctions," Appl. Phys. Lett. **2**, 57-59 (1963).
6. R. Kashyap, *Fibre Bragg Gratings* (Academic Press, London, 1999).
7. V. Vali and R. W. Shorthill, "Fiber ring interferometer," Appl. Opt. **15**, 1099-1100 (1976).
8. E. Snitzer, "Optical Maser Action of Nd^{3+} in a Barium Crown Glass," Phys. Rev. Lett. **7**, 444-446 (1961).
9. Y. Jeong, J. Sahu, D. Payne, and J. Nilsson, "Ytterbium-doped large-core fiber laser with 1.36 kW continuous-wave output power," Opt. Express **12**, 6088-6092 (2004).
10. B. He, Q. Lou, J. Zhou, J. Dong, Y. Wei, D. Xue, Y. Qi, Z. Su, L. Li, and F. Zhang, "High power coherent beam combination from two fiber lasers," Opt. Express **14**, 2721-2726 (2006).
11. J. C. Knight, T. A. Birks, P. S. J. Russell, and D. M. Atkin, "All-silica single-mode optical fiber with photonic crystal cladding," Opt. Lett. **21**, 1547-1549 (1996).
12. K. M. Davis, K. Miura, N. Sugimoto, and K. Hirao, "Writing waveguides in glass with a femtosecond laser," Opt. Lett. **21**, 1729-1731 (1996).
13. R. Osellame, N. Chiodo, G. Valle, S. Taccheo, R. Ramponi, G. Cerullo, A. Killi, U. Morgner, M. Lederer, and D. Kopf, "Optical waveguide writing with a diode-pumped femtosecond oscillator," Opt. Lett. **29**, 1900-1902 (2004).
14. L. Shah, A. Arai, S. Eaton, and P. Herman, "Waveguide writing in fused silica with a femtosecond fiber laser at 522 nm and 1 MHz repetition rate," Opt. Express **13**, 1999-2006 (2005).
15. C. B. Schaffer, A. Brodeur, J. F. García, and E. Mazur, "Micromachining bulk glass by use of femtosecond laser pulses with nanojoule energy," Opt. Lett. **26**, 93-95 (2001).
16. G. R. Fowles, "Ch 6. Optics of solids," in *Introduction to modern optics* (Dover Publications, 1989).
17. R. W. Boyd, "Ch 1. The nonlinear optical susceptibility," in *Nonlinear optics,* 2nd ed. (Academic Press, 2003).
18. P. A. Franken, A. E. Hill, C. W. Peters, and G. Weinreich, "Generation of Optical Harmonics," Phys. Rev. Lett. **7**, 118-119 (1961).
19. J. A. Armstrong, N. Bloembergen, J. Ducuing, and P. S. Pershan, "Interactions between Light Waves in a Nonlinear Dielectric," Phys. Rev. **127**, 1918-1939 (1962).
20. R. W. Boyd, "Ch 2. Wave-equation description of nonlinear optical interactions," in *Nonlinear optics,* 2nd ed. (Academic Press, 2003).
21. A. Yariv and P. Yeh, "Ch 5. Interaction of radiation and atomic systems," in *Photonics: optical electronics in modern communications* (Oxford University Press, 2006).
22. W. Kaiser and C. G. B. Garrett, "Two-Photon Excitation in CaF_2: Eu^{2+}," Phys. Rev. Lett. **7**, 229-231 (1961).

23. B. Amos, "Two photon absorption" (Science photo library), retrieved 27/03/2012, http://www.sciencephoto.com/set/916.
24. L. V. Keldysh, "Ionization In The Field of a Strong Electromagnetic Wave," Soviet Physics JEPT **20**, 1307-1314 (1965).
25. S. Nolte, C. Momma, H. Jacobs, A. Tünnermann, B. N. Chichkov, B. Wellegehausen, and H. Welling, "Ablation of metals by ultrashort laser pulses," J. Opt. Soc. Am. B **14**, 2716-2722 (1997).
26. E. N. Glezer and E. Mazur, "Ultrafast-laser driven micro-explosions in transparent materials," Appl. Phys. Lett. **71**, 882 (1997).
27. C. Hnatovsky, R. Taylor, P. Rajeev, E. Simova, V. Bhardwaj, D. Rayner, and P. Corkum, "Pulse duration dependence of femtosecond-laser-fabricated nanogratings in fused silica," Appl. Phys. Lett. **87**, 014104 (2005).
28. Y. Bellouard, A. Said, M. Dugan, and P. Bado, "Fabrication of high-aspect ratio, micro-fluidic channels and tunnels using femtosecond laser pulses and chemical etching," Opt. Express **12**, 2120-2129 (2004).
29. A. Marcinkevičius, S. Juodkazis, M. Watanabe, M. Miwa, S. Matsuo, H. Misawa, and J. Nishii, "Femtosecond laser-assisted three-dimensional microfabrication in silica," Opt. Lett. **26**, 277-279 (2001).
30. A. Crespi, Y. Gu, B. Ngamsom, H. J. W. M. Hoekstra, C. Dongre, M. Pollnau, R. Ramponi, H. H. van den Vlekkert, P. Watts, G. Cerullo, and R. Osellame, "Three-dimensional Mach-Zehnder interferometer in a microfluidic chip for spatially-resolved label-free detection," Lab Chip **10**, 1167-1173 (2010).
31. D. Choudhury, W. T. Ramsay, R. Kiss, N. A. Willoughby, L. Paterson, and A. K. Kar, "A 3D mammalian cell separator biochip," Lab Chip **12**, 948-953 (2012).
32. R. R. Thomson, H. T. Bookey, N. D. Psaila, A. Fender, S. Campbell, W. N. MacPherson, J. S. Barton, D. T. Reid, and A. K. Kar, "Ultrafast-laser inscription of a three dimensional fan-out device for multicore fiber coupling applications," Opt. Express **15**, 11691-11697 (2007).
33. J. Burghoff, C. Grebing, S. Nolte, and A. Tuennermann, "Efficient frequency doubling in femtosecond laser-written waveguides in lithium niobate," Appl. Phys. Lett. **89**, 081108 (2006).
34. W. Yang, P. G. Kazansky, and Y. P. Svirko, "Non-reciprocal ultrafast laser writing," Nat. Photonics **2**, 99-104 (2008).
35. J. R. Macdonald, R. R. Thomson, S. J. Beecher, N. D. Psaila, H. T. Bookey, and A. K. Kar, "Ultrafast laser inscription of near-infrared waveguides in polycrystalline ZnSe," Opt. Lett. **35**, 4036-4038 (2010).
36. T. Nagata, M. Kamata, and M. Obara, "Optical waveguide fabrication with double pulse femtosecond lasers," Appl. Phys. Lett. **86**, 251103 (2005).
37. S. M. Eaton, H. Zhang, M. L. Ng, J. Li, W.-J. Chen, S. Ho, and P. R. Herman, "Transition from thermal diffusion to heat accumulation in high repetition rate femtosecond laser writing of buried optical waveguides," Opt. Express **16**, 9443-9458 (2008).
38. N. D. Psaila, R. R. Thomson, H. T. Bookey, S. Shen, N. Chiodo, R. Osellame, G. Cerullo, A. Jha, and A. K. Kar, "Supercontinuum generation in an ultrafast laser inscribed chalcogenide glass waveguide," Opt. Express **15**, 15776-15781 (2007).
39. V. Kononenko, V. Pashinin, B. Galagan, S. Sverchkov, B. Denker, V. Konov, and E. Dianov, "Activation of color centers in bismuth glass by femtosecond laser radiation," Laser Phys. **21**, 1585-1592 (2011).
40. P. J. Lemaire, R. M. Atkins, V. Mizrahi, and W. A. Reed, "High-pressure H_2 loading as a technique for achieving ultrahigh UV photosensitivity and thermal sensitivity in GeO_2 doped optical fibers," Electron. Lett. **29**, 1191-1193 (1993).
41. X. Liu, D. Du, and G. Mourou, "Laser ablation and micromachining with ultrashort laser pulses," IEEE J. Quantum Electron. **33**, 1706-1716 (1997).

42. D. N. Vitek, D. E. Adams, A. Johnson, P. S. Tsai, S. Backus, C. G. Durfee, D. Kleinfeld, and J. A. Squier, "Temporally focused femtosecond laser pulses for low numerical aperture micromachining through optically transparent materials," Opt. Express **18**, 18086-18094 (2010).
43. S. Rajesh and Y. Bellouard, "Towards fast femtosecond laser micromachining of fused silica: The effect of deposited energy," Opt. Express **18**, 21490-21497 (2010).
44. S. M. Eaton, H. B. Zhang, and P. R. Herman, "Heat accumulation effects in femtosecond laser-written waveguides with variable repetition rate," Opt. Express **13**, 4708-4716 (2005).
45. A. Baum, S. De Nicola, S. Abdalah, K. Al-Naimee, A. Geltrude, M. Locatelli, R. Meucci, W. Perrie, P. J. Scully, A. Taranu, and F. T. Arecchi, "Optical characterization of PMMA phase gratings written by a 387 nm femtosecond laser," Opt. Commun. **284**, 2771-2774 (2011).
46. Y. Nasu, M. Kohtoku, and Y. Hibino, "Low-loss waveguides written with a femtosecond laser for flexible interconnection in a planar light-wave circuit," Opt. Lett. **30**, 723-725 (2005).
47. Mitutoyo, "Product information for LWD series microscope objectives, Optical_2" (2011), retrieved 14/03/2012, http://www.mitutoyo.co.jp/eng/products/gazoukogaku/Optical_2.pdf.
48. V. Zambon, N. McCarthy, and M. Piché, "Fabrication of photonic devices directly written in glass using ultrafast Bessel beams," in *Photonics North*, (SPIE, 2008), 709921-709925.
49. R. Osellame, S. Taccheo, M. Marangoni, R. Ramponi, P. Laporta, D. Polli, S. De Silvestri, and G. Cerullo, "Femtosecond writing of active optical waveguides with astigmatically shaped beams," J. Opt. Soc. Am. B: Opt. Phys. **20**, 1559-1567 (2003).
50. M. Ams, G. D. Marshall, D. J. Spence, and M. J. Withford, "Slit beam shaping method for femtosecond laser direct-write fabrication of symmetric waveguides in bulk glasses," Opt. Express **13**, 5676-5681 (2005).
51. R. R. Thomson, A. S. Bockelt, E. Ramsay, S. Beecher, A. H. Greenaway, A. K. Kar, and D. T. Reid, "Shaping ultrafast laser inscribed optical waveguides using a deformable mirror," Opt. Express **16**, 12786-12793 (2008).
52. S. Nolte, J. Burghoff, M. Will, and A. Tuennermann, "Femtosecond writing of high-quality waveguides inside phosphate glasses and crystalline media using a bifocal approach," in *Commercial and Biomedical Application of Ultrafast Lasers IV*, (SPIE, 2004), 164-171.
53. E. G. Coker and L. N. G. Filon, *A Treatise on Photo-elasticity* (University Press, 1957).
54. F. M. Bain, A. A. Lagatsky, R. R. Thomson, N. D. Psaila, N. V. Kuleshov, A. K. Kar, W. Sibbett, and C. T. A. Brown, "Ultrafast laser inscribed Yb:KGd$(WO_4)_2$ and Yb:KY$(WO_4)_2$ channel waveguide lasers," Opt. Express **17**, 22417-22422 (2009).
55. Y. Tan, A. Rodenas, F. Chen, R. R. Thomson, A. K. Kar, D. Jaque, and Q. Lu, "70% slope efficiency from an ultrafast laser-written Nd:$GdVO_4$ channel waveguide laser," Opt. Express **18**, 24994-24999 (2010).
56. J. Siebenmorgen, T. Calmano, K. Petermann, and G. Huber, "Highly efficient Yb:YAG channel waveguide laser written with a femtosecond-laser," Opt. Express **18**, 16035-16041 (2010).
57. R. Osellame, M. Lobino, N. Chiodo, M. Marangoni, G. Cerullo, R. Ramponi, H. T. Bookey, R. R. Thomson, N. D. Psaila, and A. K. Kar, "Femtosecond laser writing of waveguides in periodically poled lithium niobate preserving the nonlinear coefficient," Appl. Phys. Lett. **90**, 241107 (2007).
58. S. Campbell, R. R. Thomson, D. P. Hand, A. K. Kar, D. T. Reid, C. Canalias, V. Pasiskevicius, and F. Laurell, "Frequency-doubling in femtosecond laser inscribed periodically-poled potassium titanyl phosphate waveguides," Opt. Express **15**, 17146-17150 (2007).

59. H. T. Bookey, R. R. Thomson, N. D. Psaila, A. K. Kar, N. Chiodo, R. Osellame, and G. Cerullo, "Multi-scan femtosecond laser waveguide inscription in z-cut Lithium Niobate," in *CLEOPR*, (Optical Society of America, 2007), TuD2_2.
60. R. R. Thomson, N. D. Psaila, S. J. Beecher, and A. K. Kar, "Ultrafast laser inscription of a high-gain Er-doped bismuthate glass waveguide amplifier," Opt. Express **18**, 13212-13219 (2010).
61. A. Rodenas, G. A. Torchia, G. Lifante, E. Cantelar, J. Lamela, F. Jaque, L. Roso, and D. Jaque, "Refractive index change mechanisms in femtosecond laser written ceramic Nd:YAG waveguides: micro-spectroscopy experiments and beam propagation calculations," Appl. Phys. B-Lasers and Optics **95**, 85-96 (2009).
62. G. A. Torchia, A. Rodenas, A. Benayas, E. Cantelar, L. Roso, and D. Jaque, "Highly efficient laser action in femtosecond-written Nd : yttrium aluminum garnet ceramic waveguides," Appl. Phys. Lett. **92**, 111103 (2008).
63. R. R. Thomson, S. Campbell, I. J. Blewett, A. K. Kar, and D. T. Reid, "Optical waveguide fabrication in z-cut lithium niobate ($LiNbO_3$) using femtosecond pulses in the low repetition rate regime," Appl. Phys. Lett. **88**(2006).
64. Y. Bellouard, A. A. Said, and P. Bado, "Integrating optics and micro-mechanics in a single substrate: a step toward monolithic integration in fused silica," Opt. Express **13**, 6635-6644 (2005).
65. Y. Nasu, M. Kohtoku, Y. Hibino, and Y. Inoue, "Waveguide Interconnection in Silica-Based Planar Lightwave Circuit Using Femtosecond Laser," J. Lightwave Technol. **27**, 4033-4039 (2009).
66. Y. Bellouard, A. Said, and P. Bado, "Integrating optics and micro-mechanics in a single substrate: a step toward monolithic integration in fused silica," Opt. Express **13**, 6635-6644 (2005).
67. R. R. Thomson, T. A. Birks, S. G. Leon-Saval, A. K. Kar, and J. Bland-Hawthorn, "Ultrafast laser inscription of an integrated photonic lantern," Opt. Express **19**, 5698-5705 (2011).
68. B. Culshaw and A. Kersey, "Fiber-Optic Sensing: A Historical Perspective," J. Lightwave Technol. **26**, 1064-1078 (2008).
69. G. Meltz, W. W. Morey, and W. H. Glenn, "Formation of Bragg gratings in optical fibers by a transverse holographic method," Opt. Lett. **14**, 823-825 (1989).
70. E. Hecht, "Ch. 10. Diffraction," in *Optics,* 4th ed. (Addison Wesley, 2002).
71. N. Hirayama and Y. Sano, "Fiber Bragg grating temperature sensor for practical use," ISA Trans. **39**, 169-173 (2000).
72. A. Fender, W. N. MacPherson, R. R. J. Maier, J. S. Barton, D. S. George, R. I. Howden, G. W. Smith, B. J. S. Jones, S. McCulloch, X. Chen, R. Suo, L. Zhang, and I. Bennion, "Two-axis temperature-insensitive accelerometer based on multicore fiber Bragg gratings," IEEE Sens. J. **8**, 1292-1298 (2008).
73. V. Maselli, J. R. Grenier, S. Ho, and P. R. Herman, "Femtosecond laser written optofluidic sensor: Bragg grating waveguide evanescent probing of microfluidic channel," Opt. Express **17**, 11719-11729 (2009).
74. Corning, "SMF-28 Optical Fiber Product Information" (2011), retrieved 23/03/2012.
75. R. Sacher, Cargille Labs, New Jersey (personal communication, 2010).
76. S. M. Tseng and C. L. Chen, "Side-polished fibers," Appl. Opt. **31**, 3438-3447 (1992).
77. S. Beecher, R. Thomson, B. Pal, and A. Kar, "Single Stage Ultrafast Laser Inscription of a Side-Polished Fiber-like Waveguide Sensor," IEEE Sens. J. **PP**, 1-1 (2011).
78. Y.-W. Song, S. Yamashita, C. S. Goh, and S. Y. Set, "Carbon nanotube mode lockers with enhanced nonlinearity via evanescent field interaction in D-shaped fibers," Opt. Lett. **32**, 148-150 (2007).
79. G. D. Marshall, M. Ams, and M. J. Withford, "Direct laser written waveguide-Bragg gratings in bulk fused silica," Opt. Lett. **31**, 2690-2691 (2006).
80. H. Zhang, S. M. Eaton, J. Li, and P. R. Herman, "Femtosecond laser direct writing of multiwavelength Bragg grating waveguides in glass," Opt. Lett. **31**, 3495-3497 (2006).

81. H. Zhang, S. M. Eaton, and P. R. Herman, "Single-step writing of Bragg grating waveguides in fused silica with an externally modulated femtosecond fiber laser," Opt. Lett. **32**, 2559-2561 (2007).
82. A. S. Webb, E. M. Adikan, J. K. Sahu, R. J. Standish, C. B. E. Gawith, J. C. Gates, P. G. R. Smith, and D. N. Payne, "MCVD planar substrates for UV-written waveguide devices," Electron. Lett. **43**, 517-519 (2007).
83. C. Holmes, F. R. M. Adikan, A. S. Webb, J. C. Gates, C. B. E. Gawith, J. K. Sahu, P. G. R. Smith, D. N. Payne, and Ieee, "Evanescent Field Sensing in novel Flat Fiber," in *CLEO* (Optical Society of America, 2008), 570-571.
84. G. Brown, R. R. Thomson, A. K. Kar, N. D. Psaila, and H. T. Bookey, "Ultrafast laser inscription of Bragg-grating waveguides using the multiscan technique," Opt. Lett. **37**, 491-493 (2012).
85. K. Suzuki, V. Sharma, J. G. Fujimoto, E. P. Ippen, and Y. Nasu, "Characterization of symmetric [3 x 3] directional couplers fabricated by direct writing with a femtosecond laser oscillator," Opt. Express **14**, 2335-2343 (2006).
86. S. Nolte, M. Will, J. Burghoff, and A. Tuennermann, "Femtosecond waveguide writing: a new avenue to three-dimensional integrated optics," Appl. Phys. A: Materials Science & Processing **77**, 109-111 (2003).
87. M. Bache, H. Nielsen, J. Lægsgaard, and O. Bang, "Tuning quadratic nonlinear photonic crystal fibers for zero group-velocity mismatch," Opt. Lett. **31**, 1612-1614 (2006).
88. M. L. Bortz, L. A. Eyres, and M. M. Fejer, "Depth profiling of the d_{33} nonlinear coefficient in annealed proton exchanged $LiNbO_3$ waveguides," Appl. Phys. Lett. **62**, 2012-2014 (1993).
89. J. Amin, V. Pruneri, J. Webjörn, P. S. J. Russell, D. C. Hanna, and J. S. Wilkinson, "Blue light generation in a periodically poled Ti:$LiNbO_3$ channel waveguide," Opt. Commun. **135**, 41-44 (1997).
90. R. Nevado, E. Cantelar, G. Lifante, and F. Cussó, "Preservation of Periodically Poled Structures in Zn-Diffused $LiNbO_3$ Waveguides," Jpn. J. Appl. Phys. **39**, 488-489 (2000).
91. J. Sun, Y. Gan, and C. Xu, "Efficient green-light generation by proton-exchanged periodically poled MgO:$LiNbO_3$ ridge waveguide," Opt. Lett. **36**, 549-551 (2011).
92. H. Hellwig, J. Liebertz, and L. Bohatý, "Exceptional large nonlinear optical coefficients in the monoclinic bismuth borate BiB_3O_6 (BIBO)," Solid State Commun. **109**, 249-251 (1998).
93. H. Hellwig, J. Liebertz, and L. Bohatý, "Linear optical properties of the monoclinic bismuth borate BiBO," J. Appl. Phys. **88**, 240-244 (2000).
94. Z. Zhang, J. Sun, T. Gardiner, and D. T. Reid, "Broadband conversion in an Yb:KYW-pumped ultrafast optical parametric oscillator with a long nonlinear crystal," Opt. Express **19**, 17127-17132 (2011).
95. N. Umemura, K. Miyata, and K. Kato, "New data on the optical properties of BiB_3O_6," Opt. Mater. **30**, 532-534 (2007).
96. Y. Okamura, S. Yoshinaka, and S. Yamamoto, "Measuring mode propagation losses of integrated optical waveguides: a simple method," Appl. Opt. **22**, 3892-3894 (1983).
97. S. J. Beecher, R. R. Thomson, D. T. Reid, N. D. Psaila, M. Ebrahim-Zadeh, and A. K. Kar, "Strain field manipulation in ultrafast laser inscribed BiB_3O_6 optical waveguides for nonlinear applications," Opt. Lett. **36**, 4548-4550 (2011).
98. E. Desurvire, "Ch. 4. Characteristics of erbium-doped fiber amplifiers," in *Erbium-doped fiber amplifiers* (Wiley-Interscience, 2002).
99. E. Delevaque, T. Georges, M. Monerie, P. Lamouler, and J. F. Bayon, "Modeling of pair-induced quenching in erbium-doped silicate fibers," IEEE Photonics Technol. Lett. **5**, 73-75 (1993).
100. Y. Kondo, M. Ono, J. Kageyama, H. Hayashi, M. Reyes, and N. Sugimoto, "Gain characteristics of 6cm-long Er-doped bismuthate waveguide," Electron. Lett. **41**, 317-318 (2005).

101. W. W. Rigrod, "Saturation Effects in High-Gain Lasers," J. Appl. Phys. **36**, 2487-2490 (1965).
102. A. Eckbreth, "Coupling considerations for ring resonators," IEEE J. Quantum Electron. **11**, 796-798 (1975).
103. E. Ramsay, R. R. Thomson, N. D. Psaila, A. K. Kar, and D. T. Reid, "Laser action from an ultrafast laser inscribed Nd-doped Silicate glass waveguide," IEEE Photonics Technol. Lett. **22**, 742-744 (2010).
104. G. D. Marshall, P. Dekker, M. Ams, J. A. Piper, and M. J. Withford, "Directly written monolithic waveguide laser incorporating a distributed feedback waveguide-Bragg grating," Opt. Lett. **33**, 956-958 (2008).
105. L. Hargrove, R. Fork, and M. Pollack, "Locking of He-Ne laser modes induced by synchronous intracavity modulation," Appl. Phys. Lett. **5**, 4 (1964).
106. F. X. Kärtner and U. Keller, "Stabilization of solitonlike pulses with a slow saturable absorber," Opt. Lett. **20**, 16-18 (1995).
107. G. P. Agrawal, "Ch. 2. Pulse propagation in fibers," in *Nonlinear fiber optics,* 3rd ed. (Academic Press, 2001).
108. S. Kelly, "Characteristic sideband instability of periodically amplified average soliton," Electron. Lett. **28**, 806-807 (1992).
109. M. L. Dennis and I. N. Duling III, "Experimental study of sideband generation in femtosecond fiber lasers," IEEE J. Quantum Electron. **30**, 1469-1477 (1994).
110. S. J. Beecher, R. R. Thomson, N. D. Psaila, Z. Sun, T. Hasan, A. G. Rozhin, A. C. Ferrari, and A. K. Kar, "320 fs pulse generation from an ultrafast laser inscribed waveguide laser mode-locked by a nanotube saturable absorber," Appl. Phys. Lett. **97**, 111114 (2010).
111. W.-J. Chen, S. M. Eaton, H. Zhang, and P. R. Herman, "Broadband directional couplers fabricated in bulk glass with high repetition rate femtosecond laser pulses," Opt. Express **16**, 11470-11480 (2008).
112. T. Hasan, Z. Sun, F. Wang, F. Bonaccorso, P. H. Tan, A. G. Rozhin, and A. C. Ferrari, "Nanotube–polymer composites for ultrafast photonics," Adv. Mater. **21**, 3874-3899 (2009).
113. R. Kumar, A. P. Singh, A. Kapoor, and K. N. Tripathi, "Fabrication and characterization of polyvinyl-alcohol-based thin-film optical waveguides," Opt. Eng. **43**, 2134-2142 (2004).
114. J. Limpert, T. Schreiber, T. Clausnitzer, K. Zöllner, H. Fuchs, E. Kley, H. Zellmer, and A. Tünnermann, "High-power femtosecond Yb-doped fiber amplifier," Opt. Express **10**, 628-638 (2002).
115. J. R. Grenier, L. A. Fernandes, P. V. Marques, J. S. Aitchison, and P. R. Herman, "Optical Circuits in Fiber Cladding: Femtosecond laser-written Bragg Grating Waveguides," in *CLEO*, OSA Technical Digest (CD) (Optical Society of America, 2011), CMZ1.
116. P. J. Thomas, C. J. Chunnilall, D. J. M. Stothard, D. A. Walsh, and M. H. Dunn, "Production of degenerate polarization entangled photon pairs in the telecom-band from a pump enhanced parametric downconversion process," Opt. Express **18**, 26600-26612 (2010).
117. D. Ma, Y. Cai, C. Zhou, W. Zong, L. Chen, and Z. Zhang, "37.4 fs pulse generation in an Er:fiber laser at a 225 MHz repetition rate," Opt. Lett. **35**, 2858-2860 (2010).
118. "Optoscribe" (2011), retrieved 21/03/2012, 2012, www.optoscribe.com.
119. "Translume inc." (2011), retrieved 21/03/2012, 2012, www.translume.com.
120. A. E. Siegman, "Ch. 12. Fundamentals of laser oscillation," in *Lasers* (University Science Books, 1986).